NSK

Contents

Technical Articles

New Products

Unique Fatigue Failure of Spherical Roller Bearings and Life-Enhancing Measures
Part II: Long-Life Theory of HPS™ Spherical Roller Bearings

Tohru Ueda, Koji Ueda and Koji Takahashi
Corporate Research & Development Center

ABSTRACT

Tangential force, which is generated by rolling friction between rolling elements and the raceways in a spherical roller bearing, increases due to high contact pressure, excessive sliding, and surface roughness of the rolling elements. This phenomenon helps to explain why surface-originated fatigue failure can sometimes occur even if the bearing is operating under ideal lubricating conditions. It can also explain why spherical roller bearing life is relatively short compared to other bearings. Therefore, it is important to reduce the amount of tangential forces acting between the raceway and a rolling element in order to achieve longer life in a spherical roller bearing. In this study, we developed a long-life theory for NSK's HPS spherical roller bearings, and were successful in both reducing the amount of tangential force and extending bearing life.

1. Introduction

Unlike other types of bearings, spherical roller bearings tend to suffer from surface-originated flaking and exhibit shorter actual operating life compared with calculated operating life. The inner rings of this type of bearing also tend to flake more readily than the outer rings and the rolling elements. We conducted tests that replicated this damage using a twin-disk test machine and studied the relationship between contact pressure, slip distribution, and the point at which flaking occurs to determine the cause of the surface-originated flaking peculiar to spherical roller bearings, which was established in Part I of this study.[1] As a result, we uncovered the fact that spherical roller bearings structurally experience higher contact pressure and more circumferential slip than other roller bearings, and that they develop a specific surface-originated flaking on the inner ring due to a stronger tangential force between the inner ring and the rolling elements, which is caused by greater surface roughness of the rolling elements in comparison with the rolling elements of ball bearings. Therefore, we determined that the tangential force acting on the surface of the inner ring must be restricted in order to achieve longer life for spherical roller bearings.

Consequently, we developed the HPS spherical roller bearing, which achieves longer life by restricting the damage-causing tangential forces acting on the inner ring surface. This report describes a long-life theory and the verification results of this theory for the HPS spherical roller bearing, and the long-life benefits of the HPS spherical roller bearing.

2. Slip Generated on Spherical Roller Bearings

As mentioned earlier, tangential forces acting between the inner ring and the rolling elements must be restricted in order to prevent flaking that occurs with spherical roller bearings. We limited the amount of slip between the raceway and the rolling elements to restrict tangential forces acting on the HPS spherical roller bearings. As many reserchers[2]–[5] have reported in regards to the relationship between slip and tangential forces, the smaller the slip, the lower the tangential force.

In Part I[1] of this report, we only focused on the axial distribution of slip speed. However, both loaded and unloaded zones are formed when a primarily radial load is exerted, and rollers in the unloaded zone rotate more slowly than those in the loaded zone. Therefore, both circumferential and axial distributions of slip speed must be considered when studying actual bearing slip due to slip speed changes in the peripheral direction and changes in roller rotation velocity.

Fig. 1 shows the change of circumferential speed in a bearing's circumferential direction and the distribution of axial slip speed at the maximum load position. The broken line in Fig. 1 (a) shows the circumferential speed of rollers (V_C) at point X in Fig. 1 (b). The solid line in Fig. 1 (a) shows the circumferential speed of rollers at point Y. The line parallel to the X-axis in Fig. 1 (a) shows the circumferential speed of the inner ring (V_B). As shown by the broken line in Fig. 1 (a), the circumferential speed of rollers at point X reaches the same circumferential speed of the inner ring at the maximum load position—or in other words, pure rolling. In this case, slip, which causes

(a) Circumferential speed of rollers (points X and Y)
and circumferential speed of the inner ring

(b) Axial directional distribution of slip
velocity at maximum load position
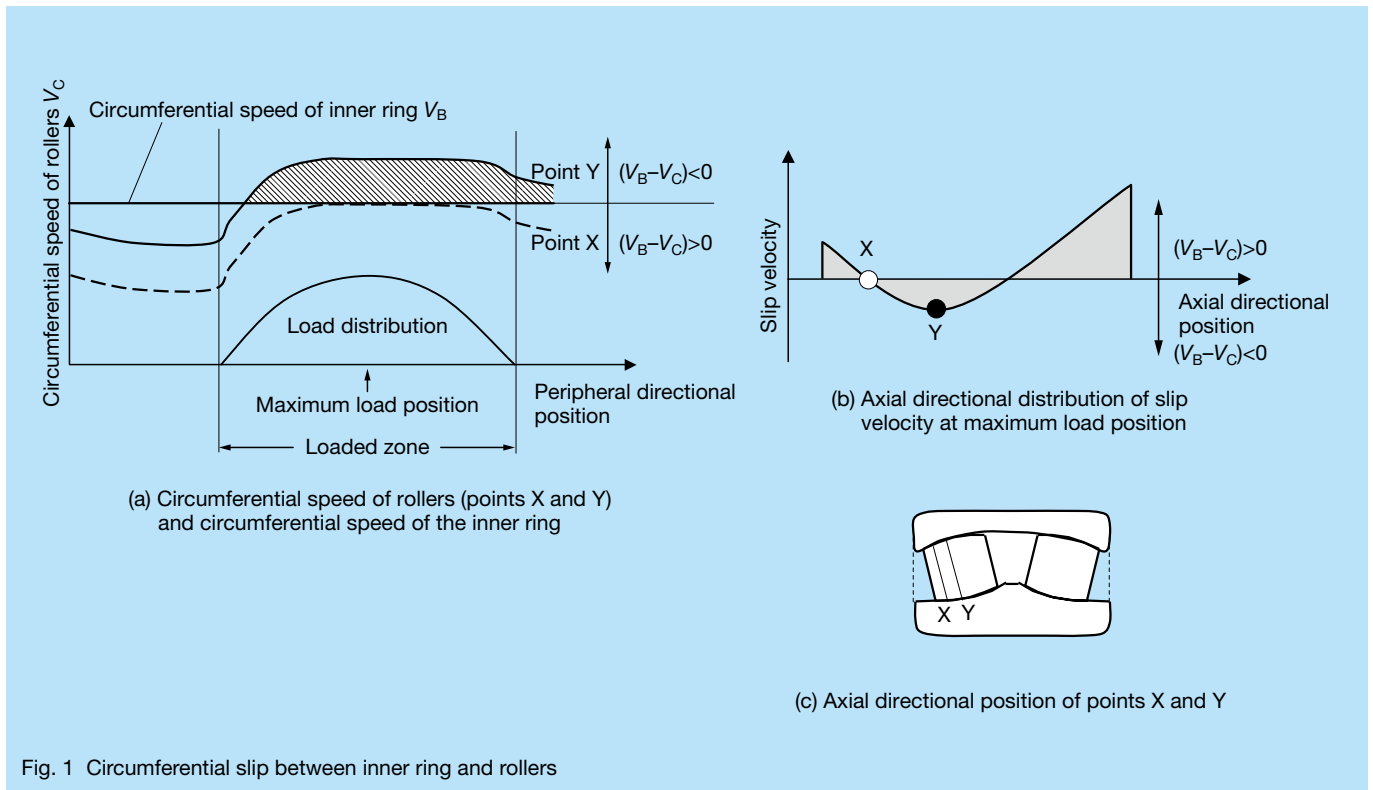
(c) Axial directional position of points X and Y

Fig. 1 Circumferential slip between inner ring and rollers

fatigue failure as a result of tangential forces acting on the inner ring, specifically, slippage against the inner ring in the driven zone ($(V_B-V_C)<0$), is induced because the circumferential speed of rollers at point Y, as shown by the solid line in Fig. 1 (a), is faster than that of the inner ring. The area marked with the diagonal line in Fig. 1 (a) is the area in which slip is being generated against the inner ring in the driven zone; therefore, it is believed that longer life can be achieved by reducing the size of this area, thereby decreasing slip against the inner ring in the driven zone.

3. Long-Life Theory of HPS™ Spherical Roller Bearings

Slowing the circumferential speed of rollers in the loaded zone is necessary to reduce the size of the hatched area in Fig. 1 (a). The friction coefficient between an outer ring and the roller adjacent to the maximum roller diameter position was increased by changing the conditions of the outer ring surface in the HPS spherical roller bearing in order to reduce circumferential speed of the rollers in the loaded zone.

Fig. 2 shows the direction of forces acting on the rollers from the outer ring at the maximum roller diameter position. In the loaded zone, force is applied from the outer ring to reduce rotational motion on the roller since the roller's rotational speed becomes faster than the roller's revolution speed at the maximum roller diameter position. Therefore, when the friction coefficient between the outer ring and the roller increases, the circumferential speed of

the roller decreases because the force to reduce rotational motion increases and slows rotational speed. It is believed that this could reduce slip against the inner ring in the driven zone.

Rotational speed of the roller was measured using a Hall element to confirm this phenomenon. Fig. 3 shows the principle behind this measurement. We mounted one magnetized roller into the bearing and applied a 1.8 V current to the Hall element using a constant-voltage power supply. We monitored the output voltage, which varied with the rotation of the magnetized roller, and converted the value of output voltage variations to rotational angle of the roller in order to calculate its rotational speed. We also measured the circumferential speed of the inner

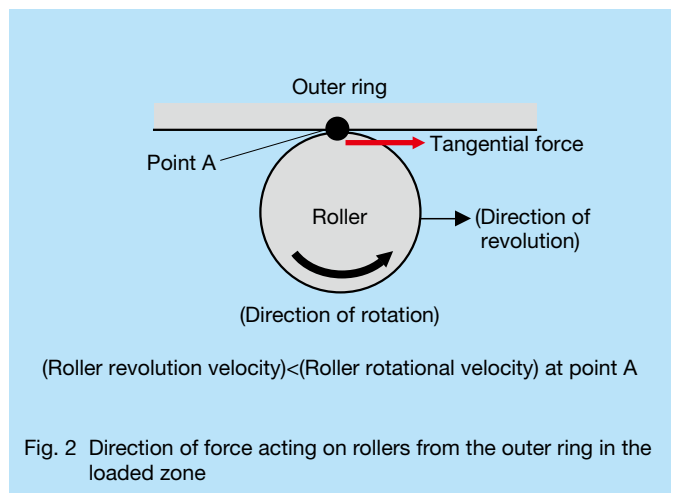(Roller revolution velocity)<(Roller rotational velocity) at point A

Fig. 2 Direction of force acting on rollers from the outer ring in the loaded zone

ring and orbital rotational speed of the roller (rotational speed of the cage) as well as the rotational speed of the roller using reflective tape and a photoelectric probe. The circumferential speed of the roller was calculated by adding measured rotational speed and revolution speed.

Fig. 4 shows the measured results of circumferential speed of the rollers along with that of the inner ring. We used a 22211 bearing for measurement, and an ISO VG68 multi-purpose oil for lubrication. The circumferential speed was measured at the maximum roller diameter position. As shown in Fig. 4, the roller of an HPS spherical roller bearing exhibits faster circumferential speed in the unloaded zone and slower velocity in the loaded zone in comparison with conventional bearings. Additionally, rotation was at a velocity close to pure rotation. In other words, slip against the inner ring in the driven zone of the HPS spherical roller bearings was controlled in the loaded zone where flaking occurs.
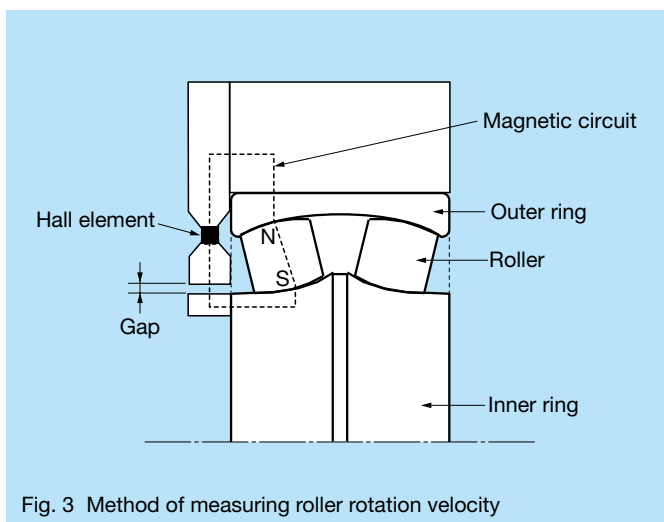
We also conducted verification analysis to further confirm reduced slip in the HPS spherical roller bearings. We used an outer ring that was fixed in position; an inner ring that was afforded two degrees of freedom of motion for the purpose of radial translation; a cage that was afforded three degrees of freedom rotating and radial motion; and rollers with six degrees of freedom of motion.

Fig. 5 shows forces that were applied to the rollers for analysis. Assuming that EHL lubrication was present between the rollers and the raceway surface, we applied slip friction and rolling friction. In addition, the analysis accounts for the slip friction between the rollers and the cage. Regarding Fig. 2, we confined the discussion to the tangential directional force induced between the roller and outer ring raceway surface adjacent to the maximum roller diameter position to facilitate understanding and qualitatively discussed the motion of the rollers. In this analysis, we calculated the circumferential speed of the roller incorporating the force generated between the rollers and inner ring raceway surface and the force generated between the rollers and the cage, as well as the force acting between the rollers and the outer ring raceway. The conditions of analysis were the same as those for measuring the circumferential speed of a roller using a Hall element, with a 22211 bearing and ISO VG68-equivalent lubrication oil. Fig. 6 shows the results of analyzing the circumferential speed of the roller. As shown in the figure, an HPS spherical roller bearing with larger friction coefficient between the roller and the outer ring exhibits higher circumferential speed of the roller in the unloaded zone and lower velocity in the loaded zone compared with conventional bearings. The HPS bearing also rotates at a velocity close to pure rolling. In fact, the results in the figure show the same tendency as the measured results using a Hall element, as shown in Fig. 4. The analysis results also confirmed that in the loaded

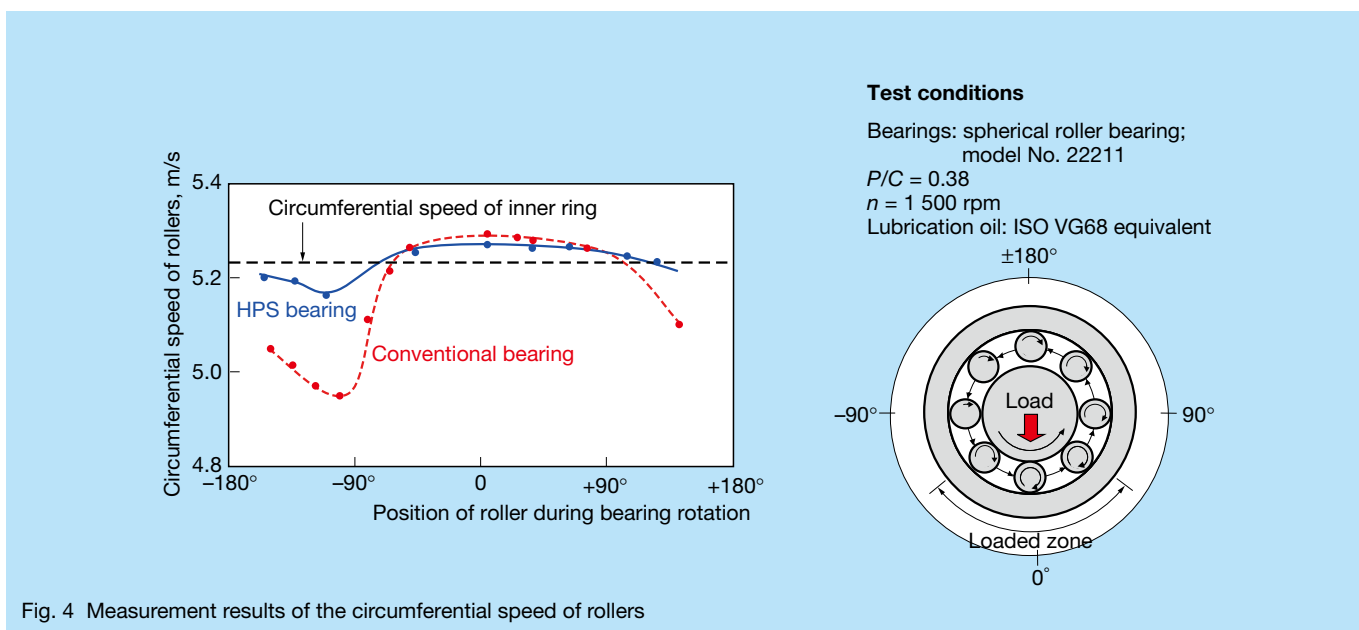Fig. 3 Method of measuring roller rotation velocity

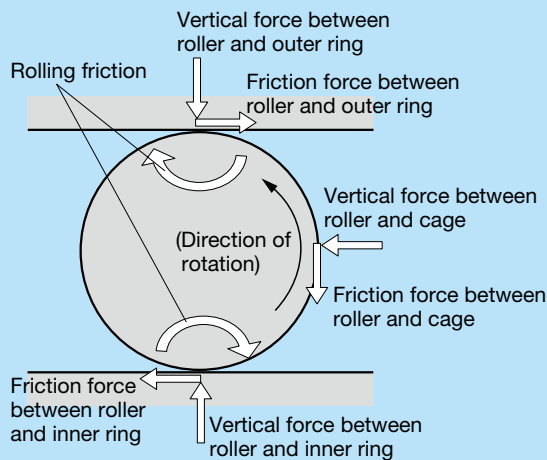Fig. 4 Measurement results of the circumferential speed of rollers

Fig. 5 Analysis incorporates the forces acting on the roller

zone, slip with the inner ring in the driven zone was reduced in the HPS spherical roller bearing. The results shown in Fig. 4 and Fig. 6 illustrate that a HPS spherical roller bearing reduces slip, which causes damage, or in other words, it reduces slip with the inner ring in the driven zone, and longer bearing life can therefore be expected.

Fig. 7 shows the results of measuring the surface fatigue index of the inner ring, outer ring, and rollers by the method[6]–[8] described in Part I[1] by driving the conventional bearing and HPS spherical roller bearing up to their calculated operating life. In addition, Fig. 7 shows model drawings of the distribution of axial slip speed at the maximum load position of a conventional bearing alongside the HPS spherical roller bearing. As shown in Fig. 7, the surface fatigue index of the inner ring decreased in the HPS spherical roller bearing in comparison with the conventional bearing because slip with the inner ring in the driven zone was reduced. Conversely, the rollers of the HPS spherical roller bearing exhibited a larger surface fatigue index since they generated greater slip in the driven zone than conventional bearings. However, there is less stress on the area subject to slip where the rollers are in the driven zone than the area adjacent to the position that experiences maximum contact pressure where the raceway rings are located in the driven zone, which is due to the fact that this area is close to the roller end with lower contact pressure, as described in Part I[1]. Therefore, fatigue does not develop easily, even when slip with the roller in the driven zone increases. In fact, as shown in Fig. 7, the lifetime of an HPS spherical roller bearing can be expected to be longer when considered over the total lifetime of the bearing because the surface fatigue level of the rollers in the HPS spherical roller bearing is lower than that of the inner ring used in a conventional bearing.
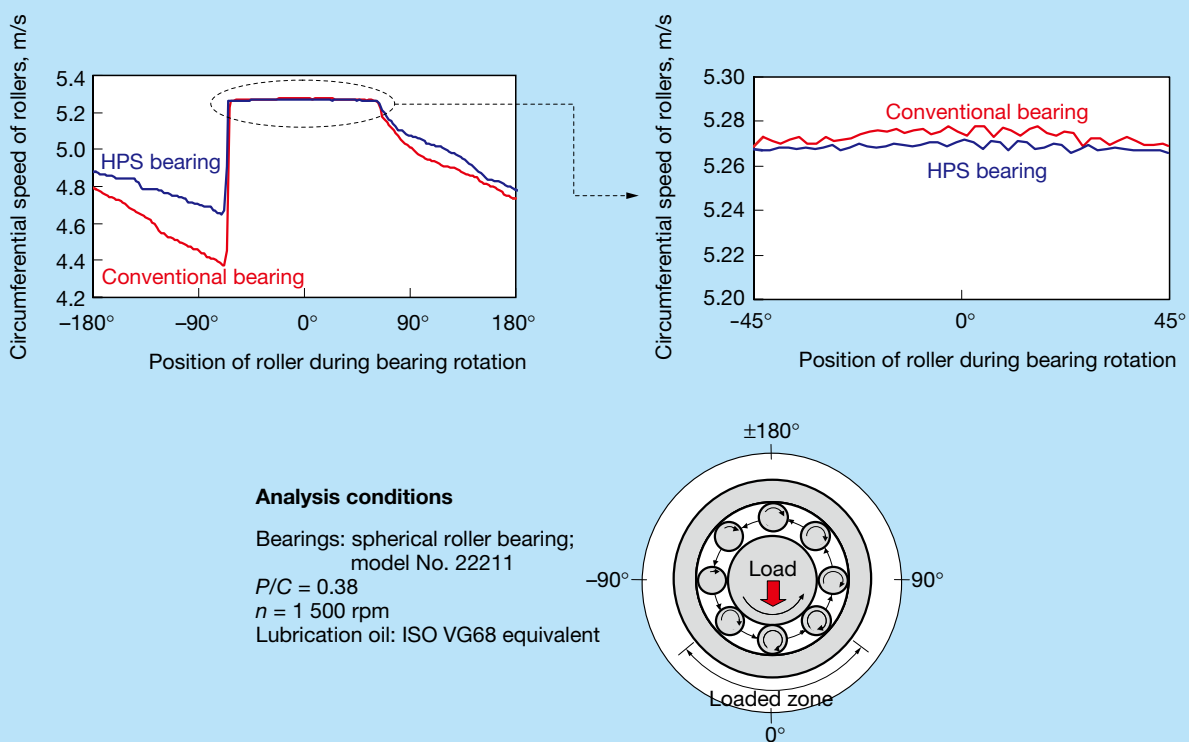

Analysis conditions

Bearings: spherical roller bearing; model No. 22211
P/C = 0.38
n = 1 500 rpm
Lubrication oil: ISO VG68 equivalent

Fig. 6 Analysis results of the circumferential speed of rollers

Axial slip-speed distribution at the maximum-load position

Rollers (driven zone) ↑
Inner ring (driven zone) ↓
Conventional bearing

HPS bearing
Rollers (driven zone) ↑
Inner ring (driven zone) ↓

Surface fatigue index

3.0
2.0
1.0
0

Inner ring
Outer ring
Roller
Conventional bearing

Inner ring Outer ring
Roller
HPS bearing

Test conditions

Bearings: spherical roller bearing;
 model No. 22211
P/C = 0.38
n = 1 500 rpm
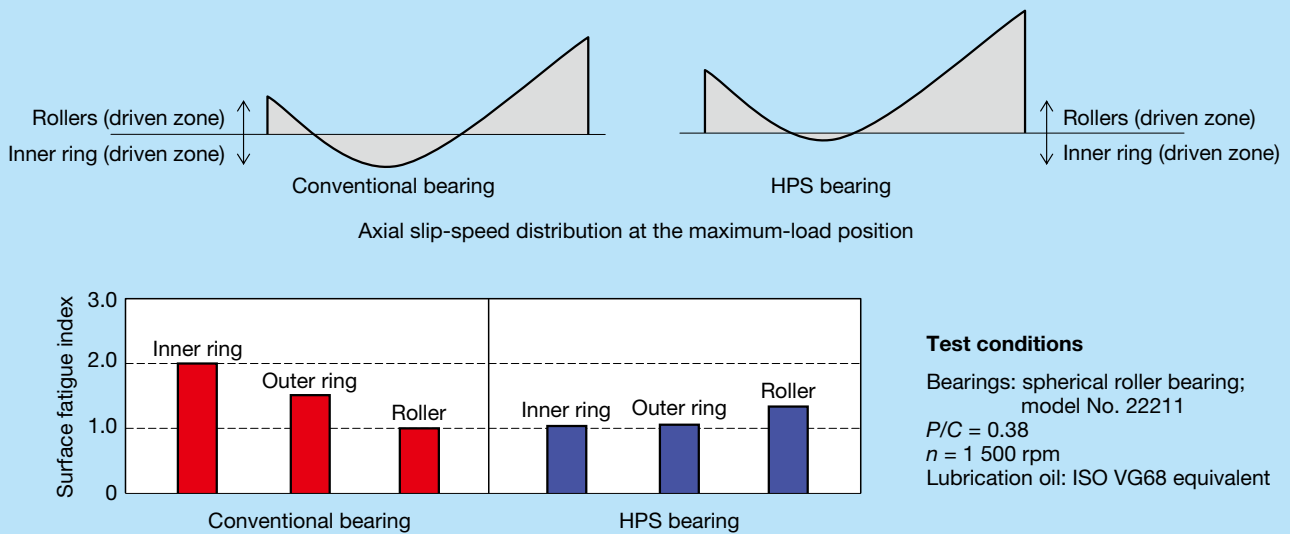Lubrication oil: ISO VG68 equivalent

Fig. 7 Surface fatigue index of the tested bearings

4. Long-Life Effect of HPS™ Spherical Roller Bearings

We tested the lifetime of HPS spherical roller bearings to confirm their effectiveness in extending bearing life compared with conventional bearings.

Fig. 8 shows a schematic view of the test equipment. This equipment is structured so that a radial load is applied on the support bearing at the center, and a load is evenly applied to the test bearings on each side. In addition, pressing the housing with incorporated test bearings in the axial direction exerts an axial load. Fig. 9 summarizes test conditions and results. We used 5 to 16 bearings for each condition in this life test. We organized the data we obtained using the Weibull distribution and calculated the L_{10} life from an optimal distribution line with the least square method. Fig. 9 shows the life ratio with the life of conventional bearings given a value of 1. As shown in the figure, the test results indicate the life of HPS spherical roller bearings is longer than that of the conventional bearings under all conditions of light loads, heavy loads, low speeds, high speeds, multiple loads, and excessive axial loads.

We increased the friction coefficient between the outer ring and rolling elements of the HPS spherical roller bearings to reduce slip with the inner ring in the driven zone. The effect of reducing slip was experimentally proven by the measurement of rotational speed with a Hall element as shown in Fig. 4 and confirmed by calculations of the circumferential speed of the rollers using the analysis in Fig. 6. At the same time, the force generated by acceleration and deceleration is considered to decrease because the variation of bearing circumferential speed of

Fr: Radial load

Tested bearings

Fa: Axial load

Support bearing
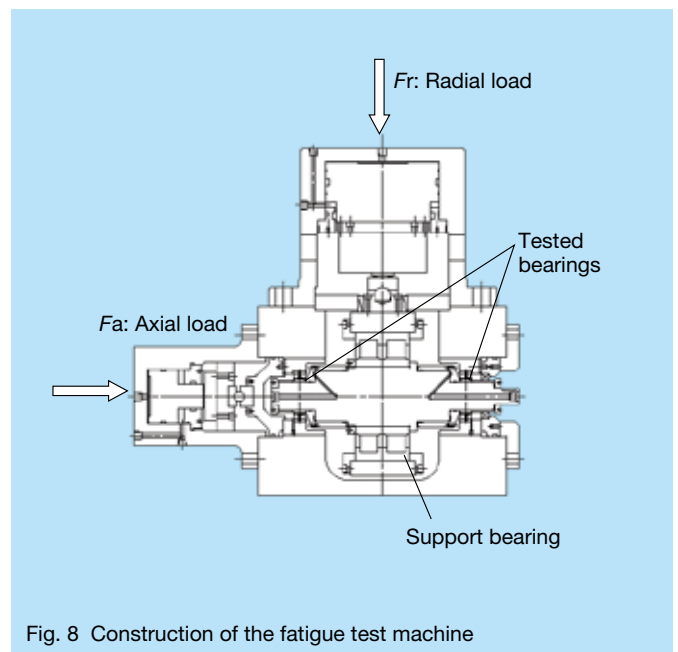
Fig. 8 Construction of the fatigue test machine

the rollers in the HPS spherical roller bearings decreased, as shown in Fig. 4 and Fig. 6. Therefore, it is possible that the extended life shown in Fig. 9 was achieved because the roller acceleration and deceleration decreased to reduce the tangential forces induced by acceleration and deceleration. However, this test and analysis is not sufficient to establish a relationship between roller acceleration and deceleration and bearing life. Clarifying the effect of acceleration and deceleration of rolling elements on operating life is a subject for future analysis.
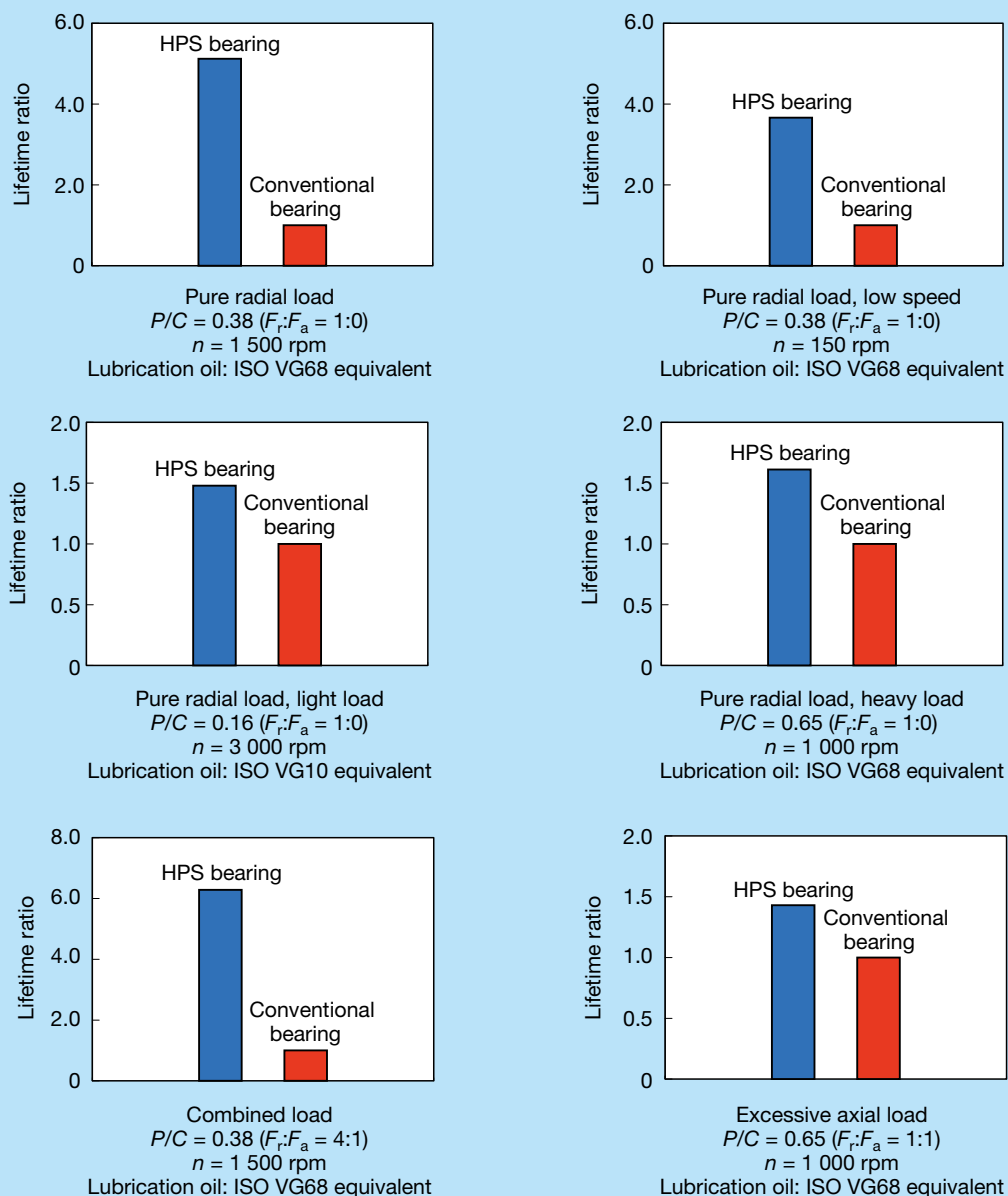
Fig. 9 Fatigue test results

5. Conclusion

The life of HPS spherical roller bearings was extended through the following mechanisms:

a. Increasing the friction coefficient between the outer ring and the rolling elements by changing the surface condition of the outer ring.

b. As the force that reduces rotational motion of the rollers increases, circumferential speed of the roller in the loaded zone decreases.

c. Slip that occurs with the inner ring in the driven zone, which causes damage, is reduced and operating life is extended.

References

1) T. Ueda, K. Ueda, "Fatigue Failure Mechanism of Spherical Roller Bearings and Life-Enhancing Measures Part I: Failure Mechanism of Spherical Roller Bearings" NSK Technical Journal, 680 (2006), 6-1 2.

2) Y. Yamamoto, S. Kaneda, "Tribology" (2001) Rikogakusya Publishing Co., Ltd.

3) N. Soda, T. Yamashita, K. Ohzora, "Influence of Tangential Force Exerted on Rolling Fatigue" Lubrication, 16-8 (1971), 573–584.

4) N. Soda, R. Yamamoto, "Roles of Tangential Force in Development of Pitching in Gears" Lubrication, 20-4 (1975), 268–275.

5) J. Akaoka, T. Nitanai, "Influence of Tangential Force on Rolling Fatigue (Part 1) Effect on Plastic Flow and Work Hardening" Lubrication, 27–3 (1982), 187–192.
6) K. Furumura, S. Shirota, A. Fujii, "Fatigue Analysis of Rolling Bearings (Part 1)—Analysis of Surface Fatigue Damage (1)" NSK Bearing Journal, 643 (1982) 1–10.
7) K. Furumura, S. Shirota, A. Fujii, "Fatigue Analysis of Rolling Bearings (Part 2)—Analysis of Surface Fatigue Damage (2)" NSK Bearing Journal, 644 (1984) 1–5.
8) K. Furumura, S. Shirota, A. Fujii, "Fatigue Analysis of Rolling Bearings (Part 3)—Analysis of Surface Fatigue Damage" NSK Bearing Journal, 646 (1986) 18–25.

Tohru Ueda

Koji Ueda

Koji Takahashi

Power Loss Factor Analysis of the High-Power Output EPS System

Yuushi Momo and Yasuyuki Matsuda
Corporate Research & Development Center

ABSTRACT

In recent years, electric power steering (EPS) systems have effectively contributed to reducing energy consumption of motor vehicles. Starting with minivehicles and subcompacts, the scope of EPS applications expanded further to include small cars, midsize cars, and more recently, large passenger vehicles. Newer EPS systems must be more compact while increasing motor output. Typically, these two requirements contradict each other and would normally require some trade-off in output or size. In order to overcome this conflict, the steering system must be designed to reduce loss of motor power transmission. In this article, we have clarified the loss factor of certain components by breaking down the efficiency of an EPS system into the efficiency of each component. We also propose a more highly effective EPS system based on the results of loss analysis.

1. Introduction

In recent years, the shift from hydraulic power steering systems to electric power steering (EPS) systems has been advancing due to several factors including the need to reduce fuel consumption, the transition to electrical control, and the trend towards reducing environmental impact. Until recently, EPS systems have been widely used for minivehicles or compact vehicles due to the power output levels of EPS. However, the scope of EPS systems is gradually expanding to include midsize to large passenger cars. Consequently, efforts have been made to design EPS systems with higher power output, but these efforts have encountered the challenge of increasing output without overly increasing the size of the EPS unit. To achieve both high output and a compact size, it is necessary to improve the efficiency of power transmission from the EPS motor without sacrificing power levels.

NSK analyzed and clarified the loss factor of each system component with the goal of improving system efficiency for a high-output EPS system. In this process, we achieved an optimally designed EPS system based on analysis results of loss factors and made improvements to ensure high output and high efficiency. This report offers recommendations in these areas with a primary focus on column-type EPS systems.

2. Transition to High-Output EPS System

High-output EPS systems face the following challenges:

· Increasing output of the power-assist motor;
· Improving the strength of component parts so as to endure the higher output;
· Minimizing the overall size of the system; and
· Improving efficiency through the use of component parts that transmit output without loss.

Possible measures for achieving higher output from the power-assist motor with a constant voltage source include increasing torque, rotational speed, or constant voltage.

Increasing torque can be achieved by boosting magnetic flux. However, when using a brushless motor, flux is equivalent to the size of the magnetized area of the rotor, and therefore increasing flux means enlarging the magnet, which in turn necessitates a larger motor. Furthermore, increasing the size of the rotor would lead to higher inertial momentum of the rotor, which would impair steering feeling.

Increasing rotational speed, the second option, can be achieved by reducing magnetic flux. Reducing magnetic flux can be achieved by reducing the number of windings inside the motor, which makes it possible to minimize the size of the brushless motor. However, the ratio of speed reduction must be enhanced to counter the decrease in motor torque, which is a trade-off for higher rotational speed. Improving the speed reduction ratio leads to an increase in the size of applicable parts (such as the worm and worm wheel gear). Moreover, enhancing the speed reduction ratio will lead to an increase in torque variation, which in turn can impair steering feeling.

Increasing constant voltage, the third option, would lead to a bigger motor since it requires a larger diameter motor coil and therefore a larger, effective slot area in a rotor. In addition, increasing the current will boost internal heat generation in the ECU and the motor, thus requiring more efficient heat dissipation (such as a larger heat sink and different materials for better performance). In terms of the ECU, different components that can handle a higher current must be selected, which would increase costs.

Increasing the output of power-assist motor leads to various limitations, as explained above. Trade-offs in terms of motor size, cost, or steering feeling make it very difficult to produce a power-assist motor with higher output in particular.

Furthermore, increasing motor output requires enhancing the strength of components that transmit

motor torque. The speed reduction mechanism transmits torque via the worm drive; therefore, the worm and worm wheel gear would have to be strengthened. Greater strength can be achieved by increasing shaft diameter or tooth thickness, but these steps would call for a larger worm drive. The increased load would also require larger support bearings for both the worm and the worm wheel gear. The same issue applies to rack and pinion mechanisms.

The amount of space for mounting a column-type EPS is limited because it is mounted inside the vehicle's passenger cabin where it is subject to significant interference from other components. Additionally, the space that is required for an energy absorption mechanism must be considered to protect passengers in the event of a frontal collision.

For these reasons, it is essential to achieve both higher output and minimize size in order to develop a high-output EPS system. To this end, constructing a method for designing a highly efficient EPS that can transmit output without loss is necessary.

Fig. 1 shows the layout of a column-type EPS system. This system can be separated into three component groups: the column, the intermediate shaft, and the rack and pinion mechanism. The following formulas provide output values for both column-type and pinion-type EPS systems using the transmission coefficients of each component.

Column-type EPS

$$F = T_h \cdot \frac{2\pi}{C} \cdot \eta_s \cdot \eta_p + T_m \cdot G_r \cdot \frac{2\pi}{C} \cdot \eta_r \cdot \eta_s \cdot \eta_p \quad \text{...................... (1)}$$

Pinion-type EPS

$$F = T_h \cdot \frac{2\pi}{C} \cdot \eta_s \cdot \eta_p + T_m \cdot G_r \cdot \frac{2\pi}{C} \cdot \eta_r \cdot \eta_p \quad \text{......................... (2)}$$

F: Output (N)
T_h: Steering torque of driver (N·m)
T_m: Motor torque (N·m)
C: Ratio of rack stroke (m) and pinion stroke (rev), (m/rev)
G_r: Speed reduction ratio
η_r: Efficiency of speed reduction mechanism
η_s: Efficiency of intermediate shaft part
η_p: Efficiency of rack and pinion mechanism

EPS output is expressed as the sum of the driver's steering force (first item in the formula) and the force of the power-assist motor (second item in the formula). The force of the power-assist motor sufficiently increases to a level that corresponds with the driver's steering force since motor output is increased by the speed reduction ratio.

The second item in the column-type EPS formula shows that higher output can be achieved by improving the efficiency of the speed reduction mechanism, intermediate shaft, and the rack and pinion mechanism. However, since the intermediate shaft is already highly efficient for structural reasons, it is not significant for this calculation. The efficiency of the intermediate shaft η_s is eliminated in the second item in the formula of the pinion-type EPS since power-assist motor is located at the lower end of the shaft. Consequently, we analyzed the loss factors of the component elements in the speed reduction mechanism, and the rack and pinion mechanism.
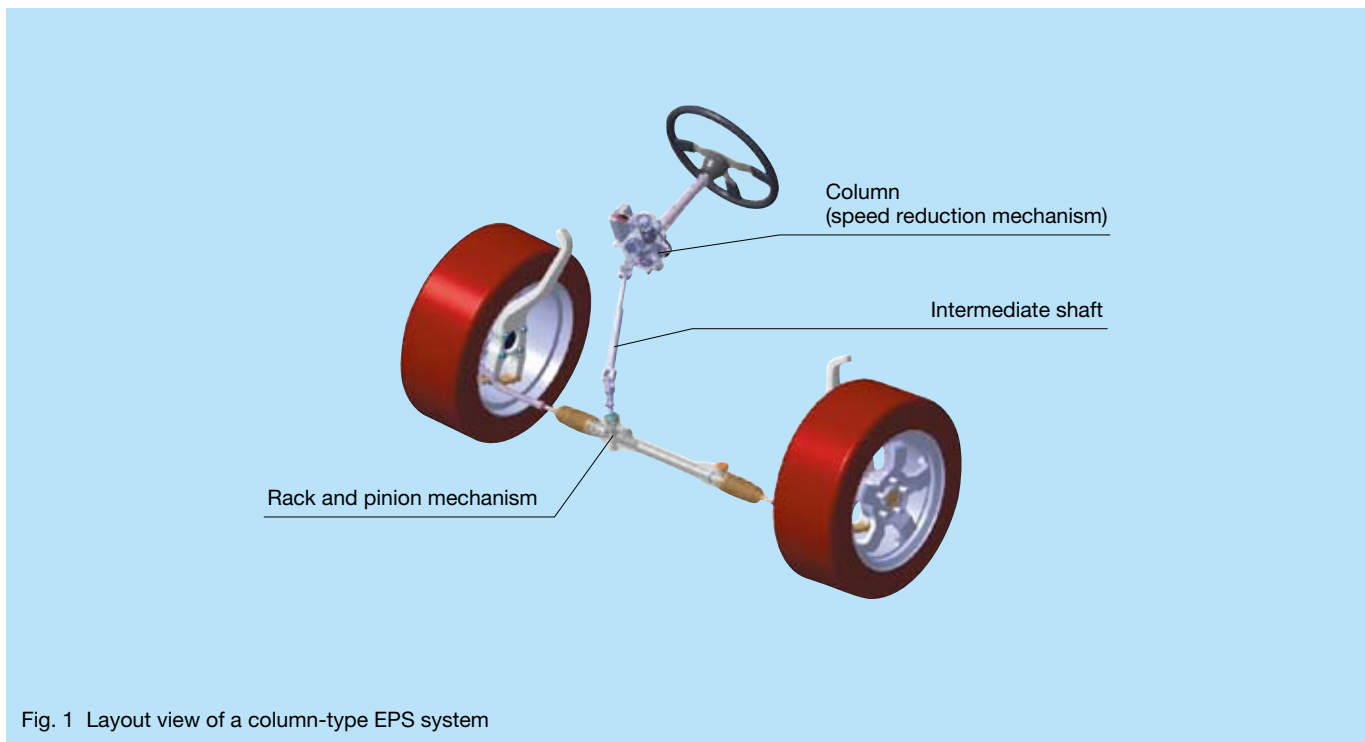

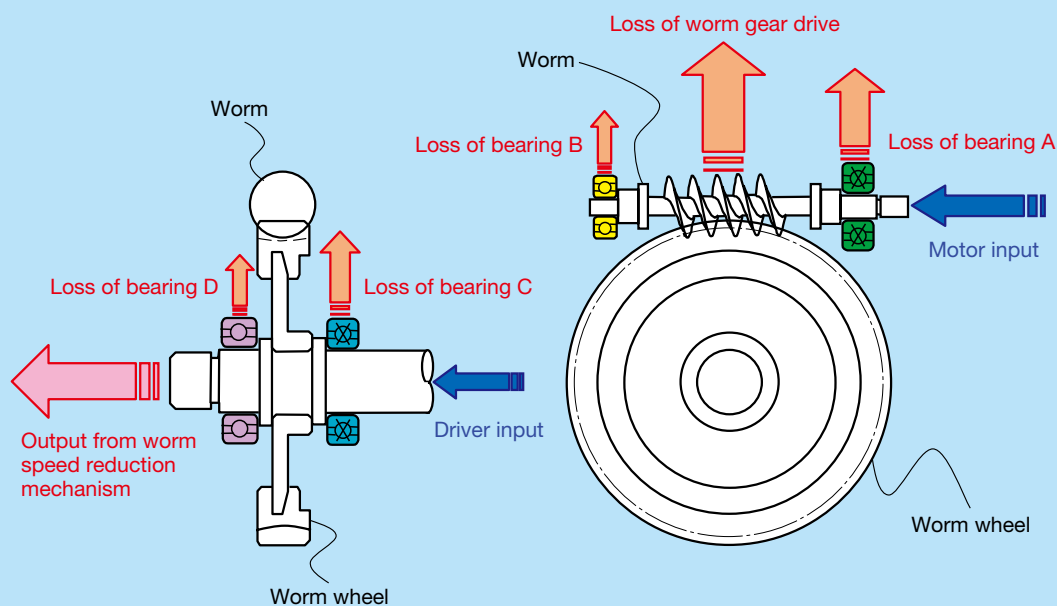Fig. 1 Layout view of a column-type EPS system

Fig. 2 Loss factors of the speed reduction mechanism

3. Power Loss Factor Analysis

3.1 Analysis methods

We analyzed loss factors through simulation and experiments. Loss factors were separated into those related to the bearings and those related to other parts, and were each analyzed in the simulation. Losses in the bearing part were obtained using NSK's bearing analysis software package (BRAIN[1), 2)]), which is used for analyzing the kinematical performance of bearings. Values for relative slip velocity and traction coefficient (friction coefficient) of the gear mesh surfaces are necessary for evaluating frictional loss in the gear mesh area. We calculated relative slip velocity geometrically and calculated traction coefficient using a traction model of a lubricant agent. These calculations were similar to a performance analysis of bearings and precision machine components.

Experimental measurements of frictional loss were divided into two groups according to mechanism: speed reduction mechanism and rack and pinion mechanism. We measured frictional loss values for the entire unit and for each bearing. The frictional loss for each bearing was measured by applying axial and radial loads and then by calculating input torque. Frictional loss in the gear mesh area was obtained by subtracting the frictional loss of each bearing from that of the whole unit.

We compared simulated and measured results obtained using the above processes and evaluated the validity of simulation. We also analyzed the loss factor for each unit and studied the impact on system efficiency. A summary of the results follows.

3.2 Power loss factor analysis of the speed reduction mechanism

The speed reduction mechanism transmits output from the power-assist motor. Fig. 2 illustrates the configuration and loss factor process for the speed reduction mechanism. The speed reduction mechanism consists of a worm and a worm wheel, both of which are supported by two bearings. Loss related to the mesh of the worm and the worm wheel and loss from the four bearings are considered to be the source of loss factors in the speed reduction mechanism.

We conducted simulations and experiments to analyze the loss factors described above (see Fig. 3 for results).
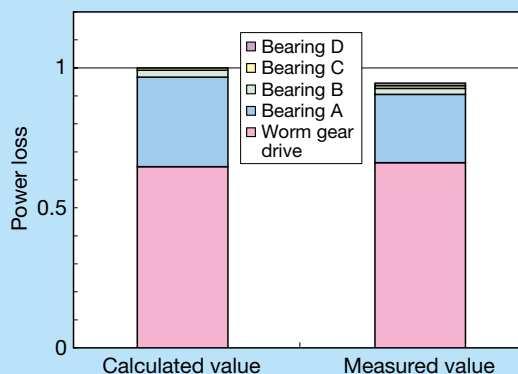

Fig. 3 Analysis results and measurement results of loss factors for the speed reduction mechanism
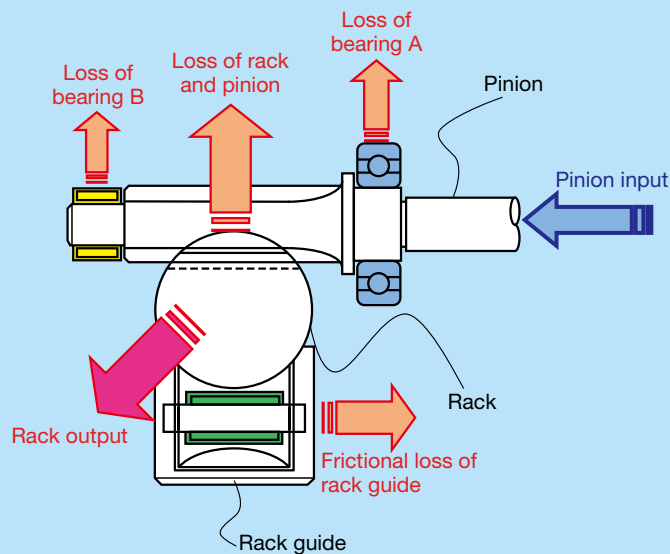
Fig. 4 Loss factors of the rack and pinion mechanism

Here, we non-dimensionalized two values using the calculated value of the entire speed reduction mechanism. Simulation and experimental results were nearly identical, with the difference being well within a range of ± 10 %, which confirms that the simulated evaluation of frictional loss was sufficiently reliable and suitable for future design purposes. The simulated and experimental results indicate that the primary loss factor is due to the mesh—almost 70 % of the total. The secondary factor is the motor side bearing of the worm shaft—representing 25 %. This means the primary and secondary factors account for nearly 95 % of the loss.

The speed reduction mechanism used for this analysis is equipped with a mechanism for applying a preload between the worm and worm wheel with a spring to reduce rattling while driving. Loss on the motor side bearing of the worm shaft is expected to increase due to a swaying motion of the worm shaft with the bearing acting as a fulcrum because of this preload mechanism.[3]

3.3 Power loss factor analysis of rack and pinion mechanism

The rack and pinion mechanism converts the rotational motion of the pinion to a linear motion via the rack. The driver's steering rotates the pinion gear in the steering system and this rotation is converted to linear motion of the rack via the rack gear. Transmitting this rack motion to the wheels through tie rods at both ends of the rack controls the direction of the vehicle. Fig. 4 illustrates the configuration and loss factors of the rack and pinion mechanism. Here, we non-dimensionalized two values using the calculated value of the entire rack and pinion

mechanism. The rack and pinion mechanism consists of two bearings that support the pinion, and a rack guide that supports the rack in addition to the rack and pinion. Power loss of the rack and pinion mechanism is divided into loss of the mesh between the rack and the pinion, loss of the two bearings, and loss from the rack sliding over the rack guide.

We conducted simulations and experiments to analyze the loss factors of the rack and pinion mechanism (see Fig. 5 for results).

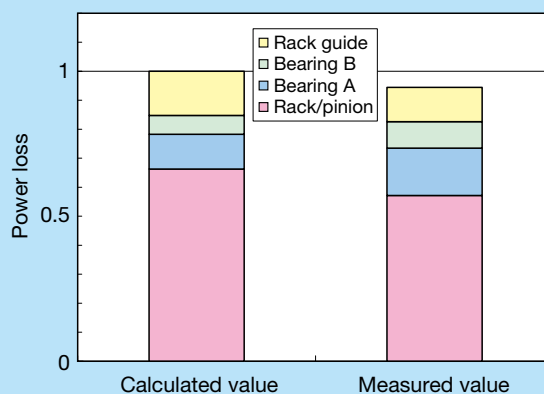Simulated and experimental results were nearly identical, with the difference being well within the

Fig. 5 Analysis results and measurement results of loss factors for the rack and pinion mechanism

range of ± 10 % for frictional loss of the rack and pinion mechanism, which is similar to our analysis of the speed reduction mechanism. Moreover, this simulation has been confirmed as being sufficiently reliable.

Fig. 5 shows that the main factor of loss in the rack and pinion mechanism is from the mesh (same for the speed reduction mechanism), which accounts for nearly 60 % of the total. Subsequent factors are losses of the bearings on the input side and that of the rack guide, which account for 10 to 15 % of the total.

4. Optimum Specification Study

We worked on an optimized design of the components, which significantly influenced efficiency in the loss factor analysis results, and confirmed its effectiveness.

4.1 Speed reduction mechanism

Major losses in the speed reduction mechanism are from the gear mesh area and from the motor side bearings of the worm shaft. We sought ways to mitigate these two factors. The following measures were taken to reduce loss in the gear mesh area:

· Improve worm wheel gear surface;
· Apply grease with a low traction coefficient; and
· Improve the gear tooth contact.

As a result, efficiency in the gear mesh area improved by 2 %. We also implemented an optimized parameter design for the motor side bearings of the worm shaft to decrease torque using the BRAIN software. As a result, efficiency improved by 1 %. Fig. 6 shows the effects of improvements that were achieved in optimizing specifications resulting from incorporating the measures described above. Here, we assumed a value of 1 for the entire speed reduction mechanism of the former specification. Overall improvement for the entire speed reduction mechanism

was approximately 3 %.

4.2 Rack and pinion mechanism

Major losses at the rack and pinion mechanism come from the gear mesh area, and the input side bearings of the pinion and the rack guide. For this report, we studied measures for reducing losses in the gear mesh area and the bearings. We developed an analysis program that helps to improve efficiency in addition to dedendum strength and tooth face strength, which represent common evaluation standards for gears, to obtain the optimized specifications for the gears, which incorporate gear mesh loss. This analysis program enabled us to obtain the most efficient specifications within parameters that satisfied both dedendum and tooth face strength. We tried to improve the loss of the gear mesh area by reviewing the following gear parameters in this program:

· Mesh angle of rack and pinion mechanism; and
· Addendum and dedendum parameters.

In addition, the following improvements were made:

· Improved shape of gear tooth face and surface roughness; and
· Usability of greases with low traction coefficient.

As a result, efficiency at the gear mesh improved 2.5 %. We implemented a low-torque design using the BRAIN software for the parameter of the input side bearings, resulting in a 1 % improvement in efficiency.

Fig. 7 illustrates the improvements we achieved with these optimized specifications. Here, we assumed a value of 1 for the entire rack and pinion mechanism of the conventional specifications. The entire rack and pinion mechanism improved by approximately 3.5 %.
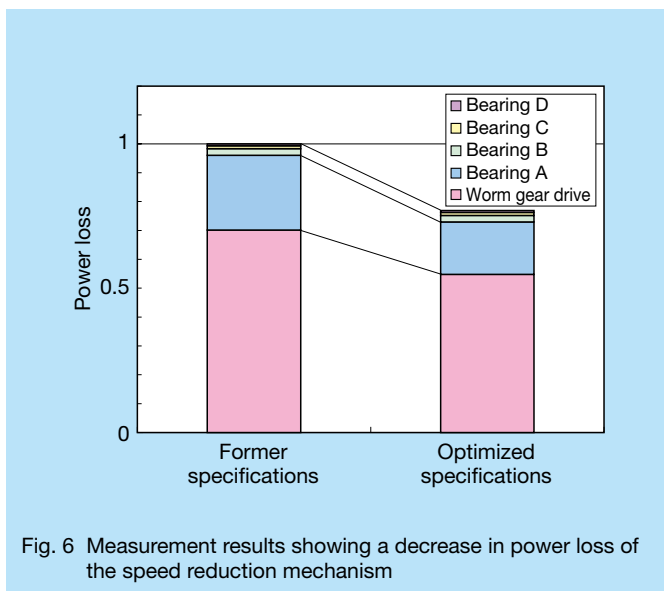

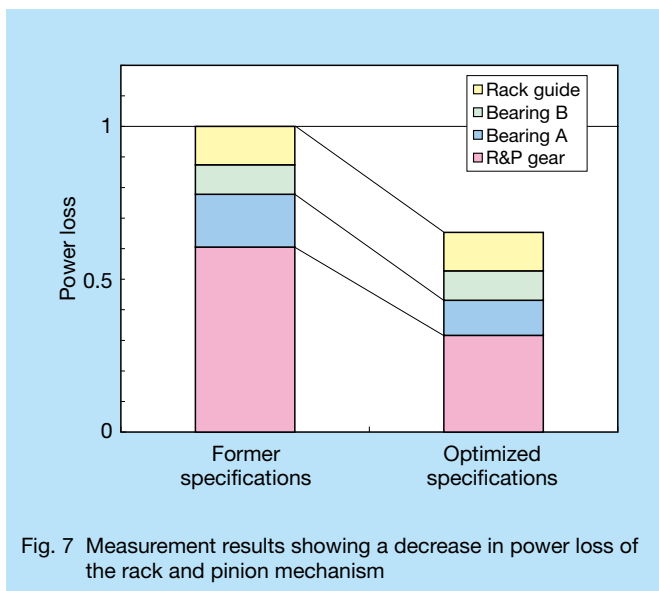Fig. 6 Measurement results showing a decrease in power loss of the speed reduction mechanism

Fig. 7 Measurement results showing a decrease in power loss of the rack and pinion mechanism
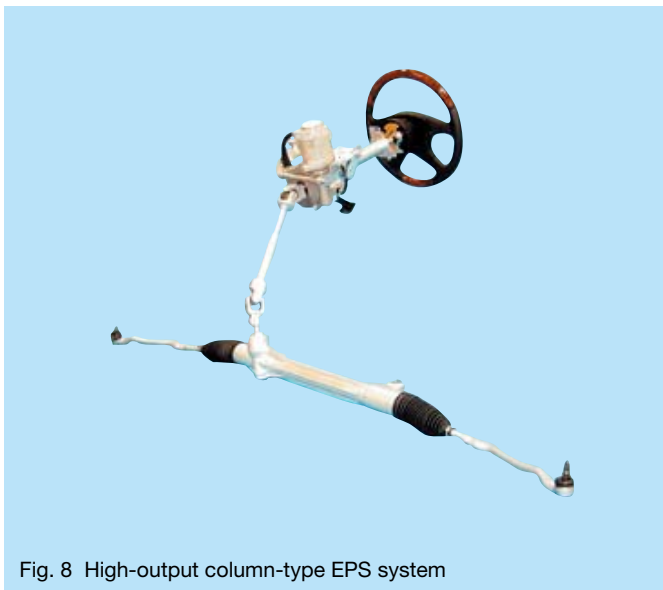
Fig. 8 High-output column-type EPS system

Yuushi Momo

Yasuyuki Matsuda

5. Conclusion

We analyzed the loss factor of the speed reduction mechanism and the rack and pinion mechanism, which are key to improving efficiency, through simulations and experiments in order to achieve higher output in an EPS system. Simulated and experimental results compared well. We optimized the design of the elements, which represented the major sources of loss for each mechanism, and achieved a 3 % improvement in efficiency in the speed reduction mechanism and 3.5 % improvement in the rack and pinion mechanism.

Each of the measures recommended in this report have been applied to the development of the column-type EPS shown in Fig. 8. This EPS system offers 12 000 N of rack thrust force, which is 1.5 times higher than that of conventional models, and can be mounted to a 3-liter class, full-size, passenger vehicle. Looking ahead, we will continue to work to achieve higher simulation accuracy and will seek to combine evaluation technologies in future studies of endurance and fatigue in order to pursue research and development that meets the needs of the times.

References
1) H. Aramaki, "Rolling Bearing Analysis Program Package 'BRAIN'" NSK Technical Journal, 663 (1997) 1–7.
2) S. Natsumeda, "Computer Simulation Technique for Predicting Performance of Rolling Bearings" NSK Technical Journal, 673 (2002) 31–35.
3) New Products, "High-Power Column-Type Electric Power Steering" NSK Technical Journal, 679 (2005) 52–53.

Development of the Next-Generation Half-Toroidal CVT —Power Transmission Efficiency and Control of the Geared-Neutral System

Takashi Imanishi, Takumi Shinojima, Toshiro Toyoda, and Eiji Inoue
Technology Development Center, CVT Project Team

ABSTRACT

The authors are developing a new half-toroidal CVT that offers a wider ratio range, higher torque capacity, and higher efficiency in a more compact size. Major features of this new half-toroidal CVT include a geared-neutral system and a power-split system. We successfully downscaled the current CVT by eliminating conventional launching devices, such as the torque converter and friction clutch, and focused our energies on a geared-neutral system. In this paper, we focus on the power transmission efficiency of such a system and present theoretical calculations and experimental results. Concepts for achieving higher efficiency will be also discussed. In an IVT, the control scheme at near-zero speed is one of the more important issues of this technology that needs to be addressed. Conventional torque controls are discussed in this area. The authors describe new control concepts based on a speed ratio-control scheme with additional torque compensation and present results of testing that was completed using an actual vehicle.

1. Introduction

Transmission systems play an important role in drive trains and are vital for the development of automobile technology that contributes to a sustainable society. Expectations have been rising steadily for an ideal continuously variable transmission (CVT) that achieves both low fuel consumption and outstanding vehicle performance. The half-toroidal CVT, which was first introduced commercially in 1999, now faces demands for a more compact size, higher torque capacity, higher efficiency, and lower cost. The authors have developed and now propose a next-generation toroidal infinitely variable transmission (IVT) adopting a geared-neutral and power-split system, as shown in Fig. 1, as a transmission system that satisfies these requirements.[1]

This report examines the power transmission efficiency of a power recirculation system as well as actual measured efficiency based on a prototype. In addition, near-zero speed control (near the geared-neutral point) is considered to be a key issue for IVTs. In regards to this control method, the authors present a geared-neutral control concept based on a transmission gear ratio control instead of the conventional torque control method.

2. Toroidal IVT Gear Train

2.1 Low mode (low-speed side mode)

For a next-generation toroidal IVT, we adopted a geared-neutral system that utilizes a differential mechanism with a double-pinion planetary gear for low mode, which is used on the low-speed side. Fig. 2 shows power transfer in low mode. The engine simultaneously drives both the input disc and the front-side planetary gear carrier across a

vibration-absorbing damper. Variator output is transferred to the sun gear (S1), part of the planetary gear, via the through shaft. The ring gear, also part of the planetary gear (R1), transmits the output of the IVT mechanism, and this output is transferred to the transmission output shaft through the low mode (low-speed side mode) clutch. The relationship between the operating speeds of each component (sun gear, ring gear, and carrier) has been well established, and the relationship of the input and output speed in the whole IVT mechanism is expressed with the following formulas:

$$N_{\mathrm{OUT}} = N_{\mathrm{R}} = \frac{(i_1 - 1) - e_{\mathrm{V}}}{i_1} N_{\mathrm{IN}} \quad\cdots\cdots\cdots\cdots\cdots\cdots\cdots (1)$$

N_{IN}: Transmission input rotation speed (= engine rotation speed)
N_{OUT}: Transmission output rotation speed

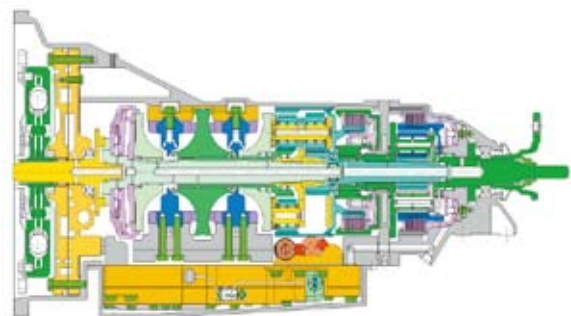
Fig. 1 Next-generation toroidal IVT

N_R: Ring gear rotation speed

i_1:   Planet gear ratio $(= Z_{R1}/Z_{S1})$

Z_{R1}:   Number of teeth, ring gear 1

Z_{S1}:   Number of teeth, sun gear 1

e_V: Variator speed ratio $\left(= \dfrac{\text{Output disc speed}}{\text{Input disc speed}} \right)$

2.2 High mode (high-speed side mode)

The high mode clutch is engaged on the high-speed side to switch the configuration of the planetary gear. This enhances the maximum speed-increasing ratio and reduces engine rotation speed during high-speed driving. In addition, high mode enables power-split transmission while a portion of the engine power is transmitted to the output shaft from the engine through the planetary gear instead of the variator. This configuration enabled a reduction in the size of the variator as well as the overall size of the IVT. Variator load during high-speed driving under continuous high-load operation can be reduced, which is an important feature that was not previously possible in a conventional CVT mechanism.

Fig. 3 shows power transmission in high mode. While the link between the sun gear and the carrier in the planetary gear is the same as that in low mode, the ring gear (R1) on the front-side planetary gear is free and the back-side sun gear (S2) of the Ravigneaux gear set transmits the output instead. The transmission gear ratio of the IVT in high mode is expressed with formula (2). A reverse speed reduction gear is necessary on the rear side to match the output rotational speed in low mode and in high mode at the point of switching from low to high mode. The planetary gear on the rear side in Fig. 3 is the sun gear (S3) input and carrier output, and is used as the reverse speed reduction gear.

$$N_{OUT} = \frac{e_V - (i_{12} - 1)}{i_{12} \cdot (i_3 - 1)} N_{IN} \quad \text{.. (2)}$$

i_{12}:   Gear ratio between sun gear 1 and sun gear 2

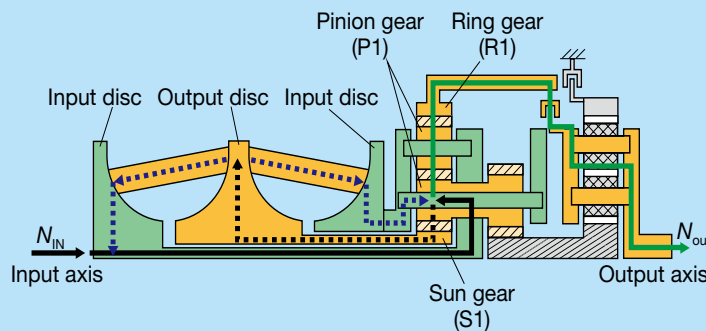$$\left(= \frac{Z_{P1}}{Z_{S1}} \cdot \frac{Z_{S2}}{Z_{P2}} \right)$$
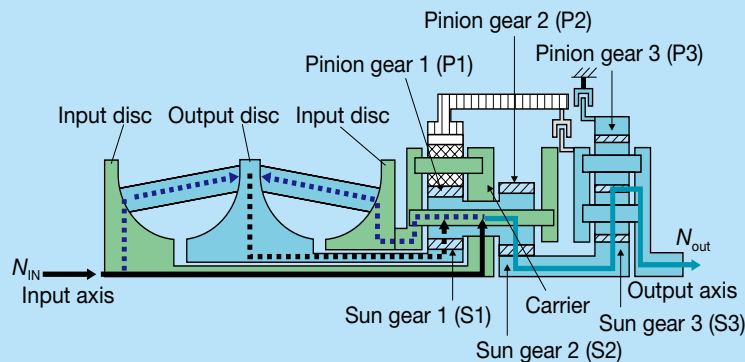

Fig. 2 Power flow for forward low-mode drive conditions

Fig. 3 Power flow for high-mode drive conditions

i_3: Planetary gear ratio ($= Z_{R3}/Z_{S3}$)
Z_{P1}: Number of teeth, pinion gear 1
Z_{P2}: Number of teeth, pinion gear 2
Z_{S2}: Number of teeth, sun gear 2
Z_{R3}: Number of teeth, ring gear 3
Z_{S3}: Number of teeth, sun gear 3

3. Power Transmission Efficiency

3.1 Theoretical transmission efficiency

Several studies have been conducted on the transmission efficiency of a planetary gear that has a differential rotation.[2] The planetary gear part can be regarded as a 2-input/1-output component when this concept is applied to the gear in low mode and efficiency can be expressed with the following formulas:

Efficiency between carrier and ring gear 1:

$$\eta_{CR} = \frac{i_1 - 1}{i_1 - \eta_0} \quad \text{.. (3)}$$

Efficiency between carrier and sun gear 1:

$$\eta_{CS} = \frac{\eta_0 \cdot (i_1 - 1)}{i_1 - \eta_0} \quad \text{.. (4)}$$

Standard efficiency of planetary gear:
$$\eta_0 = \eta_{SP} \cdot \eta_{PP} \cdot \eta_{PR} \quad \text{.. (5)}$$

Here, η_{SP}, η_{PP}, and η_{PR} are the mesh efficiencies between the sun gear and the pinion gear, the pinion gear and the pinion gear, and the pinion gear and the ring gear, respectively. In this report, the theoretical value for each mesh efficiency is assumed to be 98.5 %.

Transmission efficiency in low mode of the toroidal IVT (η_{TM_LOW}) is expressed with the following formula assuming transmission efficiency of the variator is η_V.

$$\eta_{TM\_LOW} = \frac{\eta_{CR} \cdot \{(i_1 - 1) - e_V\}}{i_1 - 1 - \eta_{CS} \cdot \eta_V \cdot e_V} \quad \text{.................................. (6)}$$

The planetary gear mechanism can also be regarded as a 2-input/1-output component in high mode, with efficiency expressed by the following formulas:

Efficiency between sun gear 1 and sun gear 2:
$$\eta_{s1s2} = \eta_0 \quad \text{... (7)}$$

Efficiency between carrier and sun gear 2:

$$\eta_{CS2} = \frac{\eta_0 \cdot (1 - i_{12})}{1 - i_{12} \cdot \eta_0} \quad \text{.. (8)}$$

Standard efficiency of planetary gear: $\eta_0 = \eta_{sp}^2$ ·········· (9)

Transmission efficiency between an input shaft and sun gear 2 (S2) in high mode (η_{12}) is expressed with the following formula:

$$\eta_{12} = \frac{\eta_V \cdot \{\eta_{S1S2} \cdot e_V + \eta_{CS2} \cdot (1 - i_{12})\}}{e_V + \eta_V \cdot (1 - i_{12})} \quad \text{..................... (10)}$$

Power transmission efficiency on the rear side reverse-speed reduction gear is expressed with the following formulas:

Efficiency between sun gear 3 and carrier:

$$\eta_{S3C} = \frac{\eta_0 \cdot i_3 - 1}{i_3 - 1} \quad \text{... (11)}$$

Standard efficiency of rear side planetary gear:
$$\eta_0 = \eta_{SP} \cdot \eta_{PP} \cdot \eta_{PR} \quad \text{... (12)}$$

Transmission efficiency in high mode (η_{TM_HIGH}) for the entire IVT is expressed by the following formula:

$$\eta_{TM\_HIGH} = \eta_{12} \cdot \eta_{S3C}$$
$$= \frac{\eta_V \cdot \eta_{S3C} \{\eta_{S1S2} \cdot e_V + \eta_{CS2} \cdot (1 - i_{12})\}}{e_V + \eta_V \cdot (1 - i_{12})} \quad \text{.................. (13)}$$

3.2 Variator transmission efficiency

Variator efficiency η_V used for the calculation in this report was obtained through experiment. Using a prototype variator, we obtained approximately 95 % transmission efficiency between the input and output disc adjacent to $e_v = 2.0$ (high side) and $e_v = 0.5$ (low side) and approximately 93 % adjacent to $e_v = 1.0$. Transmission efficiency of the variator is relatively lower than that of the gear mesh, confirming that a power split that reduces power transmission through the variator is a suitable target for improving efficiency.

3.3. Measured efficiency of toroidal IVT

We measured power transmission efficiency using the prototype toroidal IVT shown in Fig. 1. Transmission efficiency was obtained by measuring rotational speeds and torque of both input and output. Fig. 4 shows a comparison of experimental results for power transmission efficiency and theoretical efficiency, assuming a constant input torque of $T_{in} = 450$ N·m. It is obvious that the transmission efficiency becomes zero at the geared-neutral point ($e_{TM} = N_{OUT}/N_{IN} = 0$) where the output speed is zero. Efficiency improved as the speed increasing ratio became higher in low mode, exhibiting a maximum 91 % transmission efficiency adjacent to the high-mode switching point ($e_{TM} = 0.46$). In high mode, 82 to 86 % transmission efficiency was observed. The difference between theoretical and experimental transmission efficiency is approximately 2 % in both low and high modes. We infer the difference is due to the fact that the following four factors are not reflected in theoretical transmission efficiency:

1. Loss due to the churning of oil by rotating components inside the transmission.
2. Loss due to drag at the clutch plate for mode selection.
3. Insufficient gear mesh due to deformation of the carrier itself. (Pressure to the rear input disc is transmitted through the carrier in this toroidal IVT. Carrier deformation may worsen the condition of the gear mesh
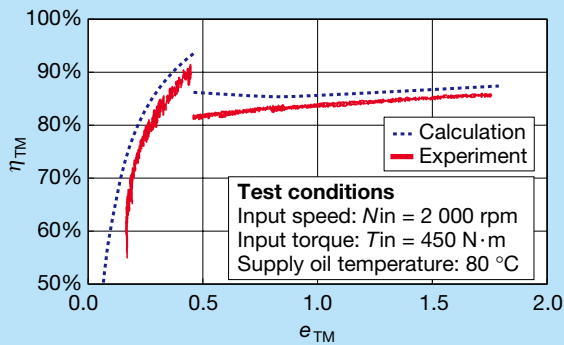
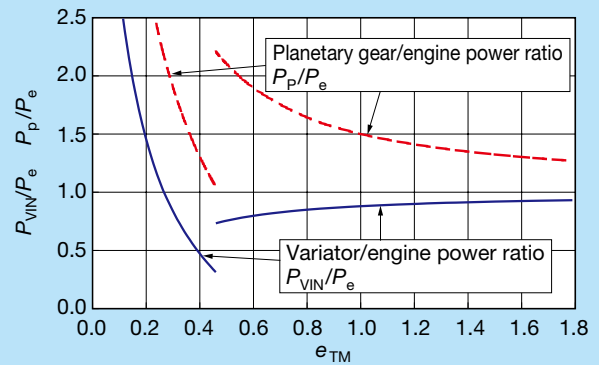Fig. 4 Theoretical and experimental efficiency of an IVT

Fig. 5 Ratio of power transmission of the variator and planetary gear

and impair gear transmission efficiency; therefore, rigidity must be considered when designing carriers.)
4. Loss due to traction oil characteristics.

A study has been conducted that indicates traction oil is designed to increase its traction coefficient under high-contact pressure, which could decrease transmission efficiency over the gear face, which is subject to slip.[3]

Fig. 5 shows power transmitted by a variator and power transmitted by the pinion gear of the planetary gear in comparison with engine power for each speed-increasing ratio. This indicates the power transmitted by the planetary gear is increased particularly on the low-speed side in high mode (e_{TM} = 0.46–0.8) and that gear efficiency substantially affects overall IVT transmission efficiency. Although gear mesh efficiency is assumed to be 98.5 % in this report, a comparison of Figs. 4 and 5 indicates that the difference between the theoretical and measured values of efficiency is higher when the planetary gear transmits higher power, and, therefore, gear mesh

efficiency can be expected to be somewhat lower than what was previously assumed.

Fig. 6 shows an example of a gear layout for even greater improvements in efficiency. We focused on the planetary gear on the rear side for reverse speed reduction in high mode and configured it with lower gear mesh numbers. IVT transmission efficiency is expected to improve as a result of these measures and a review of the power loss factor described above. Fig. 7 shows the theoretical calculation for adopting this gear layout. Efficiency is expected to exceed 92 % for the whole IVT.

4. Geared-Neutral Control

4.1. Torque control

Torque control is a key issue near the geared-neutral point. Torque ratio can be considered as theoretically infinite (∞) in geared-neutral where the speed ratio of the entire transmission becomes zero. In fact, infinite force would not be applied to the component parts since the transmission efficiency of each power-transmitting
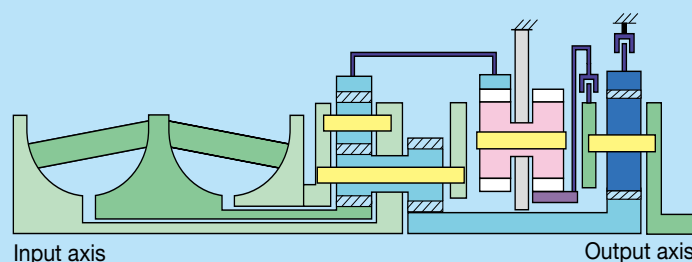

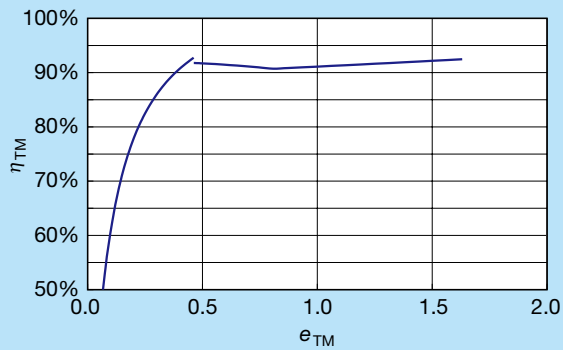Fig. 6 Example of improved gear layout

Fig. 7　Theoretical efficiency of improved gear layout

Fig. 8　Graph of torque control

element, such as the variator and gears, never reaches 100 %. However, it is possible that a torque greater than 10 times the transmission input (engine output) could be generated at the variator or gears. Torque control is an important technology in a geared-neutral mechanism.

Torque control has been studied and achieved by controlling the hydraulic pressure of a hydraulic piston using a pressure control valve to support the reaction force of power-roller transmission.[4] At the same time, the transmission speed ratio control that controls the tilting angle of the power rollers is highly reliable. Commercially available automobiles with a toroidal CVT adopt the transmission speed ratio control method to mechanically control the tilting angle using a cam mechanism. This method is highly compatible with the general transmission ratio map when determining the transmission speed ratio of the transmission when driving. In this report, we propose a new type of torque control method based on controlling the transmission speed ratio.

4.2 Principle of a new type of torque control

The variator exhibits a characteristic called torque shift that generates a variance between the targeted transmission speed ratio and the actual ratio when torque is applied.[5] It is this characteristic that we have utilized to control torque.

Fig. 8 illustrates the concept of torque control using torque shift. The horizontal axis shows the variator speed ratio, while the vertical axis shows output torque (torque acting on the ring gear). The dotted line qualitatively shows the torque shift characteristic of the variator and the change of transmission gear ratio in accordance with the change in torque. Here, a condition in which only a driving force is exerted with no output axis speed (creep)
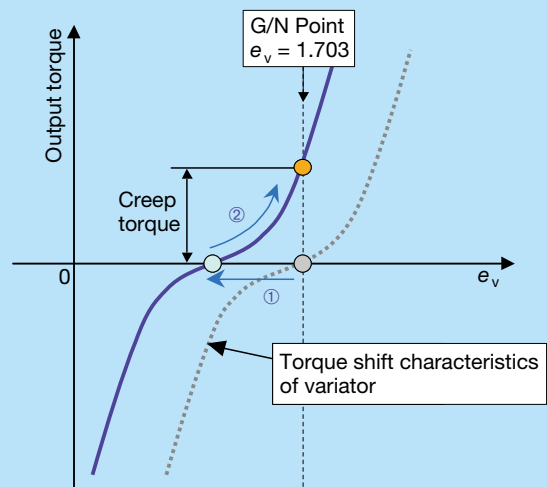
is taken into consideration. The targeted transmission speed ratio is shifted slightly on the reduced-speed side as (1) when driving force in the anterior direction is required. By changing the targeted transmission gear ratio, the characteristic line of the torque shift moves to the left side, as shown by the continuous line. However, the transmission speed ratio of the variator is forced to a geared-neutral point (e_v = 1.703) since the output axis speed is fixed at zero. As shown in (2), torque transmission is induced in the variator, resulting in the induction of creep torque in the output axis. The targeted transmission gear ratio is changed slightly to the increased-speed side to shift the characteristic line in Fig. 3 to the right when creep force is needed in the reverse direction. If this torque shift characteristic is already taken into account, changing speed to a certain degree will induce torque on the variator and a target torque (creep force) can be obtained.

4.3 Hydraulic control circuit

We designed an IVT control mechanism based on the control concept described above. Fig. 9 shows the layout of this geared-neutral control mechanism.

A mechanism with a hydraulic piston is incorporated in a prototype hydraulic circuit to increase the reliability of switching between forward and reverse. A compensation piston activates a link mechanism, while the ratio control valve that adjusts the variator's transmission speed ratio is activated by a stepping motor and the link mechanism. This compensation piston is connected to the manual valve that is connected to a shift lever and moves the link mechanism to a certain degree according to the switch between forward (D: drive) and reverse (R: reverse). The creep force on the forward side (or the reverse side) at vehicle speed zero, based on the principle shown in Fig. 8,

Fig. 9 Geared-neutral control mechanism

is obtained by this small shift of the transmission gear ratio. The compensation piston is a highly reliable system for correctly obtaining forward and reverse motions even in the event of electrical system failure.

We added two compensation controls to the prototype transmission. The extent of motion from the geared-neutral point is corrected by the stepping motor in accordance with oil temperature to compensate for the difference in valve characteristics caused by oil temperature. We also exerted a control to compensate for induced torque by the stepping motor when target torque (creep force) varied from the induced force by monitoring the differential pressure (ΔP) of the control piston. Fig. 10 shows the control flow chart. Highly reliable control of creep force, which can respond to external disturbances such as variation in atmospheric temperature, was possible using these two controls.

4.4 In-vehicle test results

We conducted an in-vehicle verification test with the prototype transmission mounted to a rear-wheel drive sedan with a 4.3-liter engine (maximum torque 430 Nm). Fig. 11 shows the data obtained when shifting from Neutral to Drive and Neutral to Reverse while applying the brake. This shows that transmission output torque is induced steadily in accordance with switching to forward or reverse. In section A of Fig. 11, the stepping motor is activated as the oil temperature compensation control and the differential pressure compensation control in B become functional. Fig. 12 shows data for launching from a standing start under full acceleration in Drive. Output axis torque and vehicle acceleration show good response and rise smoothly. The geared-neutral control operates at near-zero speed and shifts to maximum transmission speed ratio control with the transmission ratio map method after the brake is released and the vehicle starts to move.

Fig. 10 Control flow chart

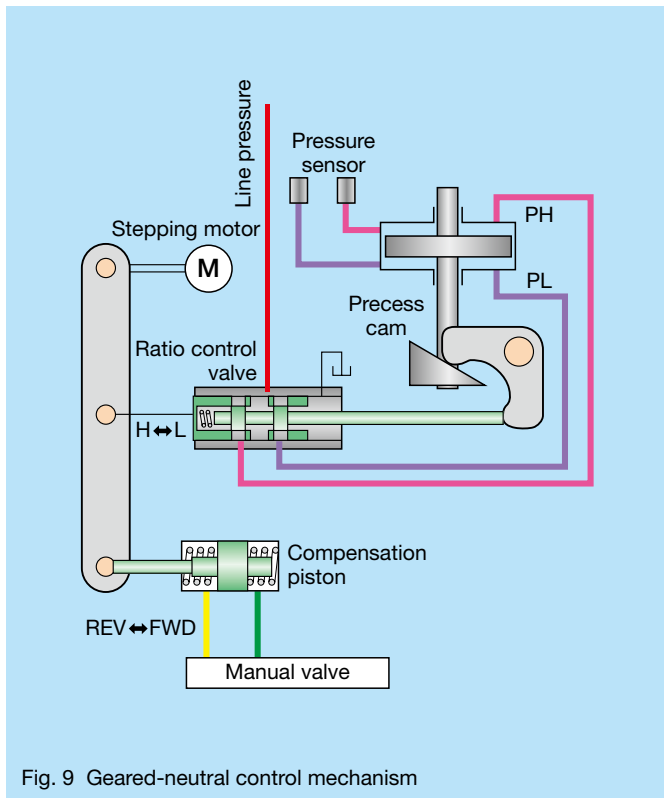**19**   Motion & Control No. 21 (December 2009)   **NSK**

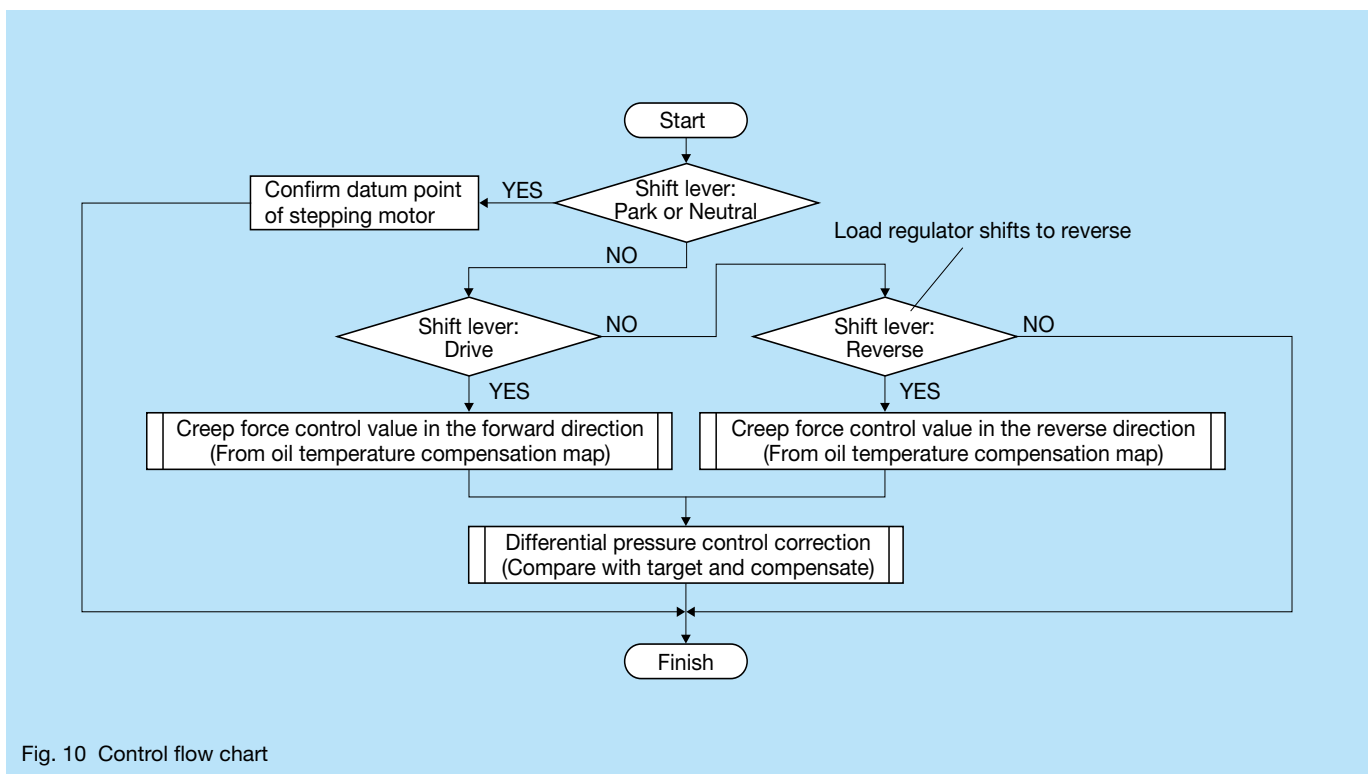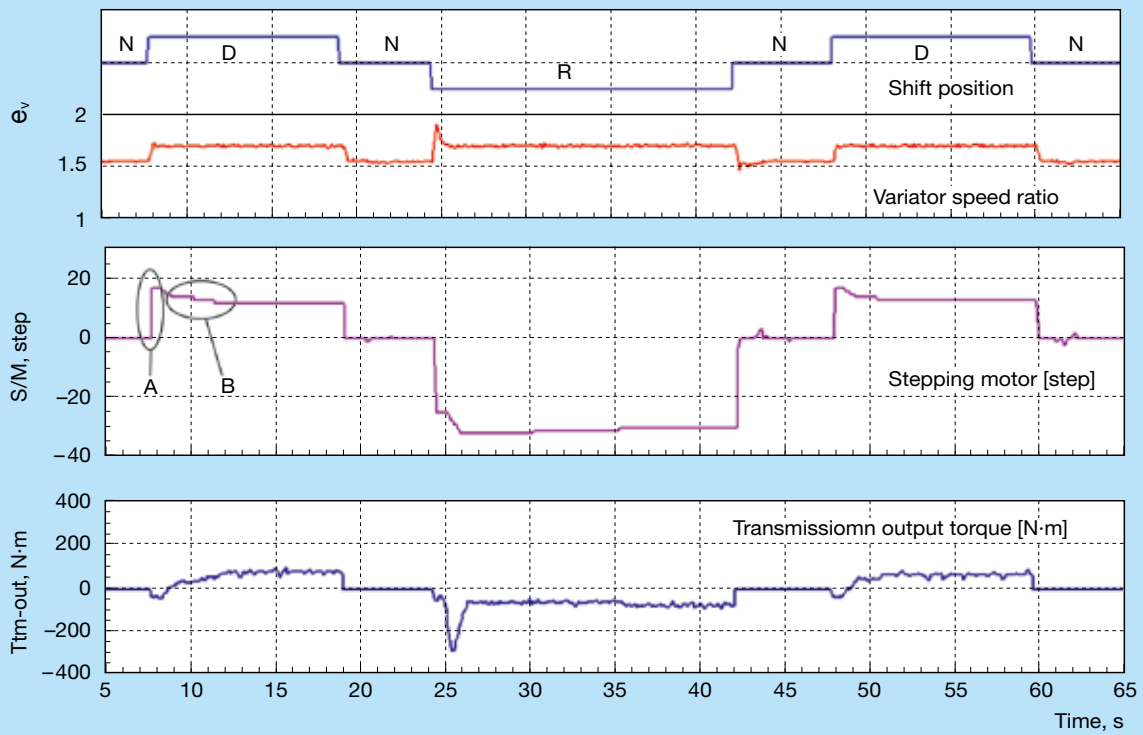

Fig. 10 Control flow chart

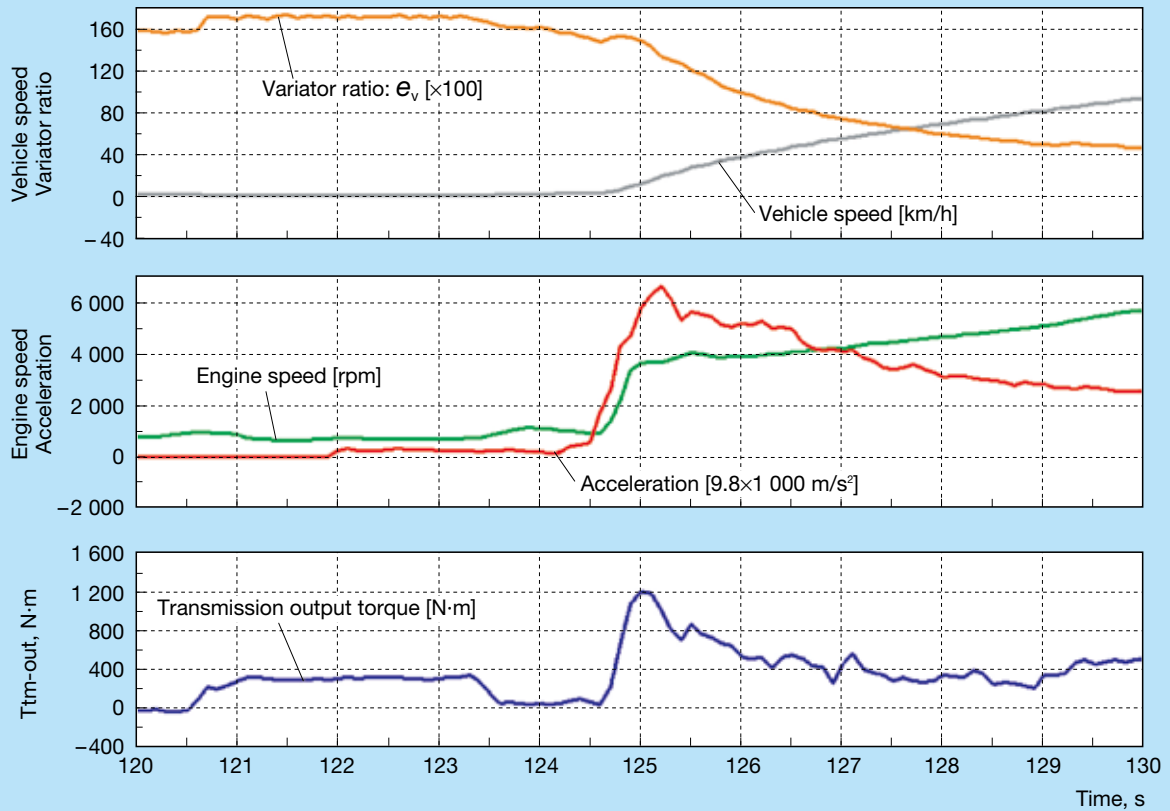Fig. 11 Results of creep force control test under standstill conditions

Fig. 12 Results of vehicle launching test under full acceleration

5. Conclusion

The authors have discussed theoretical transmission efficiency and actual measured efficiency through experiments for a toroidal IVT that adopts a geared-neutral and power-split system as a proposal for next-generation CVTs. We have reported that gear efficiency affects overall IVT efficiency as well as the efficiency of the variator itself, and that gear layout is an important factor to consider in this kind of power recirculation system. We have also proposed a new type of torque control system based on a transmission speed ratio control configuration as a control method at near-zero speed. In-vehicle testing with a prototype transmission established the superior reliability of this method. We believe that this control method makes possible a commercial IVT without a torque converter.

Some parts of this article have been translated and reprinted with permission from JSAE Proceedings of Nos. 9-05 (2005) and 140-06 (2006).

References
1) T. Shinojima et al., "Development of the Next-Generation Toroidal CVT" NSK Technical Journal, 679 (2005) 1–9.
2) M. Morozumi "Design Calculation Method of Planetary Gear and Differential Gear" Sankei Shinbun Syuppan Co., Ltd. (1984).
3) K. Ikejo et al., "Effect of Traction Oil on Power Transmission Loss of Gear" Proceedings of World Tribology Congress (Tottori, November 2004), 531–532.
4) R. D. Fuchs et al., "Full Toroidal Variator Dynamics" SAE 2002-01-0586 (2002).
5) S. Miyata et al., "Study of the Control Mechanism of a Half-Toroidal CVT During Load Transmission" TD-5, Proc of MPT2001-Fukuoka (2001) 844–848.

Takashi Imanishi

Takumi Shinojima

Toshiro Toyoda

Eiji Inoue

Sensor Bearing Development

Tomoyuki Yanagisawa and Makoto Koyama
Mechatronics Technology Development Center

ABSTRACT

We have developed sensor bearings that meet the requirements for high performance and downscaling. The NSK sensor bearing has a structure that integrates sensors with a deep groove ball bearing that are able to detect speed and direction of rotation.

In this article, we report on sensor performance and present reliability test results of this newly developed sensor bearing.

1. Introduction

Recently introduced machinery incorporate a number of high-value-added features, such as enhanced reliability, maintenance-free operation, and compact dimensions. An increasing number of these products include sensor units as an added value. These sensor units play an important role in machinery and are increasingly required to provide enhanced functionality in a compact size. To meet these demands, NSK has developed a sensor bearing with the following features.

1. Ability to detect both rotating speed and direction
2. Compact size
3. Easy mounting

This article provides an overview of this newly developed sensor bearing.

2. Background of Development

2.1 Development concept

NSK has already commercialized hub unit bearings that incorporate rotating speed sensors[1]. However, since applications of hub unit bearings are limited to automobiles, there has been demand for deep groove ball bearings with sensors for use in industrial equipment or home appliances. Demand has also been increasing for incorporating a variety of other information in addition to rotating speed to improve sensor performance.

To meet these demands, we developed a sensor bearing capable of detecting rotating speed and direction using a deep groove ball bearing unit.

2.2. Development objectives

The following objectives were key for achieving development of this bearing.

1. Improve sensor accuracy of rotating speed and direction
   Improve magnetized accuracy of the multipolar magnet and the assembly process of the sensor component in order to deliver satisfactory performance, including pitch accuracy, duty ratio, and phase shift, while also improving detection accuracy.
2. Improve resistance against environmental factors
   Select electrical components, review sensor structure, and verify through reliability tests the resistance of components against external environmental factors that could be expected under actual usage conditions, such as heat, vibration, and shock loads.
3. Improve resistance against external magnetic flux
   Study, and verify through experiments, a magnetic shield structure for improving resistance to external magnetic flux.
4. Improve electromagnetic compatibility (EMC) performance
   Select sensor elements, review electrical filters, and verify electromagnetic compatibility through testing for improving EMC performance.

3. Structure of Sensor Bearing and Sensor Specifications

3.1 Structure

Fig. 1 illustrates the structure of the newly developed sensor bearing, which is also pictured in Photo 1. The structure of the sensor bearing incorporates a function to detect both rotating speed and direction (Fig. 2).

A magnetic sensor that is attached to the outer ring of the bearing (the stationary ring) and a multipolar magnet that is mounted on the inner ring (the rotating ring) are positioned so that they face each other. The multipolar magnet has its N pole and S pole alternately magnetized in a circumferential direction. The magnetic sensor on the outer ring detects the change of polarity as the multipolar magnet on the inner ring rotates, and outputs pulse signals in accordance with the change of magnetic pole. The frequencies of this pulse signal indicate rotating speed.

Two magnetic sensors are arranged in a circumferential direction at a given pitch, as shown in Fig. 2. The pulse signals, which are output from two magnetic sensors and referred to as phase A and phase B, are square waves, as shown in Fig. 3. The positions of the magnetic sensors are adjusted so that the phase shift of phase A and phase B is 90°. As in the case of typical rotary encoders, detecting the state of phase A and phase B reveals the direction of rotation.

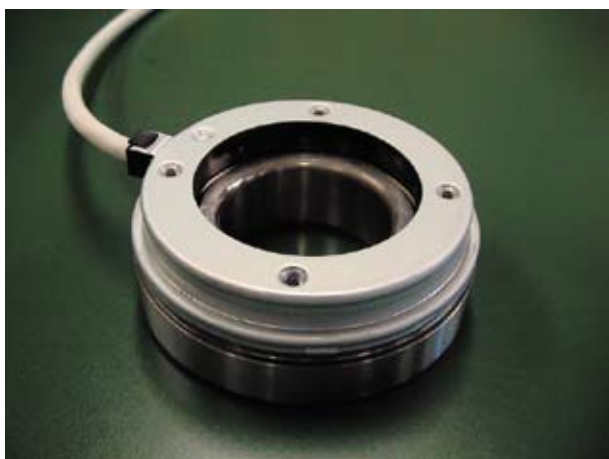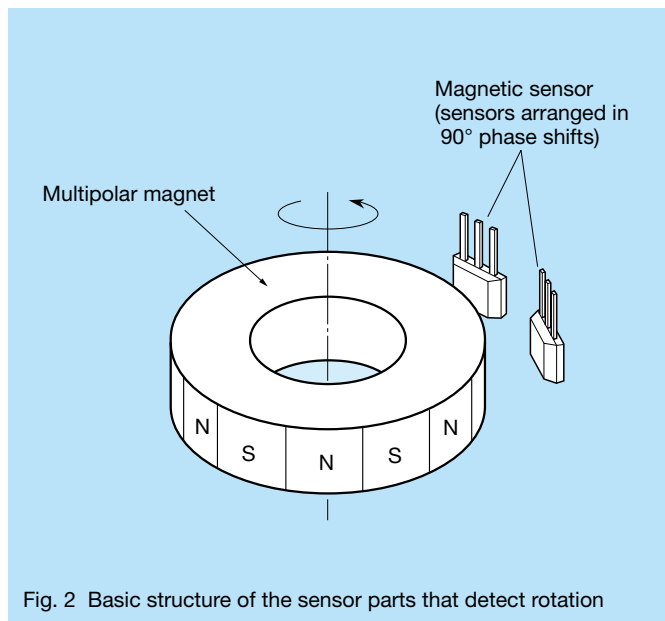Furthermore, an optimized sensor component reduces the influence of external magnetic flux.
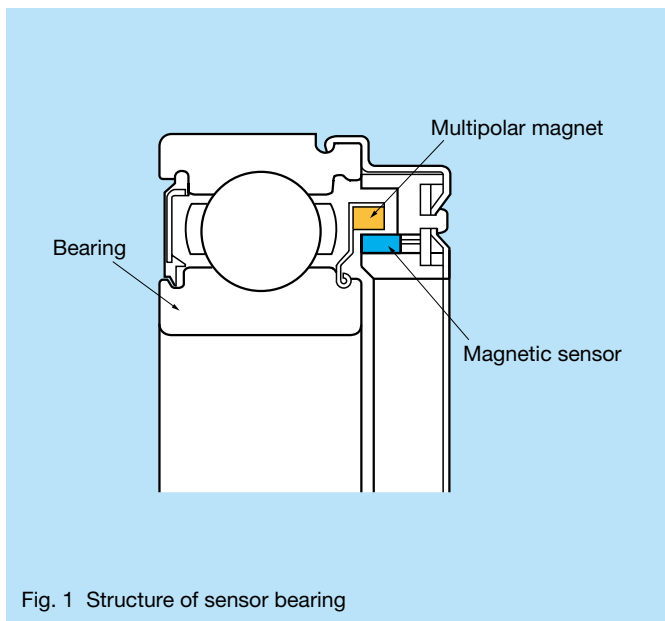
Fig. 1   Structure of sensor bearing

Fig. 2   Basic structure of the sensor parts that detect rotation

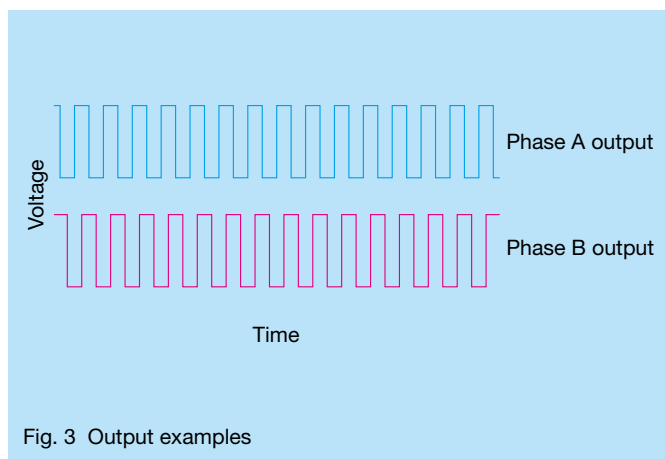Photo 1   Sensor bearing

Fig. 3   Output examples

3.2 Sensor specifications

Table 1 summarizes major sensor specifications.

Output signal waves are square waves of 64 pulses per revolution.

We measured significant factors affecting sensor performance, such as pitch accuracy, duty ratio, and phase shift, using the inspection equipment shown in Photo 2 and a computer that was connected to the equipment. Data obtained by the equipment was processed by the computer and then output in the format shown in Table 2. Measured sensor performance was good and satisfied the specifications in Table 1. The sensor bearing achieved improved accuracy in signal output, such as pitch accuracy and duty ratio, by improving magnetization accuracy and method of assembly.

In addition, values for pitch accuracy, duty ratio, and phase shift are based on a single signal cycle. Fig. 4 shows these relationships. The value for pitch accuracy is used to indicate any discrepancy error (%) by comparing the actual time T_n of one cycle with the ideal time T_{id} of one cycle, while the value for the duty ratio indicates the ratio (%) of time T_p for one pulse length against time T_n for one cycle. Phase shift is the value of the time gap T_{a-b} of the signal rise of phase A and phase B, which is expressed as a phase angle (°).

Table 1   Standard specifications of the sensor

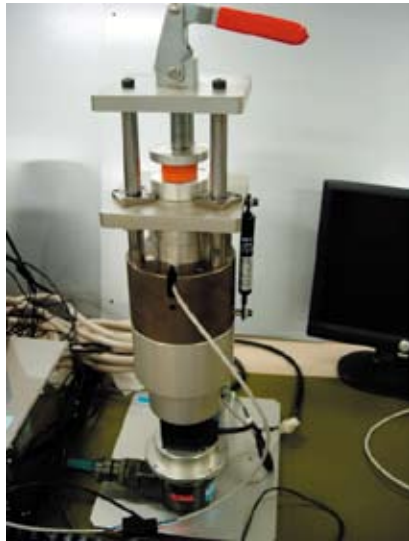| Bearing type	6206
Working temperature range	−40 °C to 120 °C
Number of pulses	64 pulses/rev
Pitch accuracy	± 5 %
Duty ratio	50 % ± 15 % (35 % to 65 %)
Phase shift	90° ± 45°

Photo 2 Inspection equipment for the sensor bearings

● Pitch accuracy (%) = ((Tn − T_{id}) / T_{id}) × 100; T_{id}: Ideal cycle
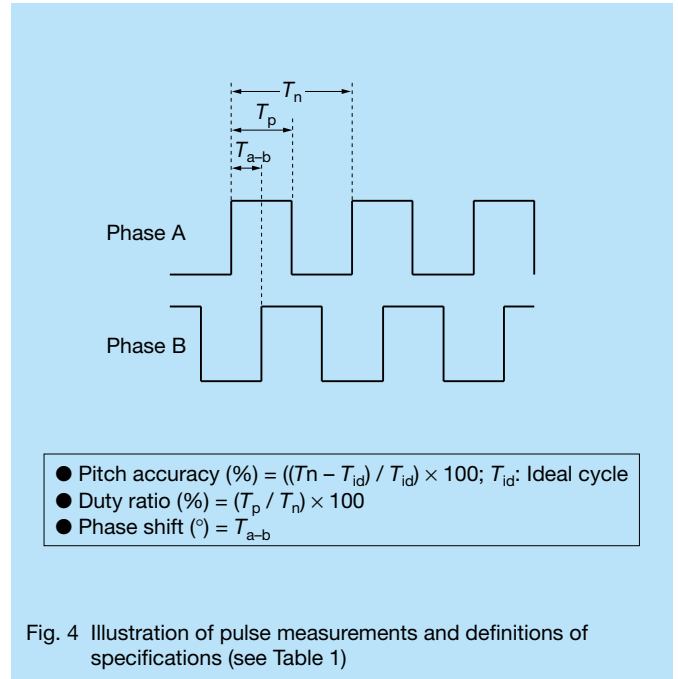● Duty ratio (%) = (T_p / T_n) × 100
● Phase shift (°) = $T_{a–b}$

Fig. 4 Illustration of pulse measurements and definitions of specifications (see Table 1)

Table 2 Example of measurement data

Phase	Phase A			Phase B				
Items	Pitch accuracy, %			Duty ratio, %		A-B phase shift, degree		Result
Criteria	ON	ON		ON	ON	ON	ON	
Standards	5	−5		65	35	135	45	
Number	Max	Min		Max	Min	Max	Min	
002	2.6	−2.5		58.5	54.4	72	59.3	OK
003	2.2	−3.1		53	48.9	91.4	71.8	OK
005	2.2	−4.1		54.8	50.1	102.7	83.1	OK
006	2.1	−2		56	51.8	93.5	78.9	OK

4. Performance Evaluation Test

4.1 Reliability evaluation

Sensor bearings are expected to be used in various environments and therefore should exhibit a level of performance that is sufficiently resistant to external environmental factors.

We conducted various reliability tests for the sensor bearings mimicking actual conditions. Table 3 shows major tested items and conditions. We tested for each condition and examined changes in sensor performance before and after testing.

As an example, Fig. 5 summarizes the measured results of a high-temperature storage test. Sensor performance in such areas as pitch accuracy, duty ratio, and phase shift exhibited virtually no change before and after testing, providing satisfactory results.

Sensor performance under low-temperature storage

tests, heat cycle tests, and vibration tests displayed no significant change that would cause problems between pre- and post-test measurements and appeared satisfactory under all tested conditions.

Table 3 Reliability test conditions

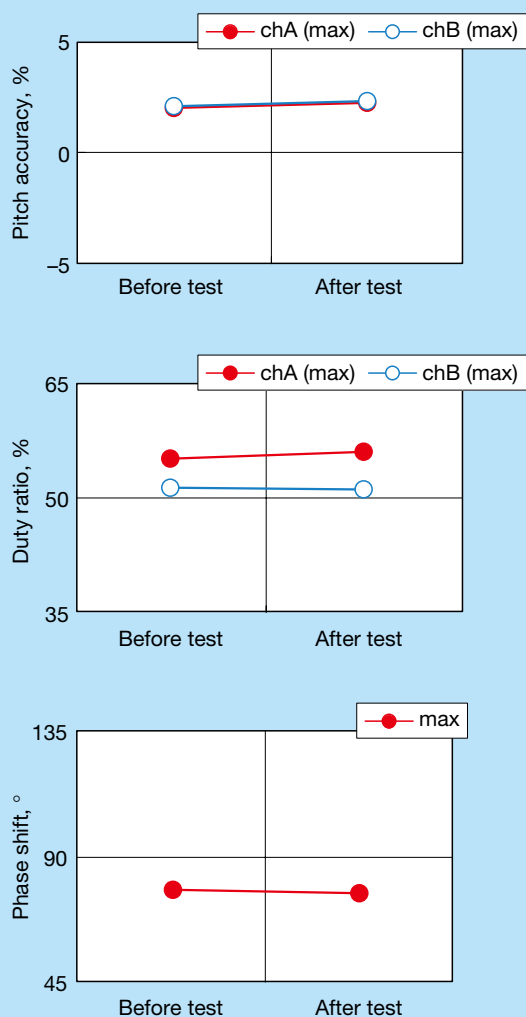| High-temperature storage test	120 °C, 500 h
Low-temperature storage test	−40 °C, 500 h
Heat cycle test	−40 °C to 125 °C, 100 cycles
Vibration test	400 m²/s, 24 h

Fig. 5 Reliability test results—high-temperature storage test

4.2 Electromagnetic compatibility (EMC) evaluation

Electrical equipment is subject to error and malfunction due to external factors such as electrostatic discharge, lightning, and electromagnetic radiation from other equipment. Therefore, it is important for electrical equipment to secure electromagnetic compatibility. Electromagnetic compatibility (EMC) requires measures against emissions (EMI: electromagnetic interference) and measures for immunity (EMS: electromagnetic susceptibility). EMI ensures that the emissions of electromagnetic disturbances are below a given level so as not to affect other equipment, while EMS ensures normal operation even when exposed to electromagnetic disturbances from other equipment. We conducted an EMS test to evaluate the level of resistance of the sensor bearings against external factors (Table 4). This EMS test was based on standards stated in JIS C 61000-4 and IEC 61000-4.

1. Electrostatic discharge immunity test (JIS C 61000-4-2)

   The electrostatic discharge immunity test simulates conditions under which an electrostatic discharge mediated by the human body causes errors or malfunction in electrical equipment.

   This test was conducted using a discharge gun for the electrostatic discharge. We confirmed that the sensor bearings fulfill the performance standards summarized in Table 4.

2. Electrical fast transient/burst immunity test (JIS C 61000-4-4)

   The electrical fast transient/burst immunity tests simulate conditions under which transient noise entering through a power source cable or signal cable causes errors in electrical equipment.

   In this test, we induced noise in a cable using a capacitive coupling clamp and confirmed that the sensor bearings met the performance standards shown in Table 4.

Table 4 EMC test items and test results

Items	Test level (criteria)	Results
Electrostatic discharge immunity test (JIS C 61000-4-2: IEC 61000-4-2)	Contact discharge ± 4 kV, Air discharge ± 8 kV (Criterion B)	Pass
Radiated, radio-frequency, electromagnetic field immunity test (JIS C 61000-4-3: IEC 61000-4-3)	Electric field strength: 10 V/m; Frequency range: 80 MHz to 1 000 MHz (Criterion A)	Pass
Electrical fast transient/burst immunity test (JIS C 61000-4-4: IEC 61000-4-4)	Voltage peak: 1 kV, Repetition rate: 5 kHz (Criterion B)	Pass
Immunity to conducted disturbances, induced by radio-frequency fields (JIS C 61000-4-6: IEC 61000-4-6)	Voltage level: 10 V; Frequency range: 150 kHz to 80 MHz (Criterion A)	Pass
Power-frequency magnetic field immunity test (JIS C 61000-4-8: IEC 61000-4-8)	Magnetic field strength: 30 A/m, Frequency: 50/60 Hz (Criterion A)	Pass

We also confirmed that the sensor bearings fulfilled the performance standards in Table 4 for a radiated, radio-frequency, electromagnetic field immunity test, immunity to conducted disturbances, induced by radio-frequency fields, and a power-frequency magnetic field immunity test. The results of these tests confirmed that the sensor bearing displayed appropriate EMC performance under actual conditions.

5. Conclusion

The sensor bearing was developed as a deep groove ball bearing unit capable of detecting rotating speed and rotating direction, satisfies JIS standards as verified through various performance tests, and was confirmed to possess sufficient specifications for use in various mechanical equipment, such as industrial equipment or home appliances. This sensor bearing is expected to improve the performance of various mechanical equipment as a unit with sensor functionality. We will continue to enhance the accuracy of the sensor and continue developmental efforts that meet user needs.

Reference
1) J. Sakamoto, "Trends and New Technologies of Hub Unit Bearings" NSK Technical Journal, 677 (2004), 2–10.

Tomoyuki Yanagisawa

Makoto Koyama

Development of a High-Output Brushless DC Motor for EPS

Toru Sakaguchi and Shuji Endo
Steering Technology Center, Electronic Control Development Department

ABSTRACT

In recent years, electric power steering (EPS) systems have been installed in vehicles for the purpose of reducing energy consumption due to an increasing awareness of greenhouse gasses and their impact on the environment. The application of EPS systems has expanded to include C- and D-segment platforms, which require EPS from the aspect of a compact and lightweight design. These platforms require an EPS system that operates quietly and with low torque fluctuations.

For the newly developed column-type EPS, NSK has developed lightweight, high-output brushless DC motors in a compact package that take advantage of NSK's control technology, which enables quiet operation with low torque fluctuation characteristics. Mass-production of this EPS system began in 2004, and it has been mounted on C-segment platform vehicles. This article reports on these brushless DC motors and applicable control technologies.

1. Introduction

An increasing number of electric power steering (EPS) systems have been installed in recent years in response to increasing concern over the global environment and energy conservation. The range of installation possibilities has even been extended to C- to D-segment platforms. This has been achieved by solving technical issues that accompany the higher output of EPS. One of these issues has been developing a suitable brushless DC motor for EPS systems.

Motors used for EPS must carefully balance certain characteristics and make highly sophisticated trade-offs in regard to motor design, such as compact size, high output, low noise, low-torque ripple, and low friction.

NSK has thus established an approach that integrates motor design and control technologies and successfully developed a high-output, brushless DC motor for EPS. A column-type EPS (Photo 1) using this motor was mounted on C-segment platform vehicles, which went into mass-production in 2004.

Photo 1 Column-type EPS

This article introduces the features of the newly designed high-output, compact, and lightweight brushless DC motor, and the control technologies used to achieve low noise and low-torque ripple for this motor.

2. Motor Development Concept

Fig. 1 shows the performance requirements for motors used in EPS systems, which include low-torque ripple, low friction, and low noise. The motor performance requirements shown here are recognized as trade-offs for increasing output and reducing size. Using simulations in this environment of supposed trade-offs, we combined conventional design with control technologies for evaluating design sensitivity. Thus, we were able to develop an optimal motor design for an EPS system.

In general, a square-wave motor is better than a sine-wave motor in terms of high output and compactness. On the other hand, a sine-wave motor is better in terms of low-torque ripple. We recently developed a vector control for a square-wave motor in order to control torque ripple that is based on a square-wave motor, which is suitable for downscaling and higher output. Furthermore, we incorporated cost advantages by using a Hall IC for estimating position as is required for vector control.

3. Brushless DC Motor for EPS

Fig. 2 shows a cross-sectional view of the brushless DC motor.

We tried to increase output and reduce the size and weight of the motor by utilizing a high-energy density, rare earth magnet. Moreover, a rare earth magnet reduces electric current, which facilitates a smaller heat sink for heat dissipation, thus enabling further downscaling of the ECU.

We also sought to reduce torque ripple generated by variation in the magnetization waveform by utilizing ring magnets that have a consistent magnetization waveform.

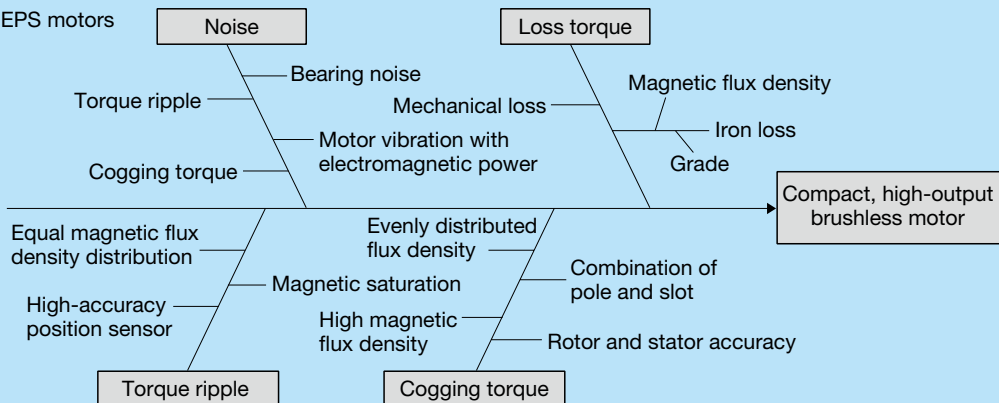Table 1 shows a comparison of a brushless motor

Fig. 1 Cause-and-effect diagram of the brushless motors and the performance requirements of the EPS motor

(BLSM) that produces sine wave back electromotive force (EMF) and the newly adopted brushless DC motor (BLDCM) that produces a quasi-square-wave back EMF. As shown in Table 1, the peak current value of BLDCM is lower when the same output is sought at the same peak of back EMF. The BLDCM's back EMF is also smaller when the peak value of the electric current is the same. This means that a smaller, lighter motor with high output was achieved by using the quasi-square-wave for the back EMF waveform, which contributed to reducing the size of the magnet. Fig. 2 lists motor sizes and rated torques. Fig. 3 summarizes system output and motor inertia values.

A Hall IC was used as the sensor for detecting motor

rotor position in consideration of its superior cost advantage. The positional resolution of the Hall IC was not sufficiently accurate for vector control. Therefore, in order to compensate, we developed a technology for highly accurate position estimation. This technology achieved a low-torque ripple and low noise at both low- and high-speed rotation. Section 4.2 provides the details of this function.

4. Brushless DC Motor Control for EPS

4.1 Vector control for square-wave motor

The sine-wave motor does not generate torque ripple with sine wave current flow. However, the newly adopted square-wave motor includes the third and fifth harmonic waves as well as the fundamental (first) wave, as shown in Table 1. Therefore, torque ripple is induced unless an appropriate current waveform is generated and applied.

Subsequently, we developed a method for generating current waveforms without generating torque ripple. This principle is outlined below. Equation (1) expresses the motor as:

$$T \cdot \omega = e_a \cdot i_a + e_b \cdot i_b + e_c \cdot i_c = \frac{2}{3} (e_q \cdot i_q + e_d \cdot i_d) \ \cdots\cdots (1)$$

where,

T: Required torque
ω: Motor angular velocity
e_a, e_b, e_c: Back EMF of phase A, phase B, and phase C
e_q, e_d: Back EMF of q-axis and d-axis
i_a, i_b, i_c: Current of phase A, phase B, and phase C
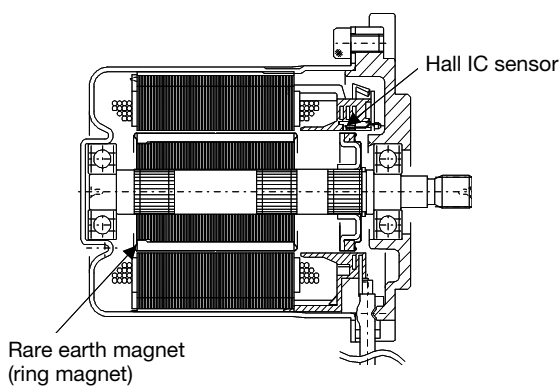i_q, i_d: Current of q-axis and d-axis

Fig. 2 Cross-sectional view of an EPS motor

Table 1 Comparison of the waveform between square-wave control motors (NSK BLDCM) and sine-wave control motors (BLSM)
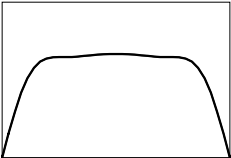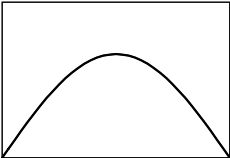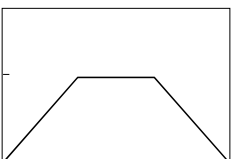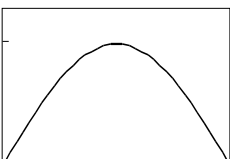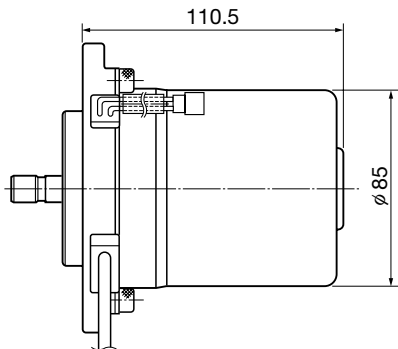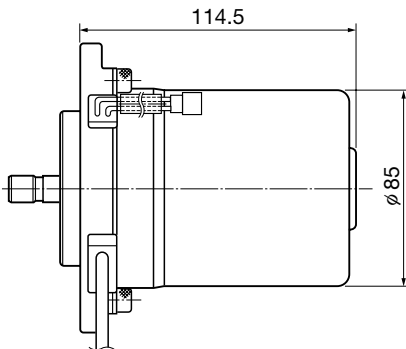
Items	Square-wave control motor (NSK BLDCM)	Sine-wave control motor (Other manufacturer's BLSM)
Back EMF waveform	1st, 3rd, and 5th harmonic components included	1st wave component only
Current waveform		

Table 2 Specifications of the NSK BLDCM series

Motor size, mm	⌀85 × 110.5	⌀85 × 114.5
Shape		
Rated torque, N·m	4.2	4.6
Rated rotational speed, rpm	1 040	950
Voltage, V	12	

Equation (2) is obtained by solving equation (1) for i_q.

$$i_q = \frac{\frac{3}{2} T \cdot \omega - e_d \cdot i_d}{e_q} \quad \cdots\cdots\cdots\cdots (2)$$

The values of e_q and e_d can be obtained by fixing the harmonic wave content ratio. Therefore, the value of i_q, which does not induce torque ripple, can be obtained by equation (2) once the values of T, ω and i_d are identified. The 3-phase current value can be obtained by 2–3 phase conversion of the i_q value and the i_d value.
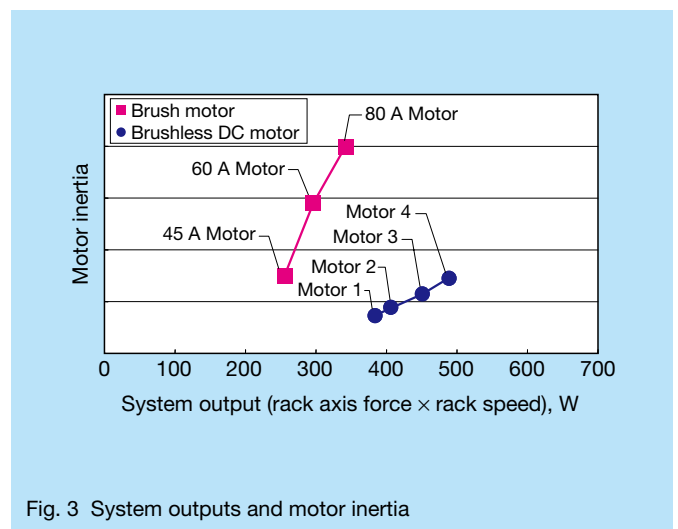

Fig. 3 System outputs and motor inertia

4.2 Rotor position estimation feature

Values e_q and e_d in equation (2) explained in 4.1 are a function of rotor position θ, and are expressed as $e_q(\theta)$ and $e_d(\theta)$. Therefore, accurate rotor position information is necessary for vector control using current command generation without inducing torque ripple.

The new motor must incorporate a rotor position estimation function to estimate the position of the rotor with a high degree of accuracy because it uses a low-resolution Hall IC as the rotor position sensor.

Rotor position estimates are conducted by estimating the back EMF from the motor current and motor terminal voltage and integrating them, as shown in equation (3).

$$\hat{\theta} = \int \hat{\omega} \cdot \mathrm{d}t = \int (V - R \cdot i) \, \mathrm{d}t = \frac{V^2}{2} - \frac{R}{2} i^2 + C \quad \cdots\cdots (3)$$

where,
θ: Rotor position
$\hat{\ }$: Estimated values
V: Motor terminal voltage
R: Motor resistance
i: Current
C: Integration constant

First, signals from the Hall sensor for each control cycle are detected to confirm whether there is any change in the pattern of the Hall sensor. Then, the accurate position can be obtained at the time the change occurs, so values C and R in equation (3) can be corrected by this accurate information.

Fig. 4 is a schematic that explains this position estimation function. Back EMF is estimated and calculated from the motor terminal voltage and current value. This value is then integrated to calculate estimated rotor position value $\hat{\theta}$. Resistance error ΔR is calculated by comparing position information obtained by the Hall sensor signal and the estimated value to correct model resistance value R_n, which estimates the back EMF.

Model resistance value R_n is corrected for each phase as each phase exhibits variation in resistance. Fig. 5 shows simulated results indicating the convergence of resistance values when initial resistance errors are applied to each phase.
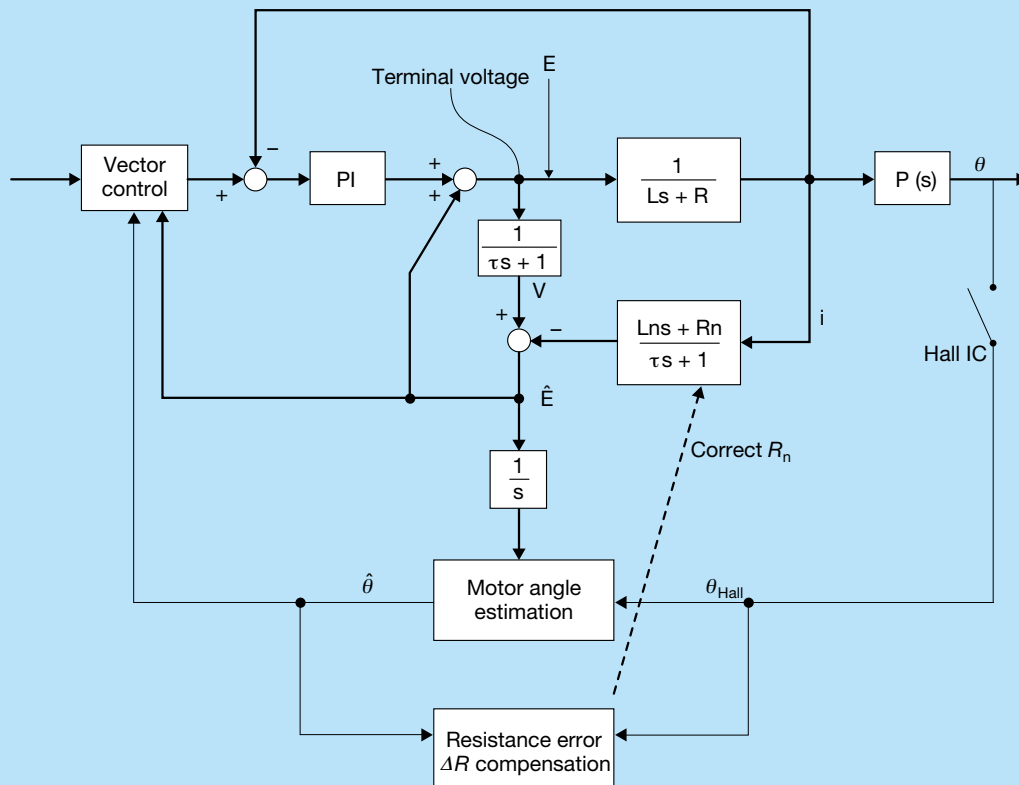

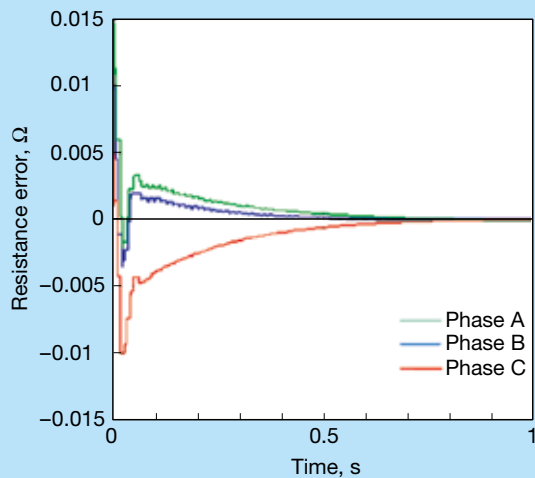Fig. 4 Schematic for estimating the angular position of a rotor

Fig. 5 Simulation results of resistance error convergence

4.3 Structure of vector control for a square-wave motor

4.3.1 Switching between square wave control and vector control

The position estimation function was explained in 4.2, but major errors can occur in the low-speed rotation range. Additional issues include torque ripple as well as noise, which are generated with vector control. Therefore, this brushless DC motor control adopts a method that switches control types in accordance with rotational speed as shown in Fig. 7. In the low-speed rotation range (I), position estimation error can be large, such that square wave control should be used instead of vector control. In the middle-speed rotation range (II), we apply vector control using estimated rotor position. However, we do not apply field-weakening control in order to prevent sound quality deterioration, which is caused by a high harmonic current wave that could be introduced due to the field-weakening control. In the high-speed rotation range (III), vector control is used and field-weakening control is also implemented to prevent voltage saturation. This is because voltage saturation distorts the current flow. It is this distortion that induces torque ripple and noise.

This brushless DC motor succeeds in meeting the challenges related to torque ripple level, sound performance, and output characteristics (rotational speed – output torque) by appropriately switching the type of control in accordance with rotational speed, as described above. Fig. 8 shows the control schematic that is used. Control is switched between square wave control and vector control depending on rotation angular velocity ω at the control-switching block. Details for the square wave control and the vector control are described below in sections 4.3.2 and 4.3.3.

Fig. 6 displays test results of estimated rotor position values when the resistance error at the time the Hall sensor pattern change was corrected and also the values when it was not corrected. It indicates that the rotor position is accurately estimated throughout all electrical angles (360 degrees) with the correction of resistance errors at the time the Hall sensor pattern changes at each 60-degree electrical angle interval.
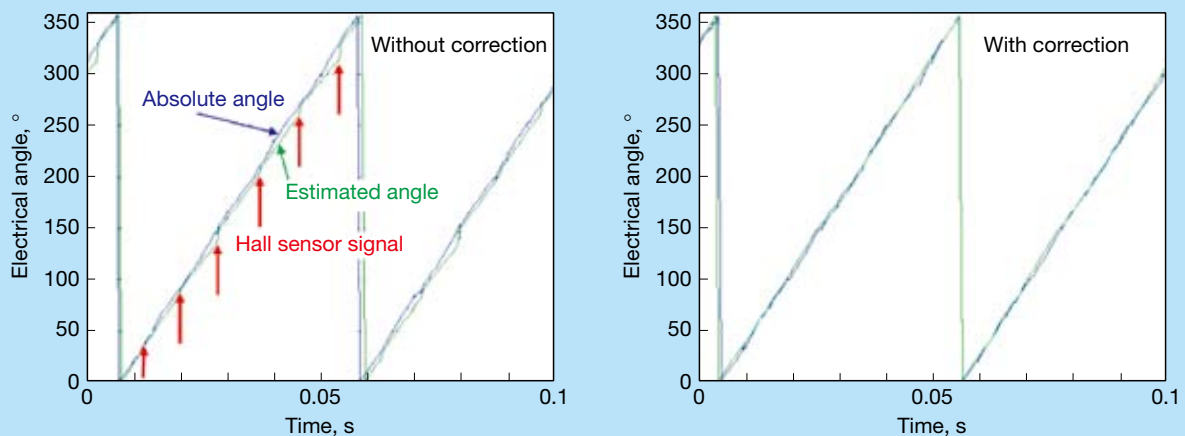

Fig. 6 Comparison of the angular position of a rotor estimated by the system
(left: without correction, right: with a correction using a Hall IC signal)

Fig. 7 NSK BLDCM control method

4.3.2 Square wave control

The low-speed rotation range is subject to significant position estimation error, and so we adopted square wave control (120 degrees excitation) instead of vector control. However, transient response of commutation when switching excitation phases at each 60-degree electrical angle interval occurs with 120 degrees of excitation. Torque ripple is induced as a result of this transient response, which is attributable to the fact that the response time of the electric current is longer in the rising phase and shorter in the decay phase, so that changes in the current in the commutation phase cannot be compensated, and the combined torque of these three phases varies because the current is affected and varies
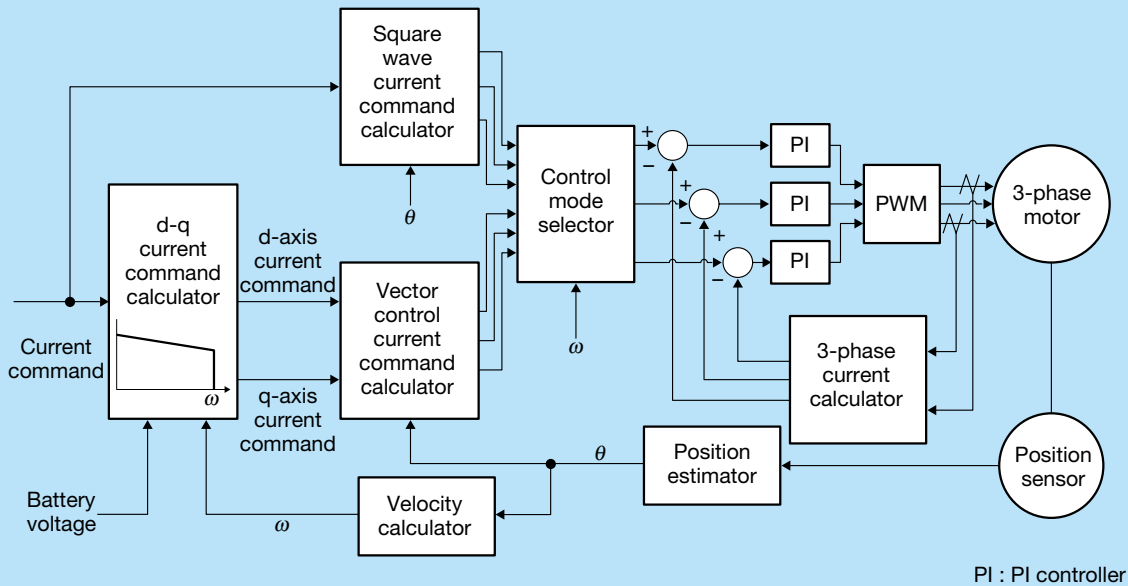
Fig. 8 Schematic of the current control for changing control methods

Fig. 9 Conventional square wave control

Fig. 10 NSK square wave control

even in the phases that are not commutating (Fig. 9). This brushless DC motor control is configured to generate current commands to match the current variation of the commutation phase and to perform electric current feedback control to solve this problem. Fig. 10 shows the current waveform and the torque ripple in this control configuration. Compared with Fig. 9, the torque ripple level is significantly improved by this control configuration.

4.3.3 Vector control

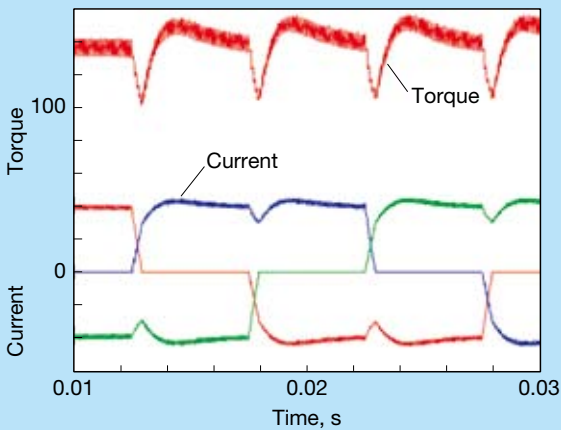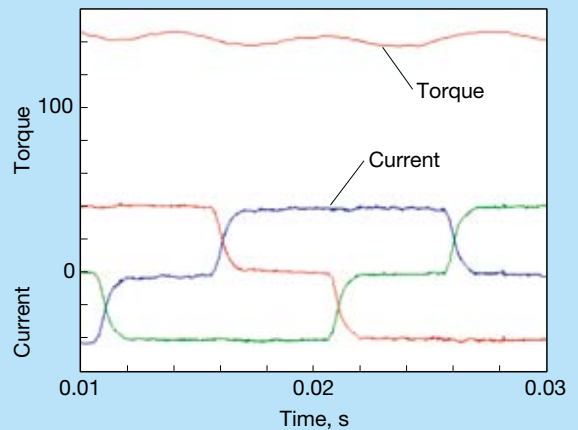The vector control used in the middle- and high-speed rotation ranges is based on the estimated rotor position information explained in 4.2 and an electric current waveform that does not induce torque ripple, as explained in 4.1.

The rotor position explained in 4.2 is estimated in the "Position estimator" block in Fig. 8. In addition, the 3-phase current waveform that does not induce torque ripple explained in 4.1 is generated in the "Vector control current command calculator" block. Furthermore, in the "d-q current command calculator" block, an electric current command value of d-q axis that does not induce voltage saturation is generated from motor output characteristics, battery voltage, and motor angular velocity.

4.4 Current controller

Normally, the vector control of a 3-phase motor is based on the deviation of the electric current command value and the motor current value along the d-q axis (Fig. 11). However, this brushless DC motor adopts the current feedback control method for each phase. The reasons for

this are provided below.

The motor voltage characteristics equation is expressed in (4).

$$
\begin{cases}
V_{an} = R_a \cdot i_a + L_a \cdot \dfrac{d i_a}{d t} + E_{an} \\[2mm]
V_{bn} = R_b \cdot i_b + L_b \cdot \dfrac{d i_b}{d t} + E_{bn} \\[2mm]
V_{cn} = R_c \cdot i_c + L_c \cdot \dfrac{d i_c}{d t} + E_{cn}
\end{cases}
\quad \cdots\cdots\cdots\cdots\cdots\cdots\cdots\cdots\cdots (4)
$$

where,

V_{an}, V_{bn}, V_{cn}: Voltage of phase A, phase B, and phase C from neutral point

E_{an}, E_{bn}, E_{cn}: Back EMF of phase A, phase B, and phase C from neutral point

R_a, R_b, R_c: Motor resistance of phase A, phase B, and phase C

L_a, L_b, L_c: Motor inductance of phase A, phase B, and phase C

Interference is induced between the three phases; and electric current distortion in one of the phases that affects the other two phases since the three phases coincide at the neutral point. Moreover, the resistance values of the motor and driving device are not identical and exhibit variation. Therefore, interference cannot be sufficiently suppressed when controlled along the d-q axis, which leads to the generation of torque ripple and noise.

This brushless DC motor adopts a control method for generating feedback current in each phase to minimize
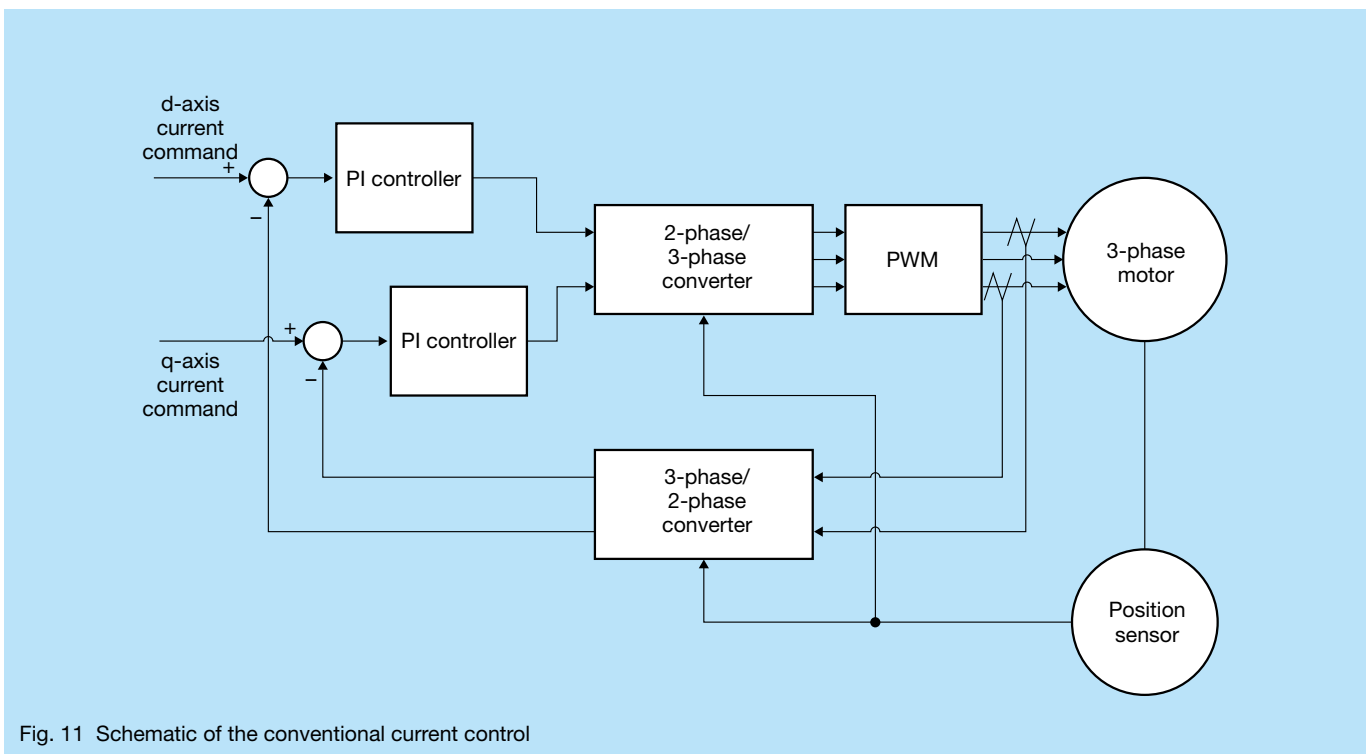
Fig. 11 Schematic of the conventional current control
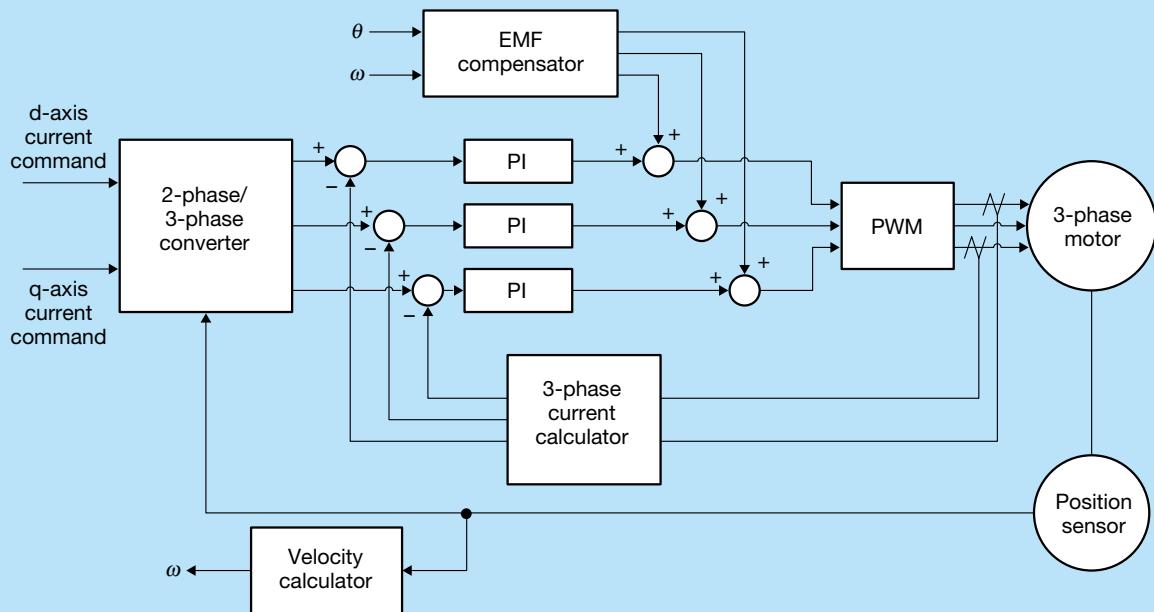
Fig. 12 Schematic of NSK BLDCM current control

the effect of this interference (Fig. 12). The motor is also highly capable of shaping an effective current that follows the current command value by feed-forwarding to each phase in order to compensate for the back EMF induced in each phase and to prevent noise and torque ripple, even at high-speed rotation.

4.5 Design adopting electromagnetic field analysis and control simulation

We established an integrated design environment to facilitate simulations that coordinate motor design and control in developing a high-output brushless DC motor for EPS systems.

Fig. 13 summarizes this integrated design environment.
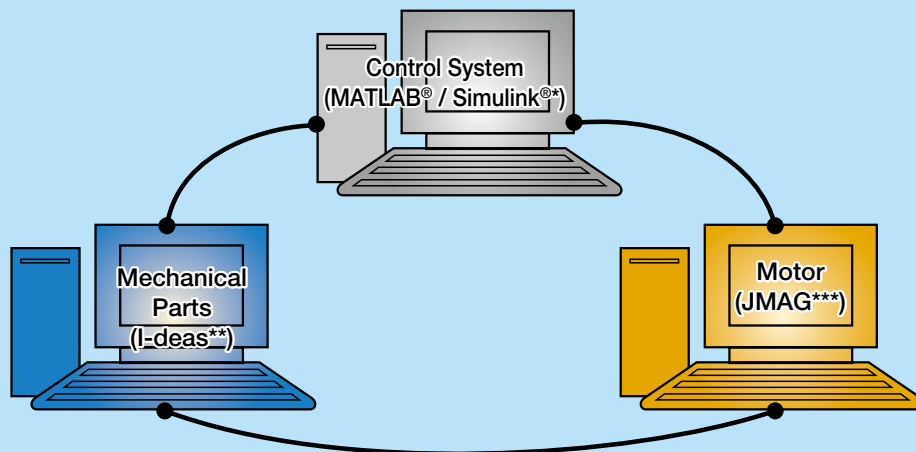
Fig. 13 Integrated design environment
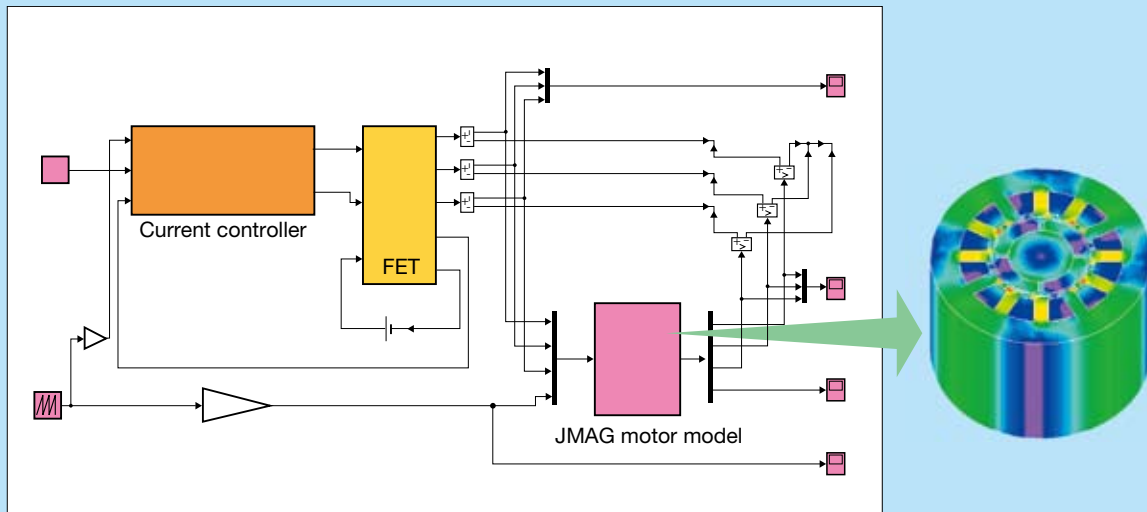
Fig. 14 Optimum design using integrated simulation of motor design and control method design

Based on simulations conducted in this environment, we can evaluate design sensitivity by combining control technology with performance requirements that can be trade-offs in motor design, enabling an optimized design for the brushless DC motor for EPS (Fig. 14).

5. Conclusion

We established an integrated design environment to enable simulations that coordinate motor design and control. This design environment enabled us to develop a control technology for achieving low noise and low-torque ripple, as well as a high-output brushless DC motor for EPS systems that utilize this technology. We intend to continue development efforts to meet the needs of the times in such areas as higher output, lightweight design, compactness, and low noise.

Toru Sakaguchi

Shuji Endo

Development of Bearings for Robots in Vacuum Environments

Masachi Hosoya, Tadahiko Sakamoto, and Hiroyuki Ito
Mechatronics Technology Development Center

ABSTRACT

Robots in vacuum environments can be used to handle and transfer silicon wafers or flat panel display substrates. The bearings used in such robots are required to have superior outgassing performance and a long service life. NSK has developed bearings treated with a DFO thin-film lubricant for use in robots and equipment used in clean and vacuum environments. These bearings undergo precision cleaning using ultrapure water and are shipped in extra-clean packaging.

In this article, we will discuss the low-outgassing performance, long-life characteristics, and strengths of the newly developed bearings. The effects of an improved cage on extending bearing life are also introduced in this report.

1. Introduction

Silicon wafers and flat panel display (FPD) substrates undergo a lamination process that forms thin films with different properties during the manufacturing process.[1] Whereas this process is conducted in a vacuum environment, the robots that are used to transfer the wafers or FPDs are subjected to the same vacuum conditions as the material that they are handling. With each passing year, micropatterned wafer fabrication becomes increasingly complex—requiring ever-higher vacuum conditions. Consequently, robot bearings used in high vacuum environments must offer lower outgassing and lower particle-emission performance. Fluorine grease, which is widely used as a bearing lubricant for robots in vacuum environments, makes it difficult to meet the lower outgassing requirements. For this reason, bearings coated with fluorine oil are sometimes used as a measure against outgassing. However, there are many cases where bearing durability is insufficient. Additionally, the lamination process for FPDs tends to require higher operating temperatures. Robot bearings for such operations must further provide superior low outgassing, low particle emissions, and durability for such high-temperature operating conditions.

To meet these requirements, NSK developed a new robot bearing for vacuum environments, which adopts DFO thin-film lubrication technology for superior low-outgassing performance. In this paper, we report on various characteristics of these DFO treated bearings.

2. Bearings for Robots in Vacuum Environments

2.1 Types of bearings for vacuum environments

Fig. 1 shows the layout of a robot that is used for transferring wafers. The robot transfers wafers from a process chamber to another chamber by extending and retracting an arm and by rotating at the central hub of the robot assembly. The bearings for robots in vacuum environments are used in the joints of the arms and in the rotating parts of the robot assembly's central hub. Typically, angular contact ball bearings, deep groove ball bearings, and four-point contact ball bearings are used. Because the robot must be as compact and as lightweight as possible, thin-section ball bearings are often used. These bearings have an extremely thin cross-section in comparison with their bore diameters.[2] Some bearings use the same type of cage that is found in conventional bearings, while some thin-section ball bearings use spacer balls instead of a cage.

A thin-section angular contact ball bearing treated with DFO thin-film lubricant and a four-point contact ball bearing are shown in Photo 1.
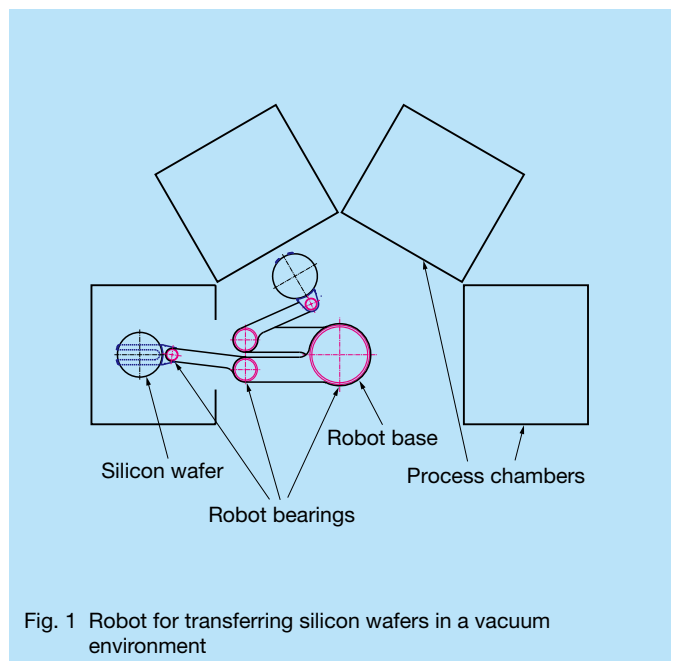

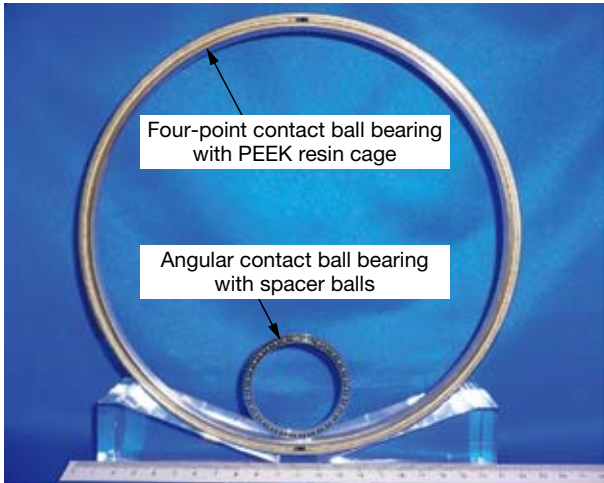Fig. 1 Robot for transferring silicon wafers in a vacuum environment

Photo 1 Newly developed thin-section DFO treated bearings for robots

2.2 DFO lubricant film for vacuum environments

DFO lubricant film for vacuum environments provides bearings with superior low-outgassing performance.[3), 4)]

Rolling contact surfaces of the bearing are treated with a DFO lubricant film, which employs lubrication oil that exhibits very low saturation vapor pressure. There are two types of DFO lubricant films: E-DFO and V-DFO. E-DFO has a lower vapor pressure than other types of synthetic hydrocarbon oils. V-DFO uses a kind of fluorine oil as the base oil. While E-DFO has far lower outgassing rates and higher durability than V-DFO, V-DFO offers superior chemical resistance. E-DFO and V-DFO thin-film lubricant are used depending on the needs of the application.

Table 1 shows comparisons of properties for E-DFO, V-DFO, fluorine grease, and fluorine oil, which are lubricants that are currently used in robot bearings for vacuum environments.

Table 1 Lubricant properties for vacuum environments

Lubricant	E-DFO	V-DFO	Fluorine grease	Fluorine oil
Base oil	Hydrocarbon oil	Fluorine oil	Fluorine oil	Fluorine oil
Outgassing performance	Excellent	Good	Poor	Fair
Particle-emission performance	Good	Good	Good	Fair
Durability	Good	Good	Excellent	Fair
Chemical resistance	Fair	Excellent	Excellent	Excellent

3. Bearing Characteristics

3.1 Outgassing rates

Outgassing rates are indicated by the amount of outgassing per unit of time. Outgassing rates can be measured directly, but the more common method of measuring outgassing rates is to employ the throughput method, which requires a test chamber and a pumping chamber separated by an orifice of known conductance. The amount of outgassing from the bearing (Q) can be obtained in the following equation from the difference of pressure ($P1–P2$) at the orifice.[5)]

$$Q = C \ (P1–P2)$$

where C is conductance at the orifice.

We measured the outgassing rates of E-DFO and V-DFO thin-film treated bearings, and bearings packed with fluorine grease. Due to limitations of the test equipment, the test bearings consisted of small diameter, 608 deep groove ball bearings (8 mm × 22 mm × 7 mm).

Fig. 3 shows the measurement results of outgassing rates.[4)]

The figure shows that the amount of outgassing increases with the increase of temperature. Furthermore, the outgassing rates of both the E-DFO and V-DFO treated bearings were smaller than that of the bearing packed with fluorine grease. The outgassing rate of the E-DFO treated bearing was reduced by about 9/10 that of the bearing packed with fluorine grease under the same high-temperature conditions of up to 100 °C.

Outgassing from the bearing was mostly emitted from the lubricant, but there are some cases in which the organic contaminants on the bearing surface caused
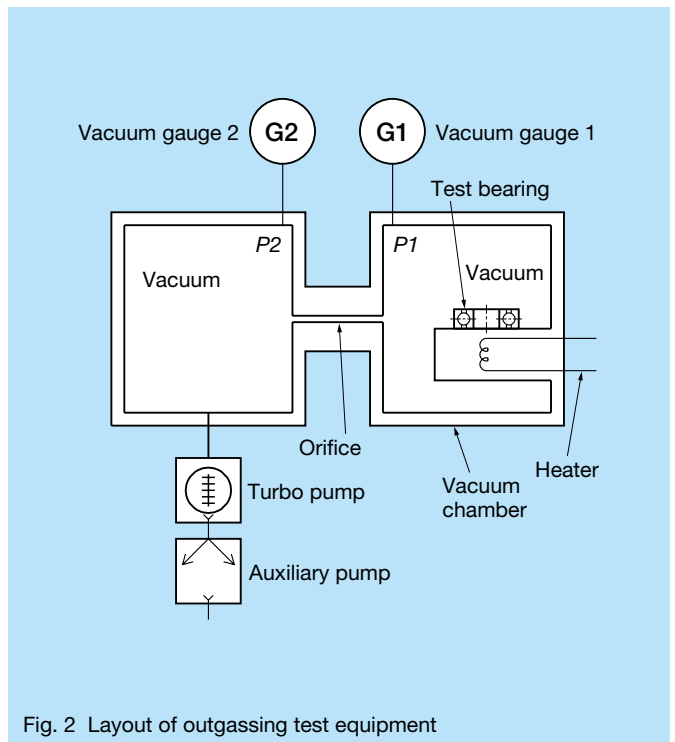
Fig. 2 Layout of outgassing test equipment
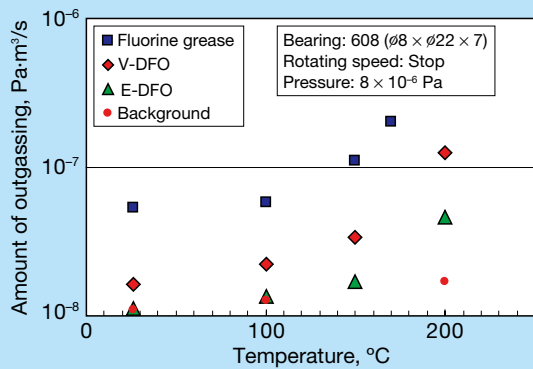
Fig. 3 Outgassing test results
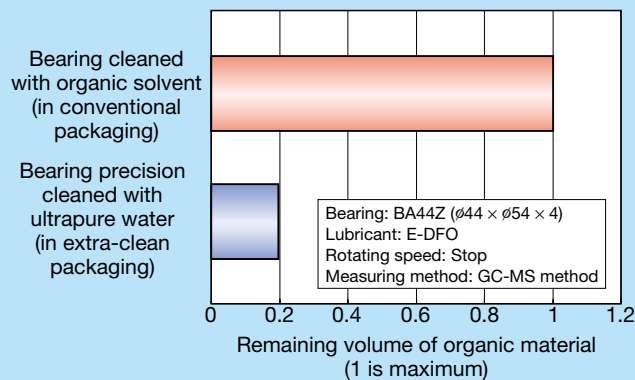
Fig. 4 Measurement results of bearing cleanliness

some outgassing. To address this issue, NSK developed a precision cleaning system that uses ultrapure water and extra-clean packaging to ensure bearing cleanliness and to reduce the amount of any remaining organic material that might exist on the surface of the E-DFO and V-DFO treated bearings.

Subsequently, the remaining volume of organic material on the bearing was measured using the GC-MS method in order to confirm the effectiveness of the precision cleaning system. Test bearings consisted of thin-section, angular contact, BA44Z ball bearings (44 mm × 54 mm × 4 mm).

Fig. 4 shows the measurement results of organic material remaining on the bearing. The amount of organic material remaining on the bearings that underwent the newly developed precision cleaning process and used extra-clean packaging was reduced by 4/5 that of the amount remaining on the bearings that underwent conventional organic solvent cleaning and used conventional packaging.

3.2 Particle emissions

In addition to outgassing rates, particle emissions, which refers to the number of particles of lubricant emitting from the bearing during a specified period of rotation or oscillation, are a primary concern of robot bearings for vacuum environments.

We measured the particle emissions while oscillating the inner rings of E-DFO and V-DFO treated bearings and a bearing packed with fluorine grease. A layout of the test equipment used is illustrated in Fig. 5. The test bearing consisted of a thin-section, four-point contact, NBX20307 ball bearing (203 mm × 219 mm × 8 mm).

Fig. 6 shows the particle-emission test results. The amount of particle emissions from the E-DFO treated bearing was higher than that from the bearing packed with fluorine grease at the beginning of testing. Later, however, particle emissions lowered to levels on a par with the fluorine grease-packed bearing. Particle emissions from the V-DFO treated bearing remained consistent throughout testing at a level that was only slightly higher than the emissions of the bearing packed with fluorine grease.
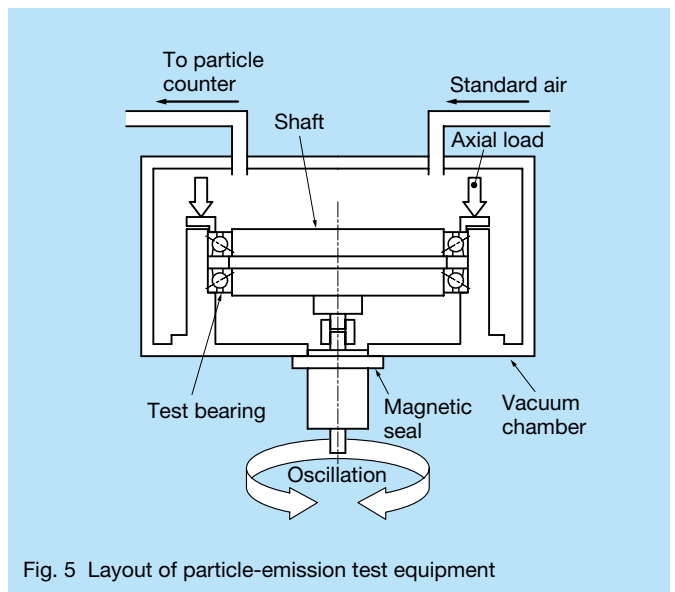
Fig. 5 Layout of particle-emission test equipment
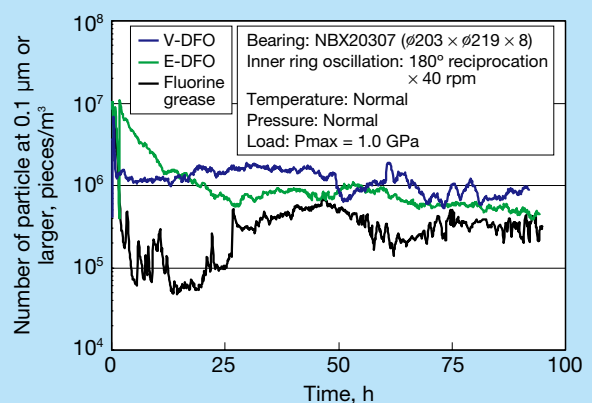
Fig. 6 Particle-emission test results

3.3 Durability

3.3.1 Durability of E-DFO and V-DFO treated bearings

Bearings are sometimes lubricated with fluorine oil instead of being packed with fluorine grease as a measure against outgassing. The use of fluorine-based oil, however, poses a risk to bearing durability. This is especially true for the bearing closest to material that is undergoing the heat treatment process.

Here, we investigated the durability of an E-DFO treated bearing and a V-DFO treated bearing at high temperatures using the test equipment shown in Fig. 7 and compared the results with test bearings using fluorine oil. Testing consisted of outer ring oscillations. Bearing life was defined as the amount of time it took for bearing torque to reach twice the amount of initial rotational torque. The test bearing consisted of a thin-section, angular contact, BA44Z ball bearings (44 mm × 54 mm × 4 mm).

Fig. 8 shows the test results.

The E-DFO treated bearing had the longest life under testing that exceeded 2×10^7 cycles at 100 ºC, with a degree of durability that was 10 times higher than that of the bearing lubricated with fluorine oil. Although the V-DFO treated bearing had a shorter life than the E-DFO treated bearing, it still had a service life that was approximately twofold longer than that of the bearing lubricated with fluorine oil.

The E-DFO treated bearing showed a dramatically higher degree of durability in comparison with the bearing lubricated with fluorine oil. The E-DFO bearing also had the added benefit of being compatible with high temperature conditions of up to100 ºC. Durability of the V-DFO treated bearing was also better than that of the bearing lubricated with fluorine oil, although not on a par with the E-DFO treated bearing under high-temperature conditions. Thus, care should be taken if V-DFO treated bearings might be subjected to high temperatures.
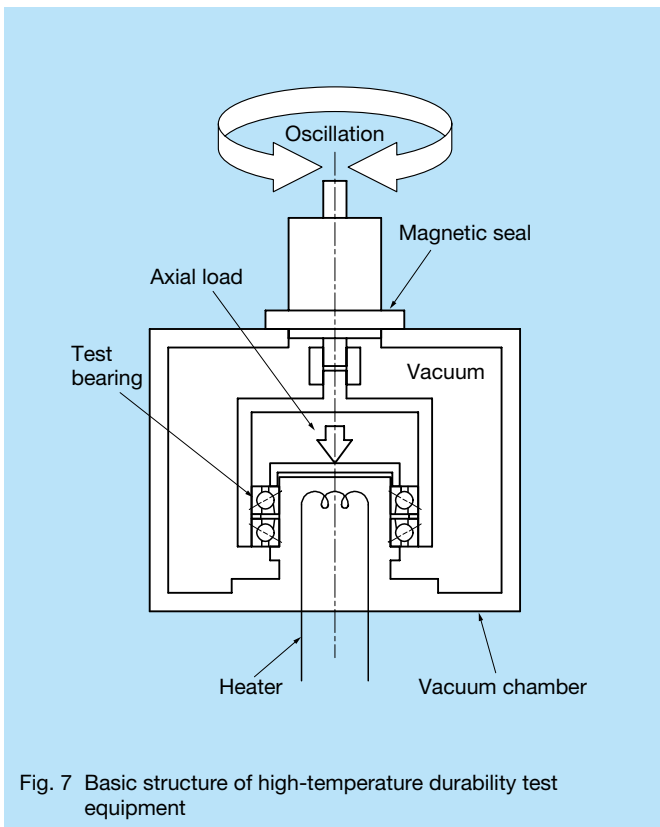
Fig. 7 Basic structure of high-temperature durability test equipment

Fig. 8 Durability test results

Bearing: BA44Z (ø44 × ø54 × 4)
Outer ring oscillation: 90º reciprocation
Pressure: 1×10^{-4} Pa
Load: Fa = 89 N, Pmax = 1.1 GPa

E-DFO
V-DFO
Fluorine oil coating (↑ Test suspended)

Fig. 9 Basic structure of durability test equipment
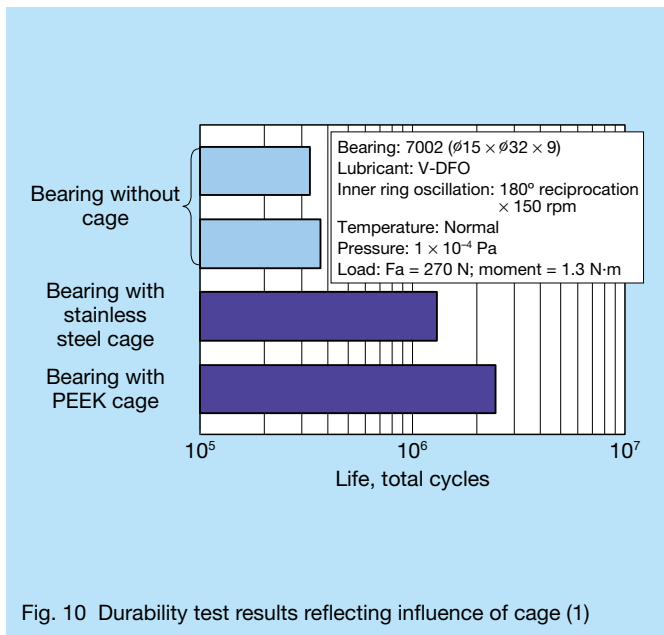
Fig. 10 Durability test results reflecting influence of cage (1)

Bearing: 7002 (∅15 × ∅32 × 9)
Lubricant: V-DFO
Inner ring oscillation: 180° reciprocation × 150 rpm
Temperature: Normal
Pressure: 1×10^{-4} Pa
Load: Fa = 270 N; moment = 1.3 N·m

Bearing without cage
Bearing with stainless steel cage
Bearing with PEEK cage

Life, total cycles

Fig. 12 Durability test results

Bearing: 7002 (∅15 × ∅32 × 9)
Lubricant: V-DFO
Rotating conditions:
    Outer ring oscillation: 180° reciprocating × 150 rpm
    Outer ring rotation: 150 rpm
Load: Pmax = 1.7 GPa (Moment loading)
Temperature: Normal
Pressure: 1×10^{-4} Pa

Oscillation
Rotation in one direction

Life, total cycles
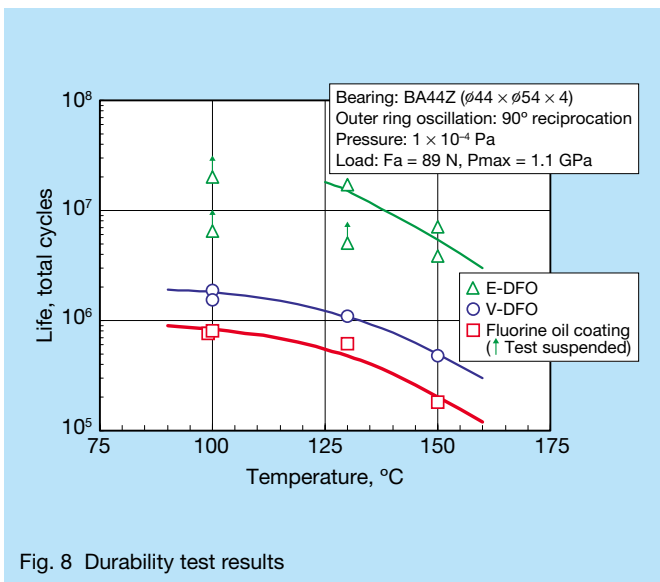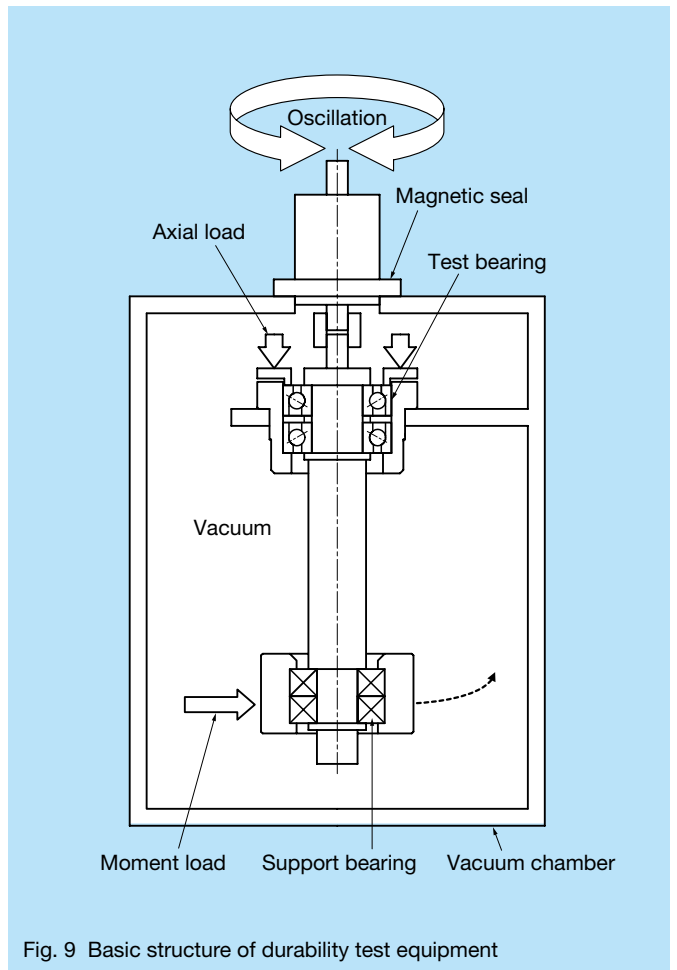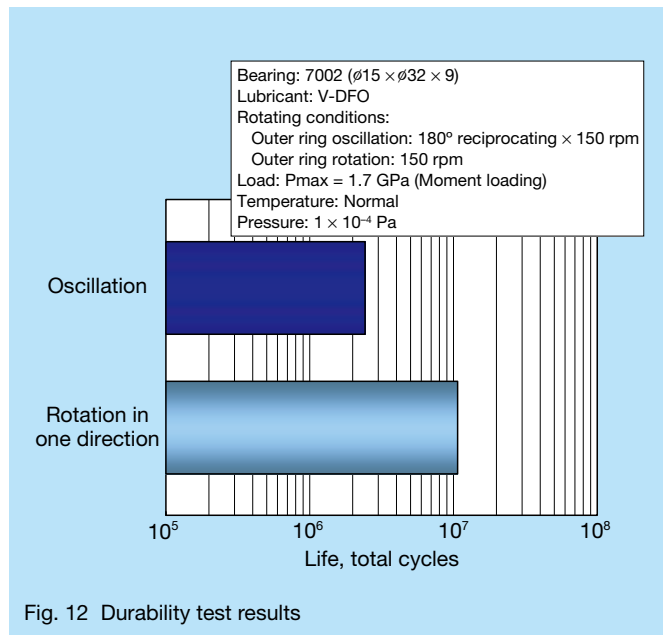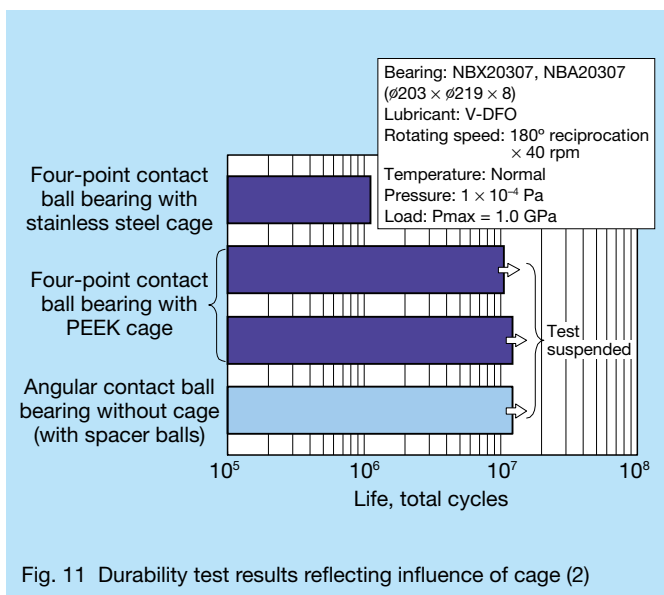

Fig. 11 Durability test results reflecting influence of cage (2)

Bearing: NBX20307, NBA20307 (∅203 × ∅219 × 8)
Lubricant: V-DFO
Rotating speed: 180° reciprocation × 40 rpm
Temperature: Normal
Pressure: 1×10^{-4} Pa
Load: Pmax = 1.0 GPa

Four-point contact ball bearing with stainless steel cage
Four-point contact ball bearing with PEEK cage
Angular contact ball bearing without cage (with spacer balls)

Test suspended

Life, total cycles

The shorter life under higher temperatures is a result of higher vapor pressure of the lubricant base oil under higher operating temperatures.

3.3.2 Improved cage for longer life

Cage specifications in a robot bearing for vacuum environments play a large role in bearing durability. NSK has taken steps to extend bearing life by improving the cage so that durability of E-DFO and V-DFO treated bearings is on a par with that of a bearing packed with fluorine grease. The E-DFO and V-DFO treated bearings use a newly developed polyetheretherketone (PEEK) resin cage instead of a conventional stainless steel cage.

The test results given in Fig. 9 confirm that the PEEK resin cage helps to enhance durability of the V-DFO treated bearing. Test conditions consisted of inner ring

oscillations that were accelerated under a heavy load. Life in this test was defined as the point at which bearing torque was twice the initial rotational torque. The test bearings consisted of angular contact, 7002 ball bearings (15 mm × 32 mm × 9 mm). Also, thin-section, four-point contact, NBX20307 ball bearings (203 mm × 219 mm × 8 mm) were also tested. Both types of cages (conventional stainless steel and PEEK resin) were tested. Additionally, we tested angular contact 7002 ball bearings and thin-section, angular contact, NBA20307 ball bearings (203 mm × 219 mm × 8 mm) using spacer balls instead of cages.

Fig. 10 shows the test results of the 7002 bearing, and Fig. 11 shows the test results of the NBX20307 and NBA20307 bearings.

The 7002 bearing with a PEEK resin cage was tested for 2.5×10^6 cycles and had approximately twice the life than that of the bearing with a stainless steel cage. Also, the NBX20307 bearing with a PEEK resin cage was tested for over 1×10^7 cycles and had a longer life than the bearing with a stainless steel cage that was tested for 1×10^6 cycles.

Because a stainless steel cage does not deform as easily as a resin cage, partial sliding can easily occur between the cage and inner and outer rings or balls. Therefore, wear can occur easily in the case of stainless steel cages if used in E-DFO and V-DFO treated bearings. Conversely, a PEEK resin cage is less susceptible to wear and provides longer life due to the generous lubricating properties of the cage itself and the flexibility of the cage, which serves to mitigate partial sliding. If a stainless steel cage is used in a bearing packed with fluorine grease, life is much more fully extended because a lubricating oil film easily forms and cage wear is negligible even if partial sliding occurs.

The thin-section, angular contact, E-DFO and V-DFO treated NBA20307 ball bearings maintained sufficient durability and life after testing for 1×10^7 cycles using normal spacer balls (Fig. 11).

3.3.3 Oscillation testing and rotation testing

Robot bearings for vacuum environments are often subjected to oscillations. Generally speaking, bearings that are subjected to oscillations are believed to have a much shorter life than if they are subjected to only rotational motion in one direction. There are, however, few concrete examples that confirm this phenomenon.

Therefore, we conducted durability tests on V-DFO treated bearing using the test equipment shown in Fig. 9 and compared bearing lives after subjecting them to outer ring oscillations and rotational motion in one direction. Bearing life was defined as the point at which bearing torque reached twice the initial rotational torque. The test bearings consisted of angular contact, 7002 ball bearings

(15 mm × 32 mm × 9 mm).
Fig. 12 shows the test results.

While testing was possible in excess of over 1×10^7 rotations in one direction, bearing life under 2.6×10^6 cycles of oscillation was approximately 75 % shorter. The reason for shorter bearing life under oscillations is the constantly changing direction of rotation, which causes the balls to slide more easily.

4. Conclusion

E-DFO and V-DFO treated bearings developed for robots operating in a vacuum environment adopt a DFO thin-film lubricant, undergo precision cleaning with ultrapure water, and are shipped in extra-clean packaging. The E-DFO and V-DFO treated bearings dramatically reduce the amount of outgassing and are fully capable of meeting the requirements of low outgassing for vacuum environments. Compared with bearings lubricated with fluorine oil as the conventional low outgassing specification, E-DFO and V-DFO treated bearings are superior in low-outgassing and long-life performance.

The E-DFO treated bearings offer high performance even under high-temperature conditions. We are convinced that these bearings can sufficiently respond to the needs of applications even if future robots subject the bearings to higher temperatures in a vacuum environment.

References
1) M. Kikuchi, "All of Semiconductors" (1998) 108–111, Nippon Jitsugyo Publishing Co., Ltd.
2) M. Hosoya, "Development Trends of Bearings for Special Environments (Vacuum)" Selection Guide for Major Machine Elements, Machine Design April Separate Volume (2005) 18–19.
3) T. Saito, "Vacuum Clean Lubricant Film V-DFO" NSK Technical Journal, No. 673 (2002) 22–25.
4) D. Kinno, "Latest Developments in Thin-Film Lubrication Technology for Vacuum and Clean Environments" NSK Technical Journal, No. 680 (2006) 24–28.
5) T. Terasawa, "Vacuum Handbook Revision III" (1982) 36–41, ULVAC, Inc. 1982 Edition of Vacuum Handbook Editorial Committee.

Masachi Hosoya

Tadahiko Sakamoto

Hiroyuki Ito

Development of the NSK RA Series of Roller Guides

Toshio Yoshida
NSK Precision Co., Ltd.

ABSTRACT

Machine tool performance has improved with each passing year while achieving increasingly higher processing speeds. Recently, longer life and higher accuracy are required for such high-performance machine tools. Additionally, these machine tools have become more complex and compact in design. Accordingly, linear guides widely used for machine tools need to meet new requirements in response to higher-performance standards. NSK has thus developed the NSK RA series of roller guides in which rollers are used instead of balls for the rolling elements. The main features and advantages of the RA series of roller guides are described in this article.

1. Introduction

Machine tool performance has improved in diverse ways to meet the needs of the times. In the wake of recent trends towards higher speeds, there is an increasing shift towards longer life, higher accuracy, and configurations that perform multiple processes with a single machine, in addition to a greater compact size for using space more effectively.

Meeting these market needs requires that linear guides, which are widely used in machine tools, offer higher levels of performance. Therefore, we adopted rollers in the place of conventional balls for the rolling elements of the linear guide. NSK developed the RA series of roller guides (Photo 1) with many features that help boost machine

Photo 1 RA series of roller guide

tool performance by combining the technologies obtained through advances in roller bearings and linear guides. The RA series has significantly improved load capacity, thus giving it a longer rated fatigue life compared to ball guides. In addition, this series provides the high rigidity necessary for higher accuracy and a more compact size.

This report summarizes the characteristics of the RA series and a few of the related test results.

2. RA series features

2.1 Super-high load capacity

International standard ISO 14728-1:2004 defines the basic dynamic load rating for linear motion rolling bearings. The basic dynamic load rating (C_{100}) of the roller guide is calculated by the following equation.

$$C_{100} = b_{\mathrm{m}} \times f_{\mathrm{c}} \times l_{\mathrm{t}}^{\frac{1}{36}} \times i^{\frac{7}{9}} \times Z_{\mathrm{t}}^{\frac{3}{4}} \times L_{\mathrm{we}}^{\frac{7}{9}} \times$$
$$D_{\mathrm{we}}^{\frac{35}{27}} \times \cos\alpha \quad \cdots\cdots\cdots\cdots\cdots\cdots\cdots\cdots\cdots\cdots\cdots\cdots (1)$$

where,
b_{m} = 1.1
f_{c} = $\lambda \times 195$
λ = 0.83
l_{t} : Effective slide length
i : Number of raceways
Z_{t} : Number of effective rolling elements
L_{we} : Effective roller length
D_{we} : Roller diameter
α : Contact angle

It is important to use rollers with the largest possible diameter and length as rolling elements to increase load capacity.

Generally speaking, rollers tend to induce excessive contact pressure at their ends (edge loading), which can reduce the operating life of the roller guides. Although a beveled portion on the cylinder part of the roller (crowning) effectively prevents edge loading, excessive crowning reduces the contact area and can impair actual

Fig. 1　Contact pressure distribution between raceways and rollers of varying crowning profiles[1)]

load capacity and rigidity. NSK designed a crowning configuration that obtains an almost even surface pressure distribution over the entire effective length (Fig. 1).

We also minimized roller chamfers that have conventionally been used to support the rollers and, therefore, achieved the longest possible effective length (Photo 2).

The actions taken are described below.

Conventional roller guides needed large chamfers on the rollers, as the rollers were supported at the chamfers by a retainer. As a result, effective length of rollers was relatively short. In the RA series, as two arms and a body of the retaining pieces support the rollers (Photo 3), there is no longer a need to support the chamfers on the rollers. Thus, the effective length of the rollers of the RA series is longer than that of conventional roller guides.

Here is a comparison between RA series and conventional products based on basic load rating as defined by the ISO. The basic load rating of the RA series

is at the highest level, which was achieved using the design described above (Fig. 2).

In addition, rated fatigue life (L) is calculated by the following equation.

$$L = 100 \times \left(\frac{C_{100}}{f_{\mathrm{w}} \times F} \right)^{\frac{10}{3}} \quad [\mathrm{km}] \cdots\cdots\cdots\cdots\cdots\cdots\cdots\cdots\cdots\cdots\cdots\cdots (2)$$

where,
f_{w}: Load factor
F: Load

A roller guide that is one size smaller than a conventional ball guide exhibits the same or longer life. Therefore, replacing a conventional ball guide with a smaller-size roller guide enables the design of more compact applications (Fig. 3).
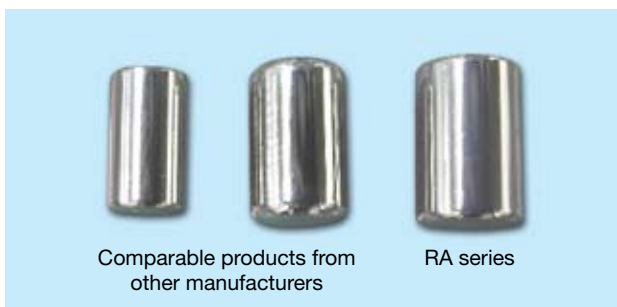
Photo 2　Comparison of an RA series roller with two other types (model size #45)

Photo 3　Rollers and retaining pieces
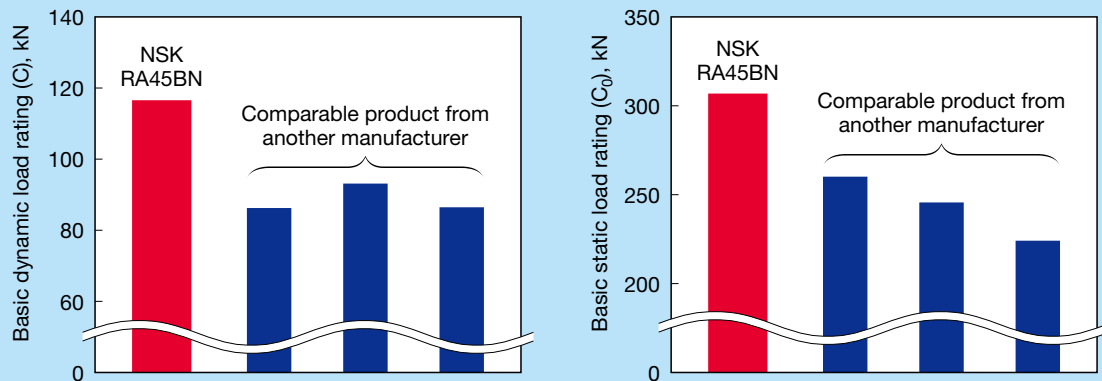
Fig. 2 Comparison of basic load ratings (model size #45)

2.2 Super-high rigidity

Rigidity of the contact area of a roller guide is much higher than that of a linear guide with balls since the roller contact area is a line. Therefore, when reviewing the rigidity of the entire roller guide, material deformation of slide and rail while load is applied to the roller guides must be taken into consideration as well as the roller contact area[1]. As a result, it is important to enhance the rigidity of the slide and rail materials. A circulation pathway for the rolling elements must be formed in a limited amount of space, as described above, and rigidity of the RA series is obtained as a result of an optimized design based on a material deformation analysis using an FEM model (Fig. 4).

Fig. 5 shows the comparison results of the relationship between external load and deformation by measurements and calculations[1]. Calculations were conducted for a case in which the materials of the slider and rail unit were assumed to be rigid, and for a second case in which rigidity of the materials was incorporated. Deformation is considerably less than the experimental results, and rigidity is overvalued in the first case. On the contrary, change in accordance with load correlates well in the second case.

Here, results between a conventional roller guide and the RA series are compared. Material deformation of the slide is presumed, and the raceway surfaces of the RA series are machined in accordance with these assumptions. Optimum contact is maintained for the roller and high rigidity is also maintained even in the heavy load
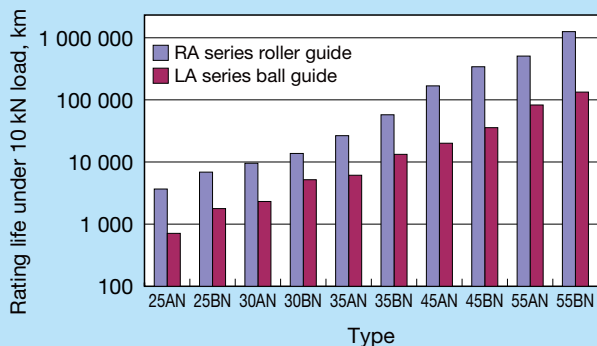
Fig. 3 Comparison of rating life for the RA series roller guide and the LA series ball guide
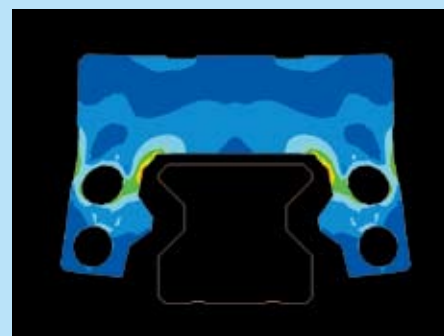
Fig. 4 An example of roller slide deformation analysis results
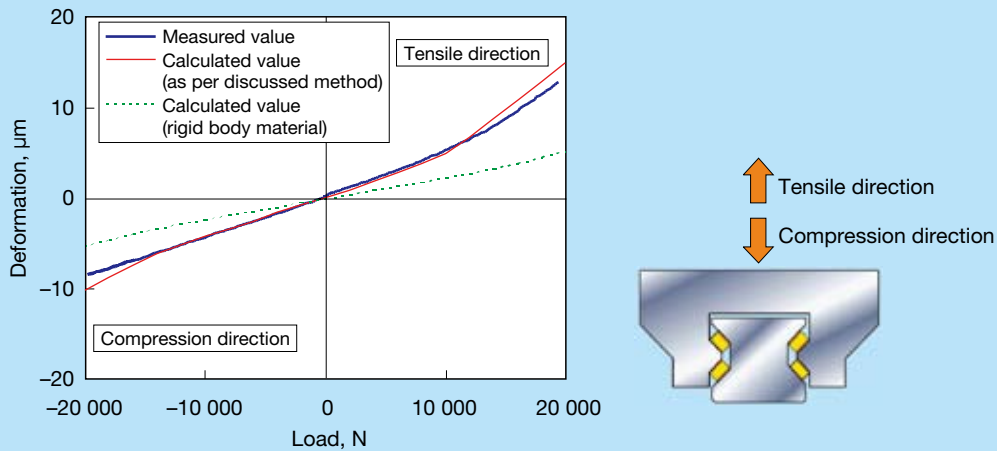
Fig. 5 Relation between load and deformation for measured and calculated results (model size #35)[1)]
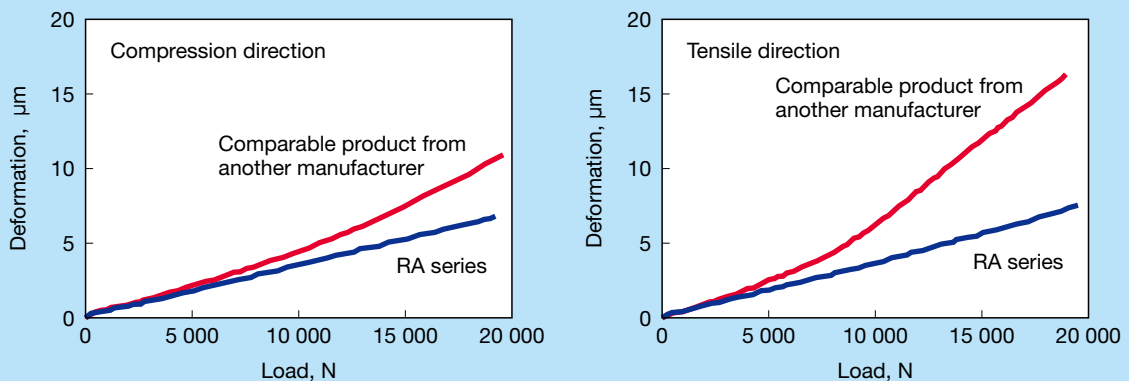
Fig. 6 Comparison of measured rigidity (model size #45)
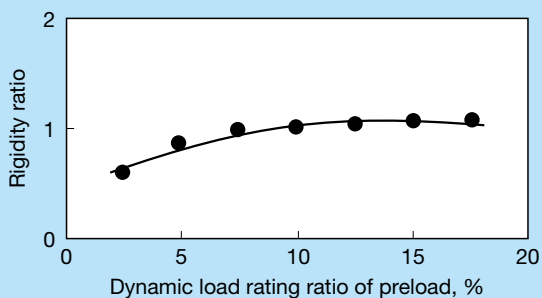
Rigidity ratio is 1 when preload is 10 % of dynamic load rating.

Fig. 7 Relation between preload and rigidity (model size #35)

range. Conversely, deformation of the conventional product dramatically increases due to preload loss in the same range (Fig. 6).

Furthermore, changes in rigidity occur slowly since the material structure of the slider and rail absorbs the change in preload in the roller guide, where contact rigidity dominates material rigidity (Fig. 7). Therefore, classification of preload does not have to be as clear as when using linear guides with balls as rolling elements.

2.3 Super-high motion accuracy

Roller guides used for guiding must possess a high level of motion accuracy since the motion accuracy of machine tools directly affects machining accuracy and quality.

Rolling element passage vibration is a typical factor that influences roller guide motion accuracy. This vibration
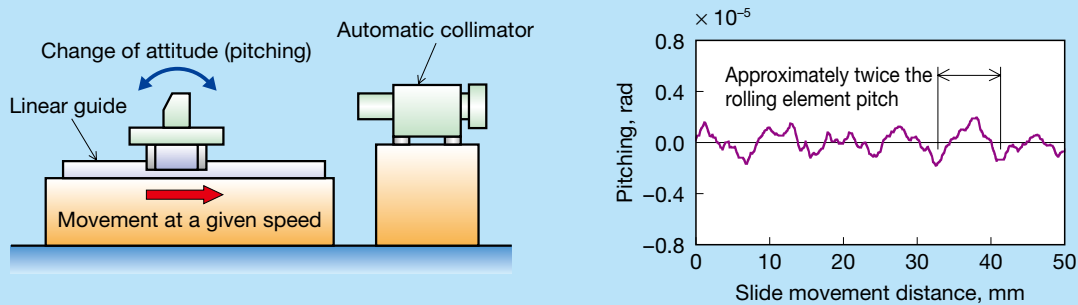
Fig. 8 Measured result of roller motion accuracy for rolling element passage vibration in a conventional roller guide (model size #35)
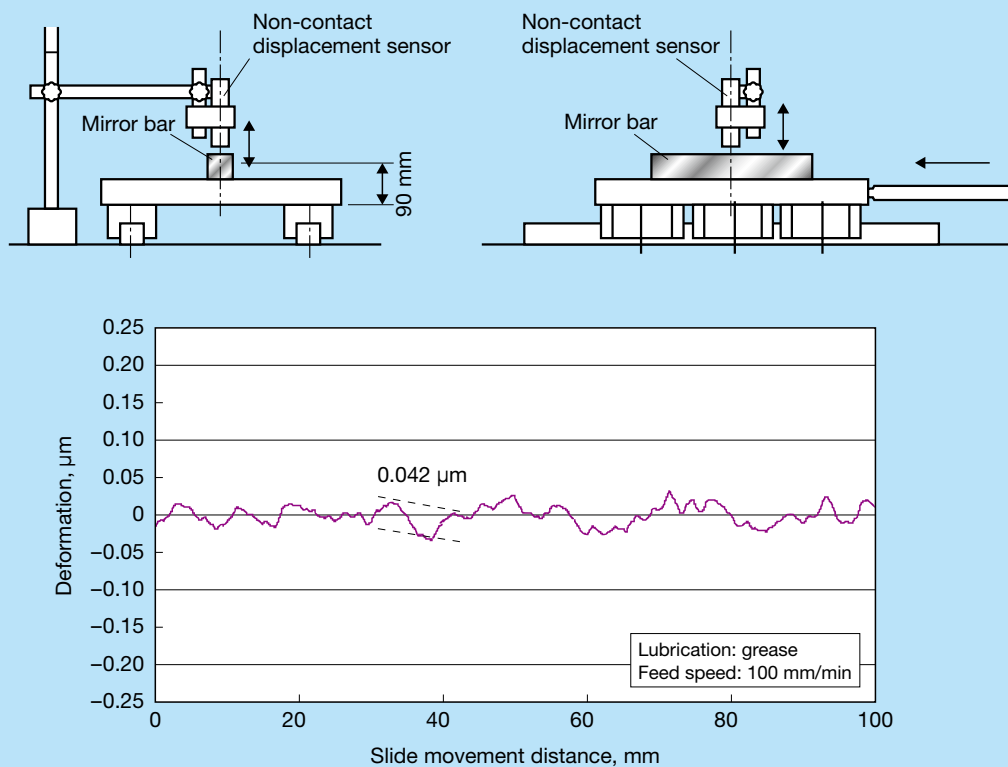
Fig. 9 Measured result of roller motion accuracy for rolling element passage vibration in a special specification of the RA series for highly precise motion (model size #25)

results from a cyclic change of attitude that occurs during slide motion. Rolling element passage vibration occurs due to cyclic variation of the number of rolling elements under load when there is a relative displacement between the rail and the slide. The cycle of passage vibration is approximately twice the pitch of the rolling elements since they orbit at half the speed of the slide (Fig. 8). Although this vibration is actually at the sub-micron order, it can lead surface quality deterioration due to surface undulation caused by tool paths. In addition, the vibration can be amplified when a cutting point is far from the roller guide.

NSK has already addressed the mechanism of this rolling element passage vibration and has established a quantitative analysis method[1]. Rolling element passage vibration can be calculated by inputting internal load
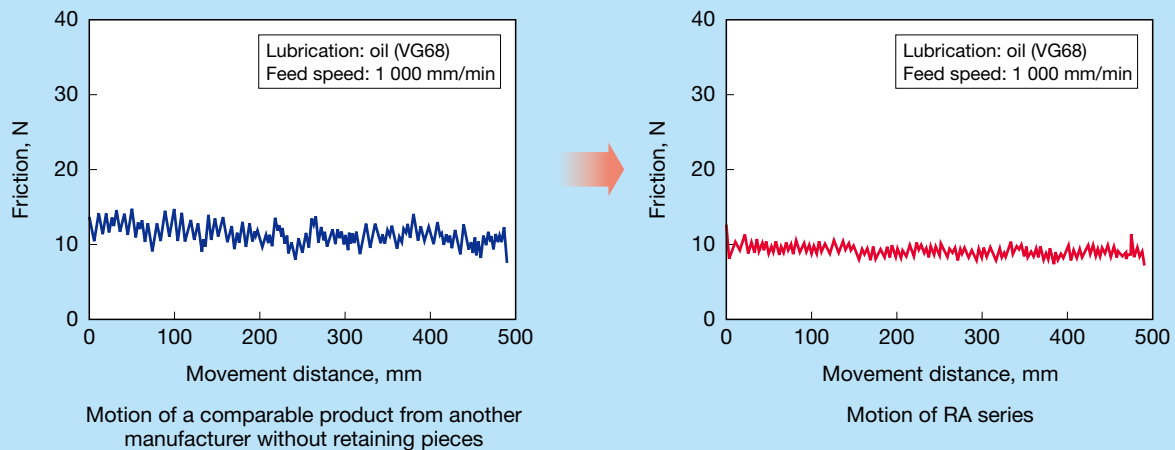
Fig. 10 Measured results of dynamic friction force fluctuations (model size #35)

conditions and external load conditions acting on the roller guide to solve the motion equation for each slide and each rolling element of the table body. Moreover, crowning at each end of the raceway of the slide can help restrict rapid load changes from the rolling elements moving in and out. Conventionally, however, it was necessary to verify machining, which depends on a geometric evaluation and experience to discover an optimal shape. This analysis makes it easier to examine the effects of crowning, allowing for a more easily conducted study.

Based on this analysis, the RA series offers roller guides with less passage vibration and higher motion accuracy, even with the standard specifications, to contribute to higher machining accuracy as a result of a design that minimizes rolling element passage vibration.

Using the analytical calculation method, we also developed specialized specifications of the crowning shape

and others in order to specifically reduce rolling element passage vibration. We then produced products using these specifications. With the additional effect of reduced load variation due to preload, rolling element passage vibration of this product has been reduced to a level of 50 nm (Fig. 9).

2.4 Smooth motion

NSK has already commercially developed the NSK S1™ series[2], which achieves smooth circulation by eliminating the interference between steel balls by inserting a resin retaining piece between the steel balls used in ball screws and linear guides; this advance has been well-received by the market.

We newly designed retaining pieces for the rollers to further the development of roller guides and installed them in the RA series as a standard feature. The retaining pieces installed between the rollers eliminate interference between the rollers and maintain their attitude for controlling skew (incline), which is peculiar to rollers. As a result, smooth motion (a guide with less dynamic friction variation) was achieved (Fig. 10). An improvement in sound quality was also confirmed (Fig. 11). (Refer to 2.1 for roller support.)

2.5 Low friction

Increasing preload to enhance ball guide rigidity leads to greater contact pressure and a larger contact oval, and induces a differential slip due to the difference in the rotation radius between the ends and the center of the oval (Fig. 12), thus increasing dynamic friction. There is a correlation between preload / rigidity and friction—the higher the rigidity, the greater the dynamic friction.

Conversely, although the roller guide exhibits high rigidity, the difference between roller rotation radiuses is very small, thus differential slip is very small. This tendency does not change even when preload increases,
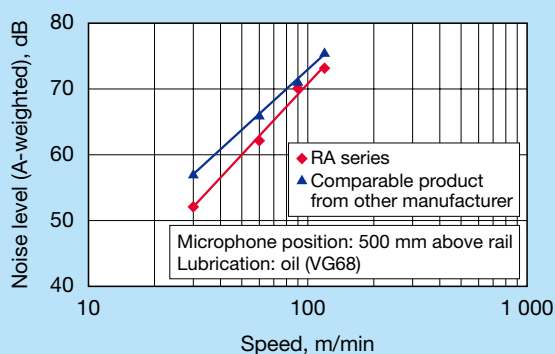
Fig. 11 Comparison of noise test results (model size #45)
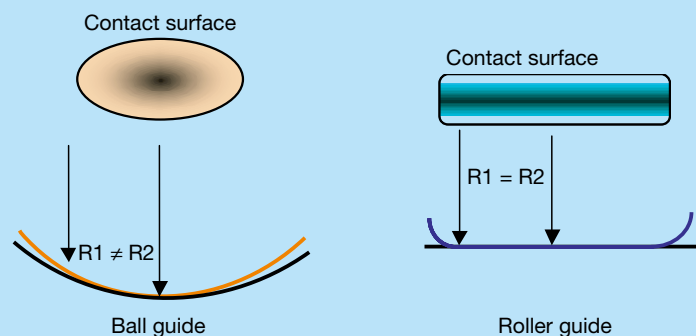
Fig. 12 Contact surface configurations

nor does dynamic friction rise significantly. When we measured the dynamic friction under loaded conditions, the dynamic friction coefficient μ, which included friction in areas other than the contact area, was approximately 0.0004 (Fig. 13). This is less than half the comparable values for conventional guides using balls.

Therefore, the roller guides can achieve high rigidity while maintaining low friction.

2.6 Highly dust-proof resistant

In general, bellows and telescopic covers shield machine-driving mechanisms and protect them against debris, which is the same for linear guides. Nevertheless, there are occasions in which exposure to cutting chips and coolant cannot be avoided. Recently, covers of machine tools have been simplified or eliminated in order to facilitate multifunctional or compact machine tools, or in order to simplify their structure. Also, machine tools sometimes may be required to operate in severe environments where they are subjected to the splattering of coolant when more efficient machining is required.

The RA series roller guide utilizes seals made from coolant-resistant material at both ends of the slide. Table 1 shows the results of submergence testing in coolants that are currently available in the marketplace. Furthermore, inner seals, which were previously optional, are installed as standard (larger than size #25) to protect the inside of the slide along with bottom seals and the end seals described above. Moreover, rail covers are now available (Photo 4) in addition to conventional mounting hole caps. A belt-shaped stainless steel sheet is installed after mounting the rail to the machine base. All rail-mounting holes are sealed, and the rail surface is kept smooth with no accumulation of foreign debris. The rail covers are designed to snap into place on the rail surface since they are to be installed after mounting the rails. The rail
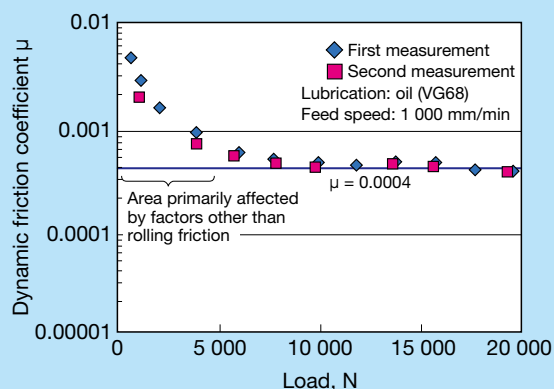
Fig. 13 Coefficient of dynamic friction (model size #35)

Table 1 Results of end seal endurance test in coolant

Tested coolant		Swelling
Emulsion type	Company A	N/A
Synthetic type	Company B	N/A
	Company B	N/A
Synthetic type	Company C	N/A
	Company C	N/A
Emulsion type	Company D	N/A
Synthetic type	Company D	N/A

Temperature: 70 °C
Period: 30 days
Dilution: 20–30 times

Photo 4 Rail cover for severe environments
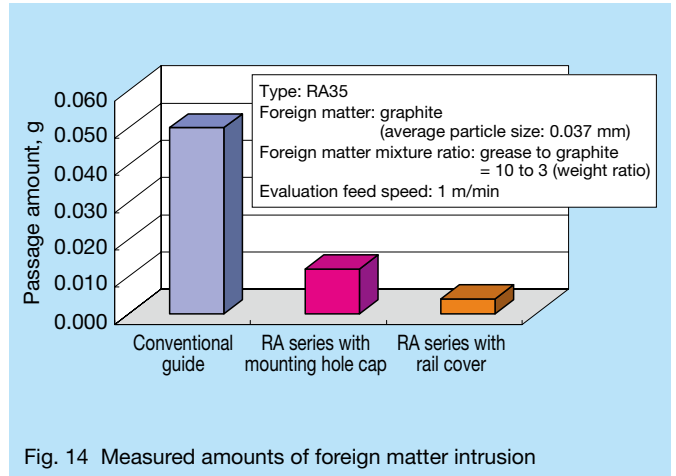
Fig. 14 Measured amounts of foreign matter intrusion

Type: RA35
Foreign matter: graphite
(average particle size: 0.037 mm)
Foreign matter mixture ratio: grease to graphite
= 10 to 3 (weight ratio)
Evaluation feed speed: 1 m/min

Test condition
Stroke: 4 mm
Cycle: 10 million
Oscillation frequency: 15.6 Hz
Maximum speed: 1 000 mm/s
Lubrication: lithium grease
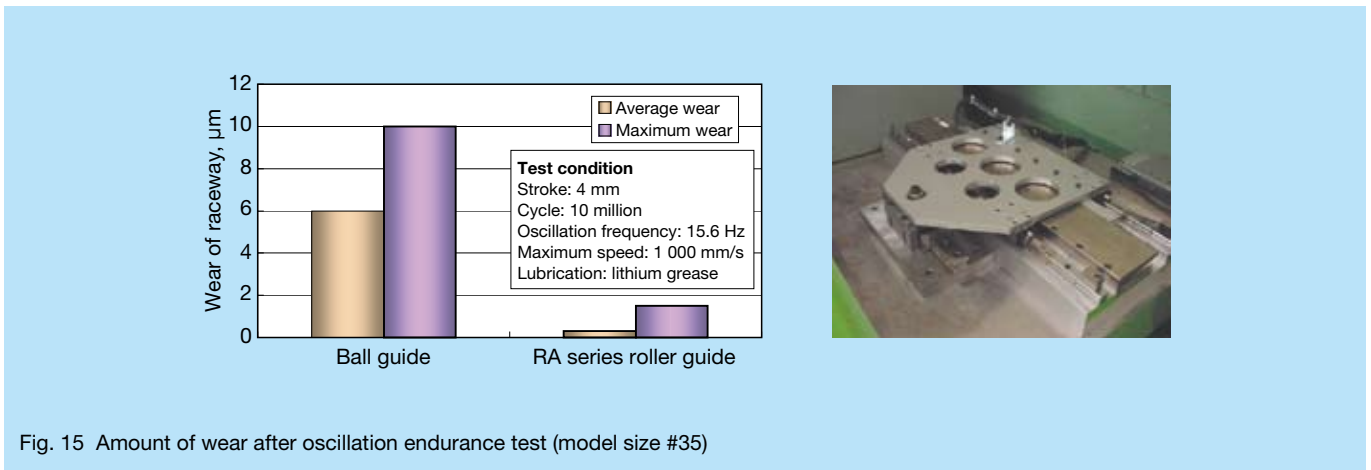
Fig. 15 Amount of wear after oscillation endurance test (model size #35)
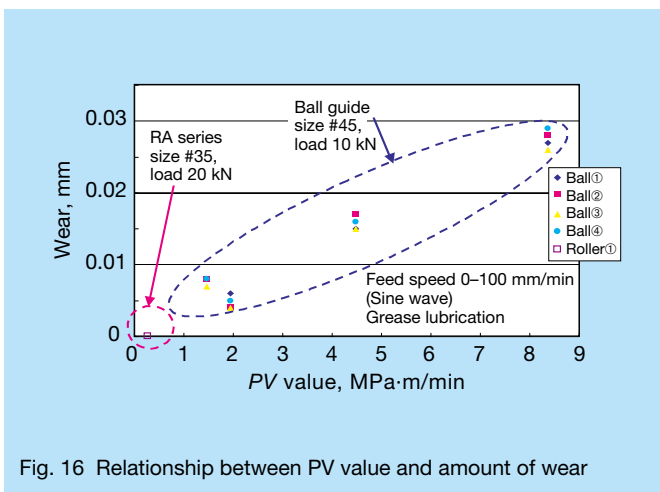
Fig. 16 Relationship between PV value and amount of wear

cover reduces the entry of foreign matter by 9/10 that of a conventional product (Fig. 14). While utilizing mechanisms for protection from debris in severe environments is advised and generally sufficient, the rail covers are considered an effective measure against contamination.

2.7 Wear-resistant performance
2.7.1 Wear-resistant performance during oscillation

Since linear guides move in an oscillating motion when creating detailed shapes in mold machining, fretting wear can be generated as the lubrication film between rolling elements and raceway surface breaks down.

Rollers in the RA series roller guides exhibit very little differential slip compared with ball guides, although there is some variation in rotation radius due to crowning. Fig. 15 shows the results of oscillation testing of the RA series and ball guides. The RA series has significantly less wear than the ball guides, confirming a considerable improvement in wear-resistant performance under oscillating conditions.

2.7.2 Wear-resistant performance at extra-slow speed

The machining of a taper shape requires one axis to move at a very slow feed while other axes are controlled simultaneously. The oil film between rolling elements and raceway surfaces may sometimes be insufficient, and wear may be generated at an early stage during continuous low-speed operation.

In general, wear is correlated with the *PV* value

(P: maximum contact surface pressure; V: maximum slip velocity in a contact oval). Roller guides have a lower slip velocity (differential slip component) and a lower contact surface pressure than ball guides, which limits the amount of wear and facilitates low-speed machining (Fig. 16).

3. Conclusion

The RA series of roller guides is now beginning to contribute to other industries beyond the machine tool market. This series offers an extended choice of sizes, and has earned a solid reputation in many industrial fields affiliated with automobile production, semiconductor and liquid crystal display manufacturing, transportation, and medical devices. We look forward to making further contributions that aim for improving the performance of applications in many more areas in the future.

References

1) J. Matsumoto, "Numerical Analysis Technology & NSK Linear Guides™ for Machine Tools" NSK Technical Journal 676, (2003) 33–41.
2) H. Yamaguchi, T. Okubo, "Development of NSK S1™ Series Ball Screws and Linear Guides" NSK Technical Journal 671, (2001) 35–43.

Toshio Yoshida

Ultrahigh-Speed Planetary Needle Roller Bearings

Needle roller bearings facilitate the smooth rotation of pinion gears in a planetary mechanism, which is a type of change-speed gearbox that is used in automatic transmissions (ATs) for automobiles. These bearings not only rotate about the shaft, but also revolve around the sun gear, as is illustrated in Fig. 1. Due to requirements for improved fuel economy and higher acceleration performance of newer vehicles, typical ATs have evolved from conventional four-speed transmissions to five-speed, six-speed, seven-speed, and even eight-speed transmissions.

With this increase in the number of gear ratios, the maximum rotational and orbital speeds that are required of the planetary needle roller bearings are also increasing.

After carrying out various analyses and tests, NSK was able to develop a planetary needle roller bearing that meets the demands of ultrahigh-speed operating conditions. Specifications and features of this newly developed ultrahigh-speed planetary needle roller bearing (see Photo 1) are presented in this article.

1. Specifications

For the bearing to meet the demands of ultrahigh-speed operating conditions, we made specific improvements to the cage and shaft in order to enhance durability performance.

· The cage geometry was optimized and high-strength chrome molybdenum steel was used for cage material
· A chemical coating process was applied to cage surface areas
· The shaft was subjected to a shot-peening process after the usual process of special induction hardening

2. Features

(1) Increasing fatigue strength of the cage

High-strength chrome molybdenum steel (case-hardened steel) was adopted for the cage material because it allows for a cage design that is lighter, has a thinner cross-section profile, and is stronger than conventionally used carbon steel.

Additionally, the flange geometry of the cage (near the roller end faces) is such that the cage structure is strengthened. Furthermore, an optimum cage geometry combined with an optimized number of rows (resulting in a multi-row design) reduces stress concentrations acting on the cage pockets when the rollers impact the cage bars.
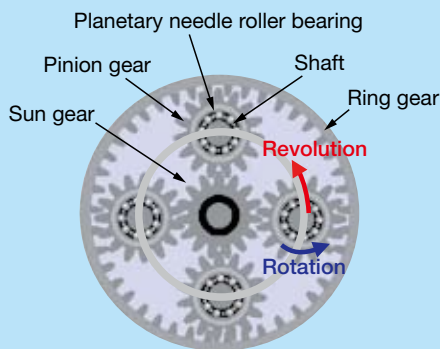
Fig. 1 Planetary gear mechanism

Photo 1 Ultrahigh-speed planetary needle roller bearings
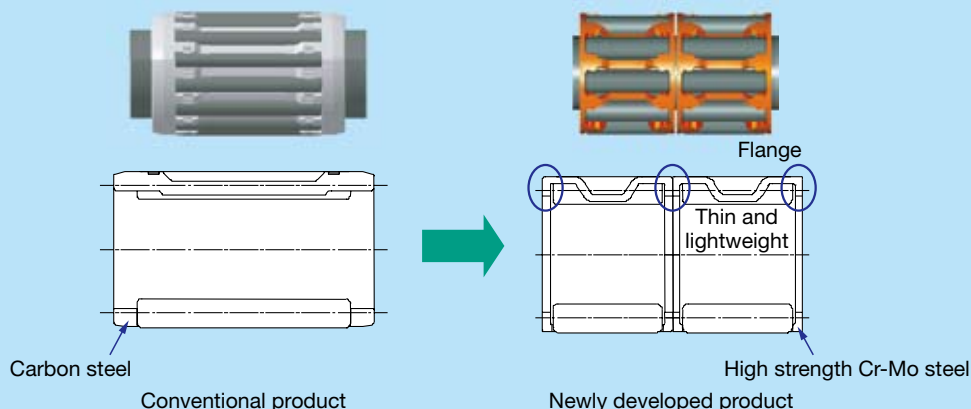
Fig. 2 Cage strength enhanced
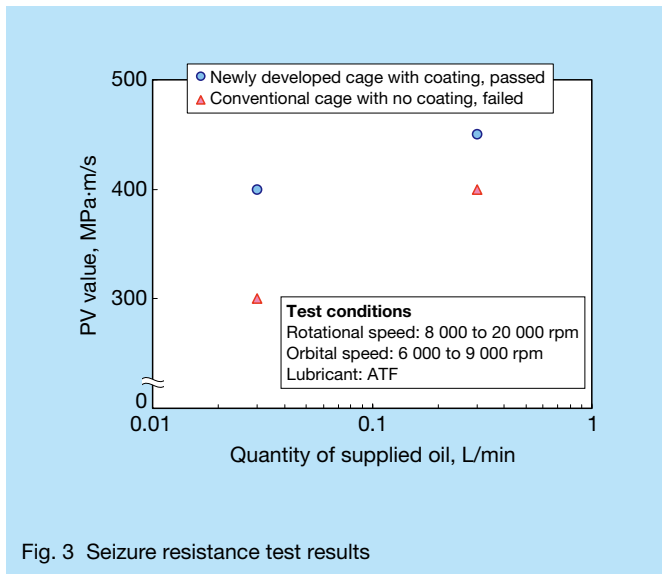
Fig. 3 Seizure resistance test results

Fig. 5 Shot peening of material surface ensures longer rolling fatigue life

Fig. 4 Shaft surface reinforcement technology

Fig. 2 illustrates a comparison of a conventional cage and the newly developed cage.

(2) Improved seizure resistance of cage

Application of a chemical conversion coating on the order of several micrometers thick to the surface areas of the cage ensures a high retention of lubricant on the surface areas, thus mitigating heat that would be generated as the cages (of each row of needle rollers) and the pinion gears rub against each other.

Fig. 3 shows the results of seizure resistance testing that was conducted for the cages.

The chemical conversion coating is also more effective in reducing the PV value when compared with conventional cages. A PV value is the product of surface pressure (P), which builds up between the cage and bore surface of the pinion gear, and sliding speed (V). A higher PV value indicates greater seizure resistance. The end result is a newly developed cage that is better capable of withstanding ultrahigh-speed operating conditions in comparison with a conventional cage.

(3) Longer shaft life

The shaft underwent special induction hardening—a heat treatment process developed by NSK—to enhance service life of the shaft.

Special induction hardening is a process by which material life is enhanced by separating out retained austenite on the surface layer. Additionally, eliminating retained austenite at the core of the material significantly reduces plastic bending (deformation) of the shaft while operating under conditions of high temperatures or heavy loads.

In addition to the special induction hardening, the shaft was subjected to a life-enhancing process called shot peening (see Fig. 4).

Fig. 5 provides a comparison of durability for test pieces made from conventional material and shot-peened material.

A shaft that is subjected to highly compressive residual stress through the process of shot peening has a longer service life than a shaft of conventional specifications.

3. Conclusion

Through the application of technologies that strengthen the cage and help to extend the service life of the shaft, we were able to develop an ultrahigh-speed planetary needle roller bearing that provides the degree of high durability required of applications that are subjected to the harshest of operating conditions, which are found in modern automotive transmissions.

This bearing, which continues to have a positive reputation in the marketplace, has been mass-produced for use in a large number of ATs found in new vehicles.

NSK's ultrahigh-speed planetary needle roller bearing for automotive transmissions plays a significant role in providing higher functionality, promoting more compact designs, increasing capacity, and lowering friction of automotive transmissions. These factors will become ever more critical as ATs continue the trend towards more overdrive ratios in multi-overdrive ATs.

Latest Needle Roller Bearing Assembly Promotes Greater Efficiency in Automotive Transmissions

About ten plain bearings (bushings) are used in an automotive automatic transmission (AT). Bushings used in modern automatic transmissions must ensure against seizure, as they are subjected to increasingly severe operating conditions as a result of the growing number of overdrive gears, higher operating speeds, tighter space requirements, and demand for higher-load capacity. Accordingly, NSK addressed these issues by being the first in the world* to develop a drawn cup needle roller bearing and seal ring assembly (see Photo 1) that is of the same overall thickness as that of a bushing. NSK's newly developed needle roller bearing addresses the various issues faced by the severe operating conditions of AT bushings.

1. Structure and Specifications

Replacing AT bushings with needle roller bearings requires that the following conditions be met:
1. Amount of oil penetration must remain the same as that of a bushing.
2. Overall cross-sectional thickness of the needle roller and seal assembly must remain the same as that of the bushing.

Positioning the seal ring inside the needle roller bearing ensured that the amount of oil penetration remained unaffected (Fig. 1). Adjusting the clearance between the seal ring and the shaft made it possible to ensure a sufficient amount of oil flow into the bearing (Fig. 2). The problem of cross-sectional thickness was resolved by adopting a newly developed seal ring. The unconventionally thin design of the needle roller bearing and seal assembly was made possible with a highly precise and thin seal ring, which was manufactured using a press-forming process.

2. Features

The thin drawn cup needle roller bearing with seal ring has the following features.

Photo 1 World's thinnest*, newly developed drawn cup needle roller bearing with a seal ring
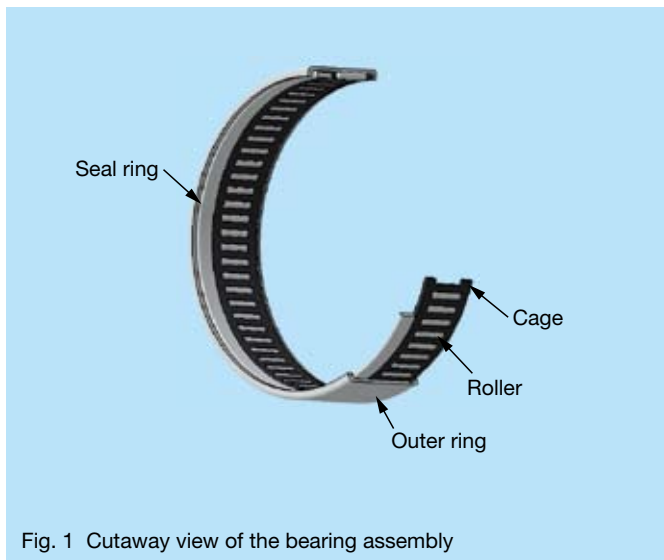
Fig. 1 Cutaway view of the bearing assembly
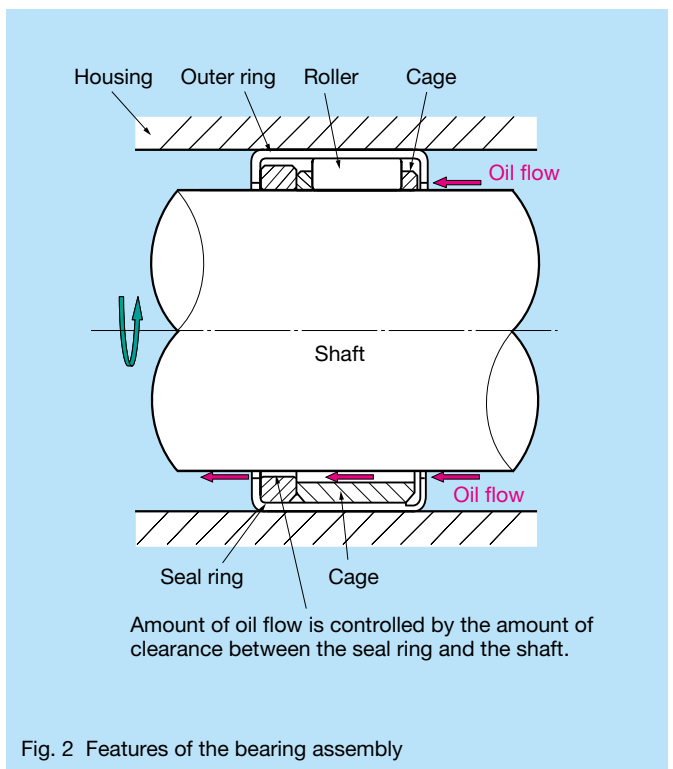
Fig. 2 Features of the bearing assembly

Amount of oil flow is controlled by the amount of clearance between the seal ring and the shaft.

Fig. 3 Comparison of seizure resistance test results
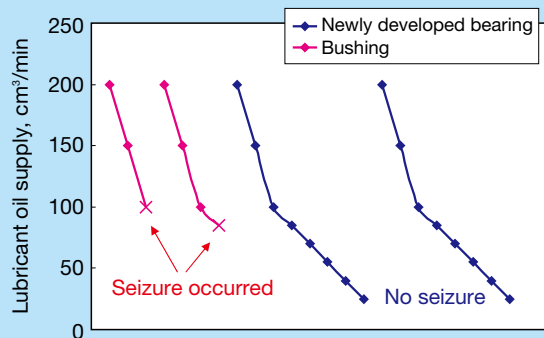
Test conditions
Rotating speed: 6 800 rpm (inner ring rotation)
Load: 1 000 N
Lubricant: ATF (80 °C)

Fig. 5 Comparison amount of oil penetration
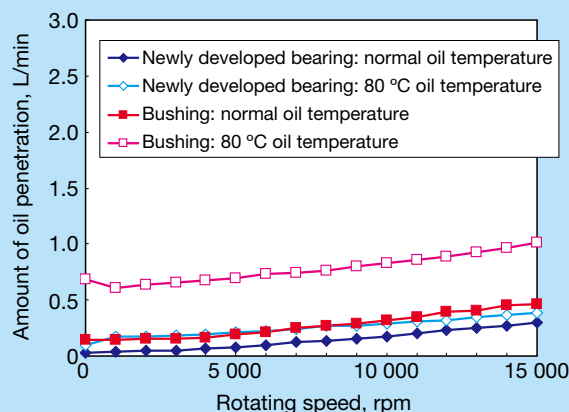
Test conditions
Load: No load
Oil pressure: 50 kPa
Lubricant: ATF

Fig. 4 Comparison of dynamic torque test results
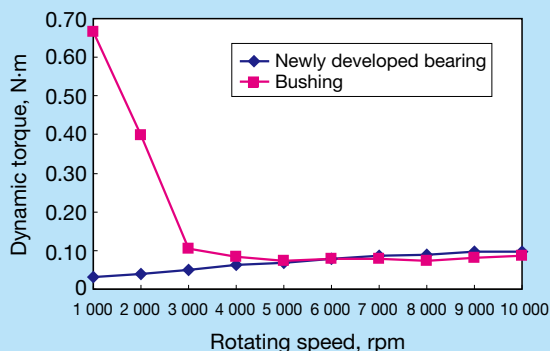
Test conditions
Load: 500 N
Lubricant: ATF (80 °C)

(1) Compactness

This newly developed, highly precise, thin seal ring has a thickness of only 0.85 mm, which facilitated the design of a new needle roller that is approximately 50 % thinner at 1.5 mm in comparison with the sectional thickness of a conventional drawn cup needle roller bearing with seal ring, which can vary from 3 to 3.5 mm thick. The more compact design makes it possible to replace bushings with roller bearings.

(2) Seizure resistance

Even under starved lubrication conditions, the needle roller bearings are able to ensure smooth rotating performance (Fig. 3). Fig. 3 illustrates the amount of oil present when the bushings fail as a result of decreased

supply of lubricant oil.

(3) Reduced torque loss

Torque loss of the newly developed needle roller bearings between the 1 000 to 4 000 min-1 range was reduced by 25 to 95 % in comparison with that of a standard bushing. Thus, energy losses can be further reduced (Fig. 4).

(4) Amount of oil penetration

The amount of oil and how it flows in an AT can be controlled with the newly developed needle roller bearing and seal ring assembly with the same degree of ease as that of a typical AT bushing (Fig. 5).

3. Applications

In addition to ATs for conventional automobiles, this newly developed bearing can be used in transmissions for hybrid vehicles, and in industrial applications that typically used plain bearings.

4. Conclusion

As consumers demand that newer automobiles offer greater fuel economy, NSK anticipates increased need for this newly developed thin drawn cup needle roller bearing with seal ring. We will continue to develop new products that meet the needs of the marketplace while contributing to the enhanced performance of automobiles.

*According to NSK research as of July 21, 2006

Highly Corrosion-Resistant Self-Aligning Ball Bearings

Bearings used in transfer systems, including cleaning equipment that are used in the manufacturing process of flat panel displays (FPDs), require sufficient resistance to highly corrosive chemical exposure. Together with the increasingly larger size of films and panels, FPD manufacturing facilities have become larger in scale, which imposes stronger demand for bearings that can accommodate misalignment of shafts used in the cleaning equipment.

NSK developed three series of self-aligning ball bearings: ES1, which is made of martensitic stainless steel; AQUA-BEARING™, which is made of resin material; and ESA, which is made of austenitic stainless steel. These three series of self-aligning bearings (Photo 1) offer excellent corrosion resistance under operating conditions of high humidity and exposure to highly corrosive agents that include acid and alkali. This article discusses the features, specifications, etc. of these three bearings.

1. Features and Specifications

(1) Corrosion resistance and durability

Fig. 1 illustrates the basic structure and describes the bearing materials used in each series. The ES1 self-aligning ball bearing adopts a highly corrosion-resistant martensitic stainless steel (ES1 steel), which was developed by NSK, for the inner and outer rings. ES1 bearing steel provides superior corrosion resistance compared with conventional stainless steel. We made the cage from austenitic stainless steel and the balls from martensitic stainless steel. ES1 all-stainless-steel bearings are suitable for environments that subject the bearings to high humidity or water.

The AQUA-BEARING™ series of self-aligning ball bearings adopts fiber-reinforced fluororesin material for the inner and outer rings. The ESA series of self-aligning ball bearings adopts surface-hardened austenitic stainless steel for the inner and outer rings. In addition, the

Photo 1 Highly corrosion-resistant self-aligning ball bearings
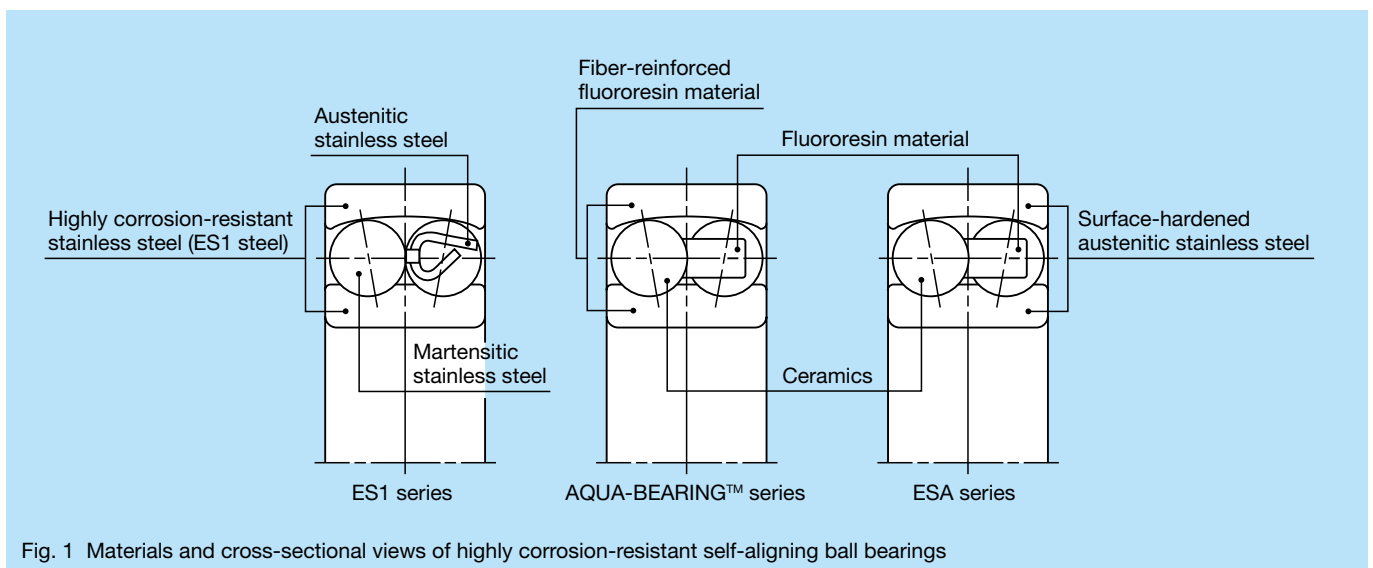
Fig. 1 Materials and cross-sectional views of highly corrosion-resistant self-aligning ball bearings

fluororesin cage offers superior corrosion resistance and self-lubricating properties. The ceramic balls used in this series provide superior corrosion resistance and durability for environments that subject the bearings to acids and alkalis.

Fig. 2 illustrates the range of operating conditions for these three series of highly corrosion-resistant self-aligning ball bearings.

(2) Self-aligning property

The spherical geometry of the outer ring raceway surface of these bearings can easily accommodate shaft misalignment up to 5 º (see Fig. 3). These bearings are best suited for applications in which it is difficult to align the shaft and housing in which the shaft may bend.

2. Dimensions

Table 1 lists the available dimensions.

3. Applications

Highly corrosion-resistant self-aligning ball bearings are suitable for transfer systems, including cleaning equipment, liquid crystal display (LCD) substrate washing equipment, food processing equipment, etc.

Fig. 2 Range of operating conditions of highly corrosion-resistant self-aligning ball bearings
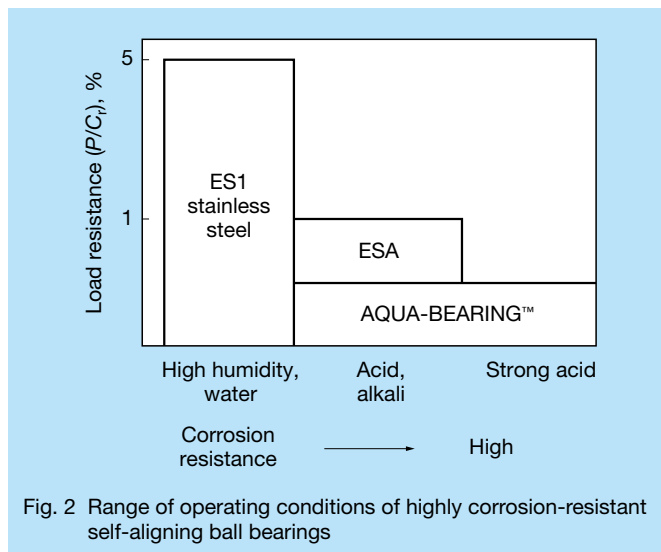
4. Conclusion

The increase in size of film handling, transfer, and cleaning equipment in the future will result in increased use of more corrosive chemicals by the FPD industry. NSK will continue to actively develop bearing products that will meet the future needs of FPD manufacturers.

Fig. 3 Self-aligning function
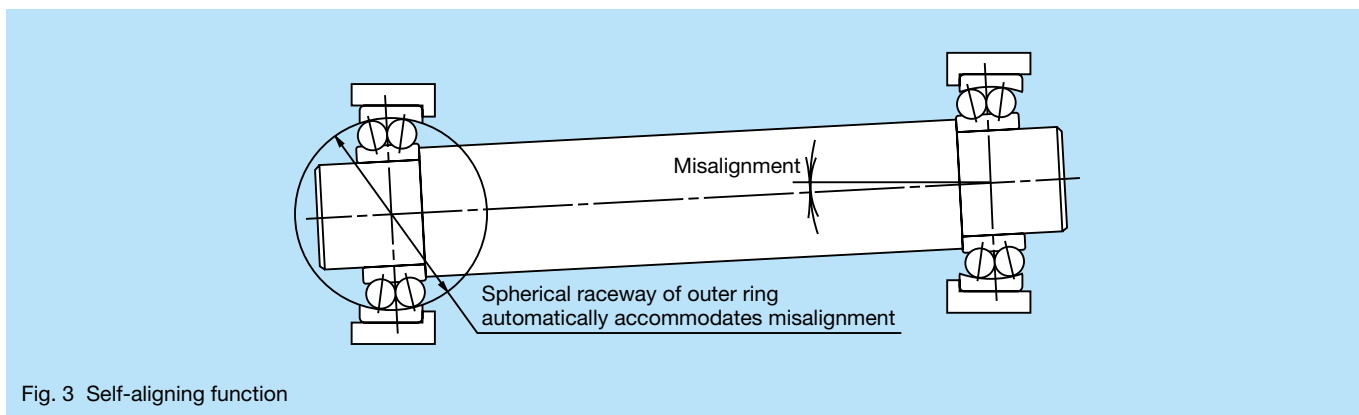
Table 1 Boundary dimensions of highly corrosion-resistant self-aligning ball bearings

Unit: mm

Basic number	Boundary dimensions			Bearing number		
	Bore diameter	Outside diameter	Width	ES1 series	AQUA-BEARING™ series	ESA series
1200	10	30	9	1200-H-20	1200L-RT3B	ESA1200T3B
1201	12	32	10	1201-H-20	1201L-RT3B	ESA1201T3B
1202	15	35	11	1202-H-20	1202L-RT3B	ESA1202T3B
1203	17	40	12	1203-H-20	1203L-RT3B	ESA1203T3B
1204	20	47	14	1204-H-20	1204L-RT3B	ESA1204T3B
1205	25	52	15	1205-H-20	1205L-RT3B	ESA1205T3B

World's Thinnest* Microactuator Pivot Ball Bearing Assembly

This article discusses a newly developed microactuator pivot ball bearing assembly for use in ultrathin hard disk drives (HDDs) with the world's smallest height of 2.5 mm (Photo 1). The microactuator pivot ball bearing assembly (pivot unit) is used to position the read/write heads over the platter surface of a disk in an HDD assembly. Development of this product was aligned with the Japanese government's Ministry of Economy, Trade and Industry project titled, "Consortium R&D Projects for Regional Revitalization," which included a focus on research and development into high-capacity, ultrathin storage devices for digital media.

1. Structure and Specifications

The microactuator pivot ball bearing assembly (pivot unit) is used to position the read/write heads over the platter surface of a disk (Fig. 1). The torque of a pivot unit must perform while maintaining a stable level of torque so that the actuator arm can move the arm from the hub to the edge of the disk so that the heads can read/write data to platter surfaces. The pivot unit consists of two deep groove ball bearings, housing, and a shaft. The ball bearings are preloaded using adhesive material or press fitting (Fig. 2). In addition, different HDD models have different types of read/write head assemblies in addition to different methods used for mounting the HDD assembly. Furthermore, among HDDs of the same size, there are considerable variations among pivot unit designs.

Current 2.5 mm HDDs require that the pivot unit be 1.83 mm in height or less. Accordingly, NSK successfully developed and commercialized a thin, sealed bearing with a 1.5 mm bore, a 4 mm outside diameter, a 0.85 mm width, and an extremely short shaft.

Photo 1 The world's thinnest, newly developed microactuator pivot ball bearing assembly for ultrathin HDDs with a height of 2.5 mm

Ballpoint pen

1.83 mm

2.4 mm

Newly developed product for ultrathin 2.5 mm HDDs

Conventional product for 3.3 mm HDDs
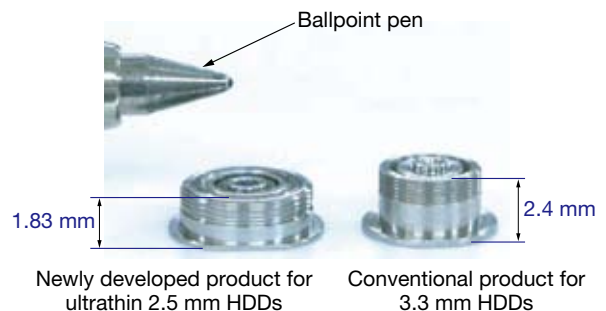
Photo 2 Comparison of the newly developed and conventional products

Magnetic head

Pivot unit

Disk

Actuator arm
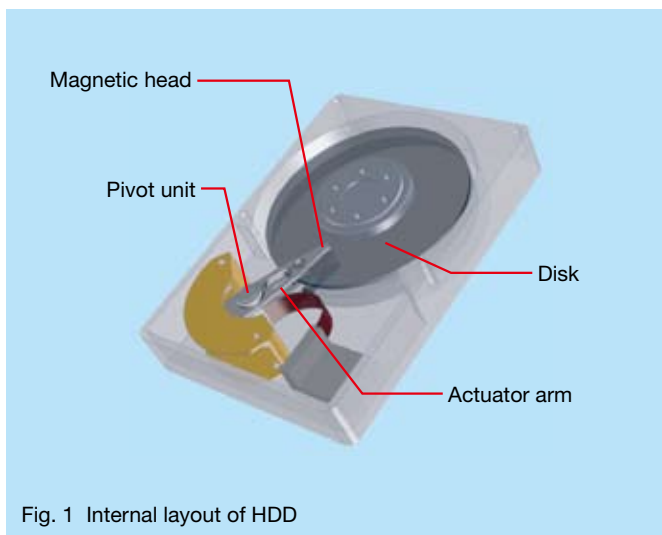
Fig. 1 Internal layout of HDD
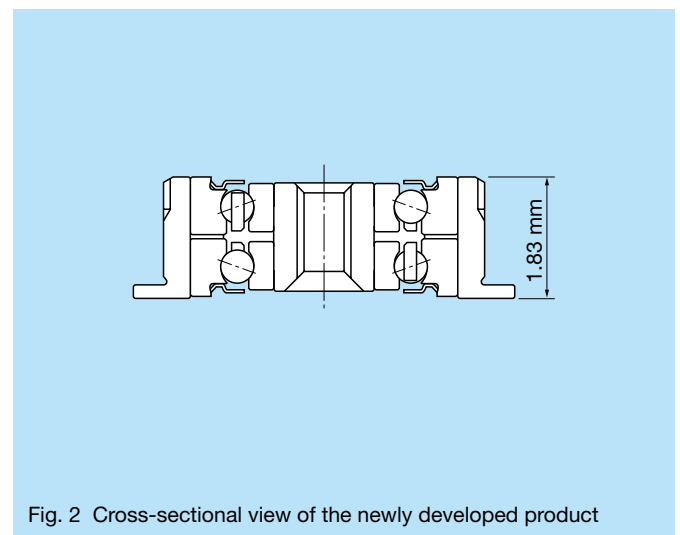
1.83 mm

Fig. 2 Cross-sectional view of the newly developed product
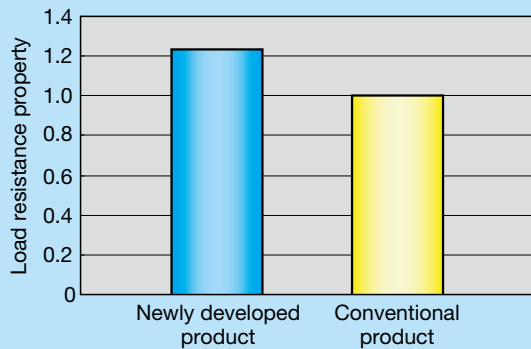
Fig. 3 Static load test results
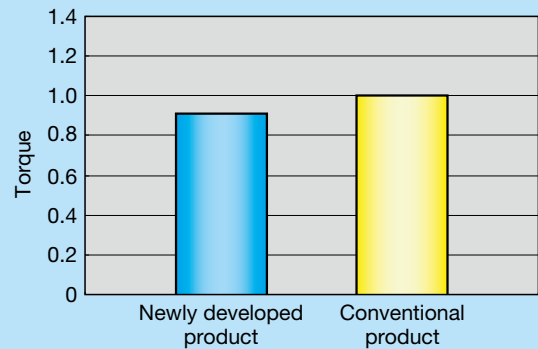
Fig. 4 Torque performance evaluation results

2. Features

(1) 1.83 mm height

At just 1.83 mm in height, and 25 % thinner than the conventional product, this microactuator pivot ball bearing assembly is the world's thinnest.

(2) Load resistance improved by 25 %

Through the use of a thinner seal and the development of an ultrathin cage, we were able to maximize the steel ball size in the bearing, which has improved load resistance by 25 % in comparison with the thinnest conventional pivot unit (Fig. 3).

(3) Lower torque

The resin cage is reinforced with nanoscale fibers, which enable the molding of a thinner cage with a minimum wall thickness of 0.1 mm and result in a lower torque level compared with those found in conventional steel cage assemblies. The thin cage wall thickness further facilitates the design of an overall thinner pivot unit (Fig. 4).

3. Conclusion

Electronic gadgets are increasingly using flash memory as the storage medium of choice. However, as technology advances, storage requirements for mobile devices will increase due to the higher volume and quality of audio and video data. Because of their exponentially higher storage capacity, HDDs are expected to meet the demands of future devices.

NSK will actively carry out product development that responds to the changing environment and needs of the future.

*According to NSK research as of May 24, 2006

Tapered Roller Bearings with an Aligning Ring for Continuous Casting Machines

Bearings for guide rolls of continuous casting machines (CCMs) are being used under severe operating conditions in which it is difficult to form a lubrication oil film. This is due not only to ultra-low operating speeds, heavy loads, and high temperatures, but also to conditions made more severe by the intrusion of water and/or scale, which is generated during the casting process. Many bearings, commonly 1 500 to 2 000 pieces, are used in an entire continuous casting machine. If only one bearing becomes severely damaged, distance between the upper and the lower guide rolls increases, which may possibly affect the quality of the steel being produced by the CCM. For this reason, highly reliable bearings with a long life are in strong demand.

Because heavy loads acting on the guide rolls of a CCM generate roll deflection, spherical roller bearings were widely adopted on both the float and the fixed positions of rolls in the past. However, spherical roller bearings are also affected by minute sliding between the rollers and raceways, which is caused by the bearing's internal geometry. In addition to the above-mentioned severe operating conditions, it was occasionally found that abnormal wear or flaking occurred on the raceway surface of the bearing's outer ring during the early stage of use, which resulted in fracturing of the outer ring.

Therefore, NSK adopted a cylindrical roller bearing that does not generate the above-mentioned sliding due to bearing geometry. During the 1980s, NSK developed and commercialized a cylindrical roller bearing with an aligning ring that accommodates misalignment at the float position on the shaft. This development dramatically improved bearing reliability and service life at the float position on the shaft. However, this type of bearing cannot be used at the fixed position on the shaft of the roll to resolve the geometrical internal sliding problem since it cannot accommodate axial loads that are generated by roll deflection or mounting errors.

Recently, NSK successfully developed the world's first tapered roller bearing with an aligning ring (Photo 1) that meets all the above requirements and resolves customer issues related to the fixed position on the roll shaft in a CCM.

Photo 1 Tapered roller bearing with aligning ring

1. Features of Tapered Roller Bearing with Aligning Ring

The NSK tapered roller bearing with aligning ring has been designed in detail using finite element method (FEM) analysis and has been further developed using NSK's advanced simulation test equipment. The features of these bearings are described below.

Tapered roller bearing with aligning ring		Spherical roller bearing
Wear depth 2 µm		Wear depth 14 µm
Roller contact length		Roller contact length
Period used	21 months	12 months

Fig. 1 Comparison of wear depth in the outer ring raceway of a tapered roller bearing with an aligning ring and that of a spherical roller bearing used in a continuous casting machine

(1) Wear resistance, long life, and axial load capacity

Unlike spherical roller bearings, tapered roller bearings do not generate sliding due to the pure rolling motion generated from the geometry of the raceway surface. Therefore, wear resistance in a tapered roller bearing with an aligning ring is dramatically improved under the severe lubricating conditions in which it is difficult to form an oil film. Observations in an actual CCM revealed that such wear in this bearing has been reduced from one-seventh to one-tenth in comparison with a conventional spherical roller bearing (Fig. 1).

In addition, bearing life has been extended by three to four times that of a standard spherical roller bearing at the fixed position as tested in an actual casting machine. Furthermore, the capability to accommodate axial loads has been dramatically improved in comparison with a spherical roller bearing or cylindrical roller bearing with a loose rib.

(2) Aligning function

A spherical seat has been formed on the outside surface of the outer ring to smoothly accommodate shaft deflection (Fig. 2).

2. Specifications

Table 1 lists the main specifications of tapered roller bearings with aligning rings.

3. Applications

This bearing is most suitable for guide rolls of continuous casting machines. It is also suitable for use at the fixed position on the shaft for various iron and steel making equipment that are subjected to shaft deflections under heavy loads that have a severe impact on service life.
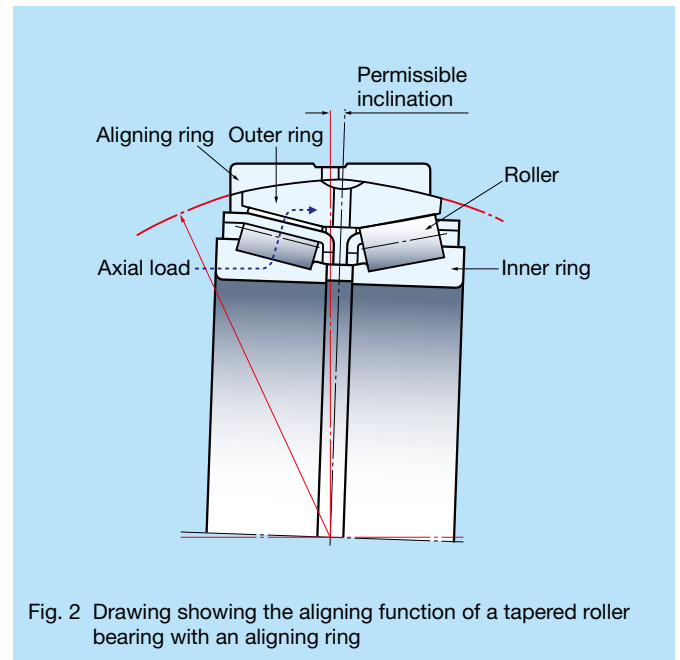
Fig. 2 Drawing showing the aligning function of a tapered roller bearing with an aligning ring

4. Conclusion

Compared with a conventional spherical roller bearing, the tapered roller bearing with aligning ring offers dramatically longer service life, which has been observed in real-world guide rolls for continuous casting machines at steelmaker sites. This bearing can contribute to boosting the reliability of continuous casting equipment, which helps to reduce the operational costs of steelmakers.

Table 1 Specifications of a tapered roller bearing with an aligning ring

Bearing number	Boundary dimensions (mm)				Basic load rating (kN)	
	d	D	B_2	C	C_r	C_{or}
AR100-42	100	180	60	46	256	390
AR110-46	110	170	45	38	171	310
AR120-30	120	180	60	48	256	525
AR130-31	130	200	69	55	320	650
AR140-24	140	210	69	55	340	690
AR140-27		225	85	70	445	905
AR150-1	150	225	75	60	395	845
AR160-11	160	240	80	65	455	935
AR180-1	180	280	100	80	665	1 430
AR200-18	200	340	112	92	895	1 630

Notes C_r: Basic dynamic load rating C_{or}: Basic static load rating
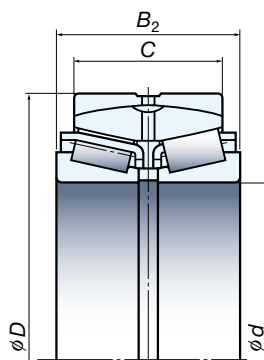
NN-Z Series of Double-Row Cylindrical Roller Bearings for Machine Tools

As built-in motorized spindles using grease lubrication for use in machining centers and numerical control (NC) lathes tend to operate at increasingly faster speeds, reliability of the non-locating (float) position bearings becomes even more important (Fig. 1).

The non-locating position bearings (Fig. 2) of a machine tool main spindle are required to accommodate thermal expansion of the shaft and must have minimal clearance between the outer ring and housing to ensure sufficient stiffness.

From a structural standpoint, cylindrical roller bearings are most suitable for such requirements. However, grease life in a cylindrical roller bearing is shorter than that of a ball bearing. Thus, there is a need for a cylindrical roller bearing that can ensure longer grease life by restricting heat generation.

In response to this need, NSK adopted its commercially successful, high-strength, roller-guided polyphenylene sulfide (PPS) resin TB cage for use in double-row cylindrical roller bearings. This NN-Z series of double-row cylindrical roller bearings (Fig. 3) was developed for exclusive use in the non-locating position of a machine tool main spindle, where it offers lower heat generation and longer life than a conventional bearing.

1. Structure

The number of rollers is optimized so that the heating value in NN type of double-row cylindrical roller bearings becomes the same as the heating value in N type.

2. Features

(1) Low temperature rise
The design of the cage has been simplified. The highly rigid, PPS resign TB cage minimizes deformation caused by centrifugal forces and facilitates the smooth rotation of rollers. Temperature rise in the NN-Z series is 50% lower than that of conventional bearings, which was achieved by optimizing the number of rollers (Fig. 4).

(2) Longer life
Grease life has been significantly improved through the adoption of the TB cage, which eliminates wear during the early stage of operation, which in turn reduces the amount of heat that is generated in the bearing.
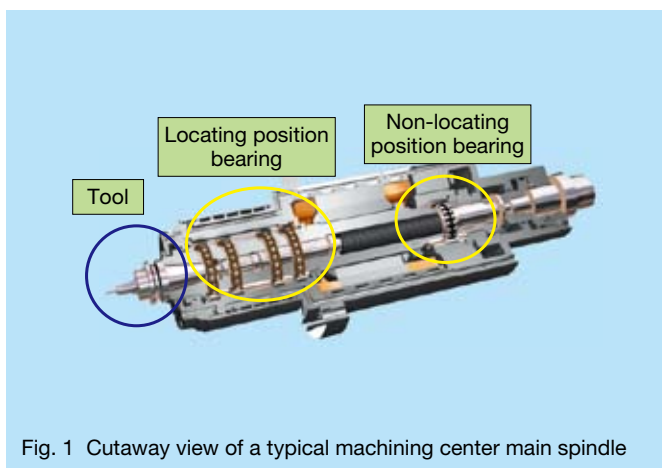
Fig. 1 Cutaway view of a typical machining center main spindle
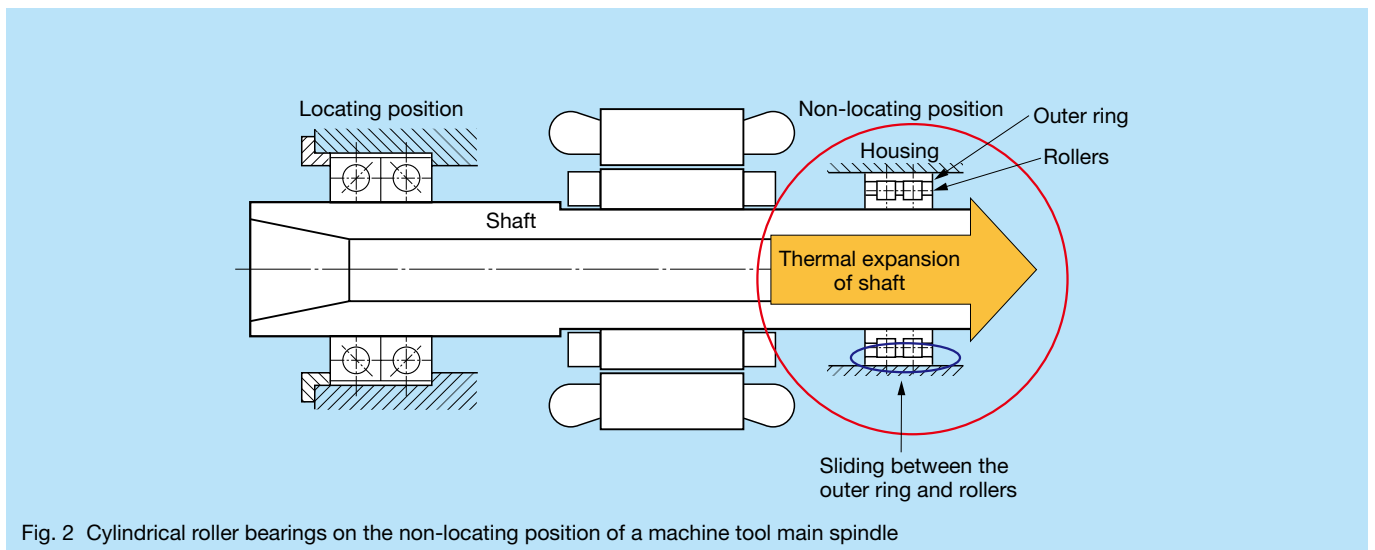
Fig. 2 Cylindrical roller bearings on the non-locating position of a machine tool main spindle

Fig. 3 NN-Z series of double-row cylindrical roller bearings
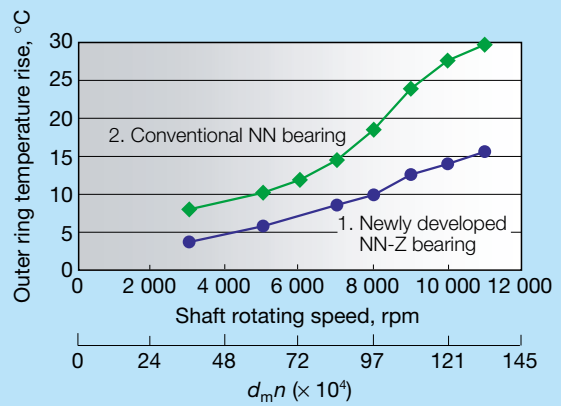
Test conditions
Bearing: NN3019
  1. Newly developed NN-Z, TB (PPS resin) cage
  2. Conventional NN, MB (copper-alloy) cage
Lubrication: grease (MTE)
Mounting clearance: 0 μm
Drive: belt (no cooling)

Fig. 4 Comparison of temperature rise

(3) Improved oil drainage

For users who prefer to use oil-air lubrication or oil-mist lubrication, NSK has improved the oil-drainage characteristics of the NN-Z series by reducing the number of rollers compared with conventional bearings. This improvement also helps reduce the number of temperature fluctuations, which are typically caused by churning resistance of the oil in the bearing.

3. Specifications

The NN-Z series is available for applications using cylindrical roller bore diameters ranging from 30 to 120 mm with a bearing accuracy of ISO Class 5 or higher.

4. Conclusion

For high-speed applications, NSK newly developed the NN-Z series. For the non-locating (float) position of machine tool spindles, the NN-Z series of double-row cylindrical roller bearings has adopted the TB cage and features lower heat generation and longer life compared with conventional bearings. This series also provides higher reliability for machine tool main spindles.

New Global Standard of Packaging for Precision-Class Bearings

Conventionally packaged precision-class bearings for machine tool main spindles require cleaning and packing of grease before mounting. To improve the efficiency and production capacity of machine tools, a type of packaging that reduces the amount of time required to mount the bearings is needed and in demand.

NSK addressed this issue by redesigning the way precision-class bearings are packaged at all production sites across the globe (Photos 1 and 2). Precision-class bearings are prepacked with grease, which also helps to prevent corrosion during shipping and storage. This article provides a detailed description of this new packaging.

1. Features

With this new packaging (Fig. 1), customers are no longer required to wash the bearings nor are they required to pack grease into them prior to mounting. Additional features include the following.

(1) Reliability
Bearings are prepacked with the optimal amount of NSK's standard specification MTE grease. MTE grease, which continues to have a favorable reputation in the field, provides superior durability in high-speed machine tool applications.

(2) Prevention of rust, leakage, and contamination
The bearings are enclosed in a volatile corrosion inhibitor (VCI) bag. VCI packaging uses heat-sealed shrink-film to prevent contamination, the formation of rust, and the leakage of grease.

(3) Work efficiency
Laser markings on the bearing indicate bore diameter, outside diameter, and width. These laser markings make it easier to confirm the boundary dimensions at the time of mounting.

(4) Environmentally friendly
Metallic lamination on the exterior of the shipment box has been eliminated and replaced with markings using a specific paint that facilitates easy recycling of the cardboard box.

(5) Packaging for oil-lubricated bearings
Bearings that will use oil lubrication instead of prepacked grease are also shipped in VCI packaging that uses heat-sealed shrink-film. The need for customers to wash the bearing prior to mounting has been eliminated by the use of a minimal amount of rust-preventive oil.

Photo 1 NSK group-wide recyclable cardboard box used for external packaging (golden shipment box)

Photo 2 NSK group-wide internal VCI packaging using heat-sealed shrink film

Fig. 1　Comparison of mounting procedures using conventionally packaged bearings (below) and the new standard packaging specification (top)

2. Bearing Size Lineup

This new packaging is applicable to angular contact ball bearings with a bore diameter ranging from 10 to 130 mm with an ISO Accuracy Class of P4 or higher.

3. Conclusion

NSK's global standard of packaging for precision-class bearings significantly shortens the amount of time required to mount the bearings to a machine tool spindle and eliminates the need to wash the bearings prior to mounting. In addition, grease-lubricated bearings come prepacked with the optimal amount of grease to ensure machine tool reliability.

Customers can also benefit from the ease of mounting and improved efficiency afforded by the adoption of this new packaging when replacing bearings during repairs or retrofitting older bearings with NSK precision-class bearings.

V1 Series of Ball Screws for Contaminated Environments

Ball screws are used in various applications where they risk exposure to severe operating conditions, including contamination and debris that adhere to the screw shaft. Under such conditions, ingression of foreign particles can cause abnormal wear of the circulating path surface or ball elements, and smooth ball movement can be hampered in the recirculation circuit leading to early failure of the ball screw.

Therefore, measures have been taken that include the use of wiper seals to remove debris from the screw shaft

Photo 1 V1 series of ball screws for contaminated environments

and the use of bellow covers to establish a physical barrier between debris and the ball screw shaft.

Although wiper seals are put into practical use, they lack sufficient sealing performance due to the difficulty in maintaining uniform contact around the screw shaft. Because of the relatively wide contact area of a wiper seal, high-speed applications are subject to friction-generated heat. In addition, structural considerations may preclude the installation of appropriate covers, thus minute particles can still drift past the barrier and contaminate the shaft. As a result, there is growing demand for high-speed ball screws that provide sufficient protection against contamination and debris while ensuring long-life performance and low frictional torque.

NSK has developed and marketed its V1 series of ball screws for contaminated environments to meet these market needs. The V1 series offers long-life performance, low frictional torque, and excellent high-speed capability, and it provides sufficient resistance against debris and contamination. This article provides an overview of the series (Photo 1 and Fig. 1).

1. Features

The features of the V1 series ball screws, which include high-performance seals, are described below.

(1) Highly resistant against debris

The flat-lip contact seal (patent pending) and enhanced groove profile significantly improve resistance against contamination. The penetration rate of foreign particles was reduced to about 1/15 that of the standard
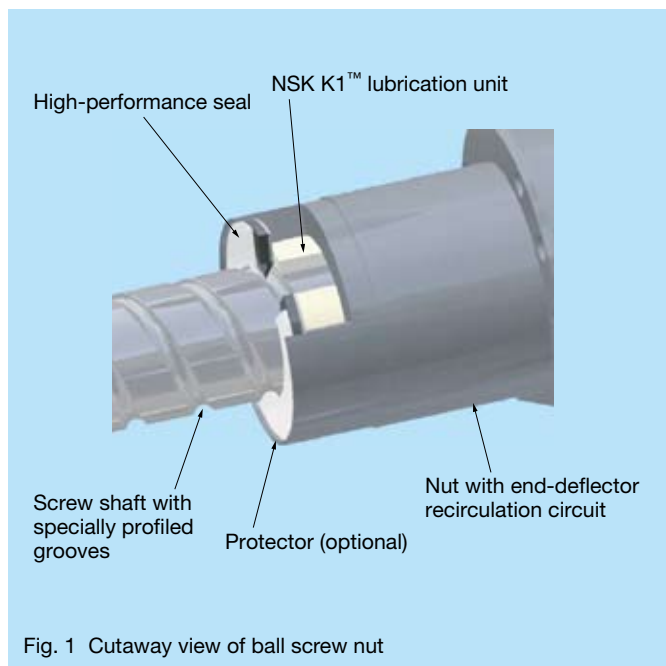
Fig. 1 Cutaway view of ball screw nut
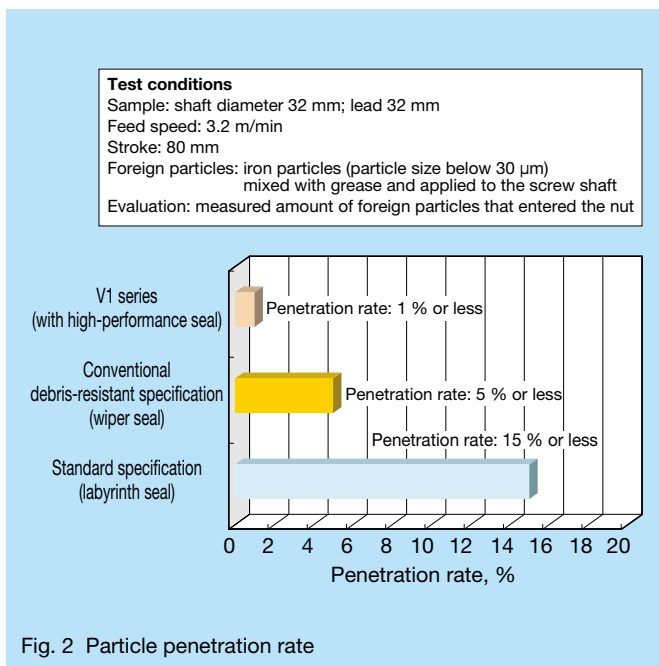
Fig. 2 Particle penetration rate
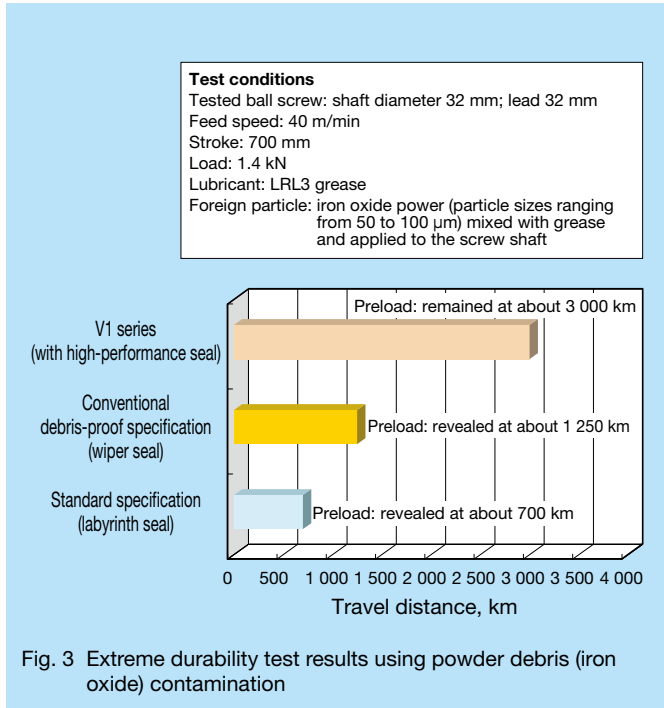
Fig. 3 Extreme durability test results using powder debris (iron oxide) contamination

Test conditions
Tested ball screw: shaft diameter 32 mm; lead 32 mm
Feed speed: 40 m/min
Stroke: 700 mm
Load: 1.4 kN
Lubricant: LRL3 grease
Foreign particle: iron oxide power (particle sizes ranging from 50 to 100 μm) mixed with grease and applied to the screw shaft

V1 series (with high-performance seal) — Preload: remained at about 3 000 km
Conventional debris-proof specification (wiper seal) — Preload: revealed at about 1 250 km
Standard specification (labyrinth seal) — Preload: revealed at about 700 km

Fig. 4 Variation in frictional torque of seal due to rotating speed of ball screw

Test conditions
Tested ball screw: shaft diameter 32 mm; lead 10 mm
Lubricant: ISO VG68 oil

Conventional debris-proof specification (wiper seal)
V1 series (high performance seal)

specification and reduced to about 1/5 that of the wiper seal specification (Fig. 2).

(2) Highly durable in contaminated environments

Being highly resistant against contamination from debris significantly improved durability in severe environments. The particle penetration test with ultrafine iron particles established a four-fold improvement in durability over the standard specification (Fig. 3). In addition, lubricating the lip using the NSK K1™ lubrication unit mounted inside the seal further improved the seal's durability.

(3) Low friction and low heat generation

The optimized lip profile and material improved debris-resistant performance and durability as well as low frictional torque. Seal torque was reduced (Fig. 4) and heat generation caused by the seals was significantly minimized compared with the conventional wiper seals.

(4) Excellent high-speed performance

The recirculation circuit with end deflectors at each nut ensures ultimate smoothness of ball circulation and enables a $d·n$ value of up to 15×10^4 and ultrahigh speeds of 150 m/min maximum at significantly reduced noise levels. Incidentally, the term "$d·n$ value" represents the product of shaft diameter (d mm) and rotational speed (n min^{-1}).

Table 1 Product lineup

Unit: mm

Shaft diameter	Lead						Maximum shaft length
	10	16	20	32	40	50	
⌀32	◯	◯	◯	◯			2 800
⌀40					◯		3 800
⌀50						◯	5 000

2. Specifications

Table 1 shows the combination of shaft diameter and lead as well as the maximum shaft length of the V1 series. JIS C5 lead accuracy is available as standard.

3. Applications

Typical applications include laser-cutting machines, tire buffers, woodworking machinery, chip mounters, and others.

HTF-SRC Series of Ball Screws for High-Speed and High-Load Applications

Injection molding machines and other applications using feed mechanisms that are subjected to high loads have conventionally used hydraulic feed mechanisms. In recent years, however, there has been a rapid shift from hydraulic to electric methods using ball screws and rotating motors to improve feed accuracy, improve control, and reflect environmental considerations.

NSK marketed the HTF series of ball screws for high-load applications in 1996 in advance of other companies.

The latest injection molding machines are not only required to precisely mold parts with super-thin walls, including parts for IT equipment such as digital cameras and cellular phones, but must also increase productivity. High-speed and highly responsive injection performance is needed to meet these demands. Consequently, feed screws offering faster rotating speeds have also become necessary.

To meet these demands, NSK thoroughly reviewed the ball screw's recirculation mechanism, a critical factor in determining the high-speed limits of a ball screw, and developed the HTF-SRC series (Photo 1), which uses a newly developed recirculation circuit. This article provides an overview of this product.

1. Features

The HTF-SRC series features improvements in high-speed, quiet operation based on the conventional HTF series of ball screws for high-load applications.

This series uses the new smooth-return coupling (SRC) recirculation circuit (Fig. 1) in place of a conventional ball recirculation circuit. The smooth ball circulation of the SRC recirculation circuit features the following:

(1) High-speed performance

Achieves a maximum feed speed ranging from $d \cdot n$ 140 000 to 160 000 (shaft diameter $d \times$ revolutions n), which is more than twice the performance of conventional products.

This capability enables high-speed injection rates at 500 mm/s or higher.

(2) Quiet operation

The new recirculation circuit achieves smooth ball circulation, reducing noise levels by 1/2 to 2/3, which is 6 to 10 dB lower than conventional products. Fig. 2 shows noise levels compared with the conventional HTF series.

Photo 1 HTF-SRC series

Sharp bend in section of recirculation circuit

Smooth and continuous recirculation of balls in a tangent to the helical ball path

Conventional ball recirculation circuit

SRC recirculation circuit
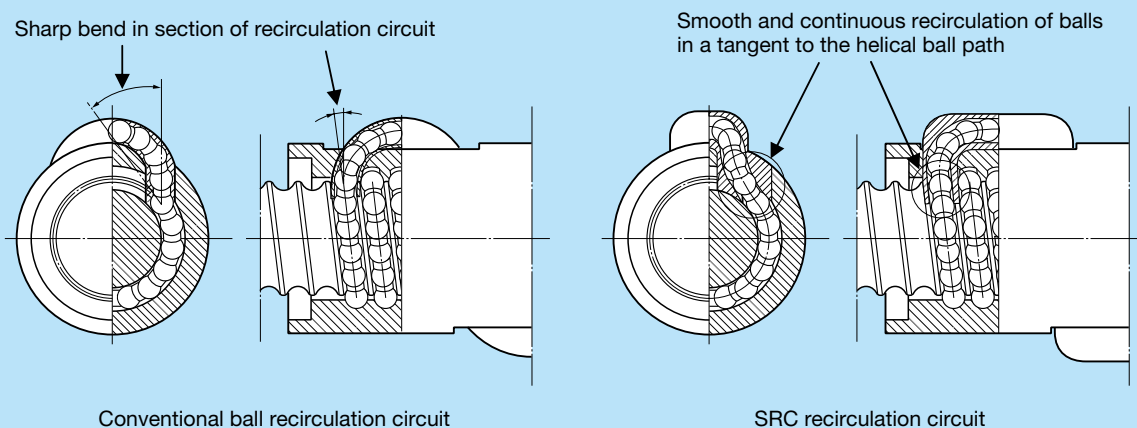
Fig. 1 Comparison of a conventional ball recirculation circuit and the SRC recirculation circuit

(3) High-load capacity

The internal design, which responds to high-load capacity and is a feature of the HTF series, has been retained. As before, the design is applicable to a variety of shaft-end shapes, including splines for large driving torque.

2. Specifications

· SRC type ball recirculation circuit
· Lead accuracy conforms to JIS C5 and Ct7
· Available in seven combinations of shaft diameter and lead (Table 1)

3. Applications

The HTF-SRC series ball screws are suitable for a wide range of applications such as electric injection molding machines, die casting machines, IC molding presses, servo presses, press brakes, and turret presses.
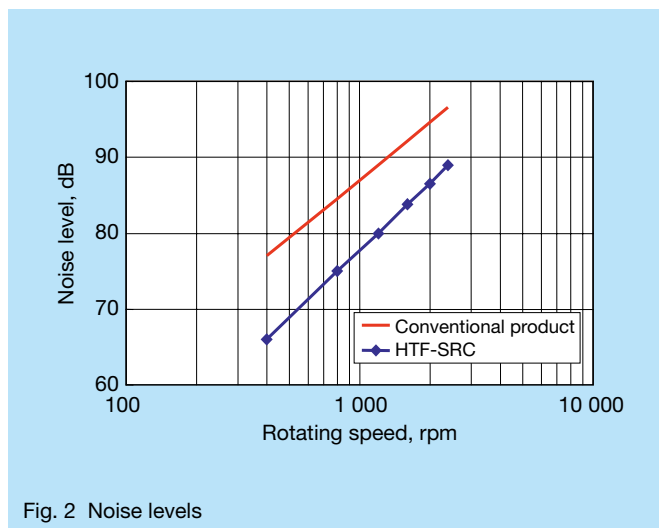
Fig. 2 Noise levels

Table 1 Series lineup

	Shaft diameter (mm)	Lead (mm)	Basic load ratings (N)		Feed (mm/s)	
			Dynamic (C_a)	Static (C_{oa})	$d \cdot n$ 140 000	$d \cdot n$ 160 000
HTF-SRC 5016-7.5	50	16	306 000	818 000	—	860
HTF-SRC 6316-10.5	63	16	450 000	1 450 000	—	680
HTF-SRC 6320-7.5		20	457 000	1 280 000	740	—
HTF-SRC 8016-10.5	80	16	501 000	1 870 000	—	540
HTF-SRC 8020-10.5		20	671 000	2 300 000	590	—
HTF-SRC 10020-10.5	100	20	749 000	2 910 000	470	—
HTF-SRC 10025-10.5		25	964 000	3 430 000	590	—

NSK RA Series of Roller Linear Guides with Interchangeable Rails & Sliders with Guaranteed Preload

The NSK RA series of roller linear guides was launched in 2004, boasting the world's highest load capacity and highest rigidity. Since then, the outstanding performance and reliability of the RA series have gained public attention and a favorable reputation the world over. This series has attracted many inquiries, and the range of applications for this linear guide has been growing dramatically.

To provide quick delivery and to meet the strong demand for the RA series for use in machine tools found throughout Europe, China, and other Asian countries, as well as automotive manufacturing equipment and LCD manufacturing equipment in Japan, the interchangeable rails and sliders of NSK's latest RA series of roller linear guides now come preloaded and are available in single-unit quantities (Photo 1), which gives customers greater flexibility in randomly matching rails and sliders according to their needs.

1. Features

Features of the new RA series of interchangeable rails and sliders are as follows.

(1) Highly accurate, preloaded, interchangeable rails and sliders

Improved accuracy of the rail raceway surfaces and of the mounting surfaces (parallelism and perpendicularity) provide excellent preload accuracy, profile accuracy, and constant rigidity with any combination of rail and slider.

(2) Quick delivery

The rails and sliders are available in single unit quantities, allowing us to easily fill customer orders for varying combinations, thus ensuring quick delivery.

(3) Profile accuracy

Dimensional tolerances have been significantly improved and have been reduced to half that of the conventional RA series through higher machining accuracy of the rails and sliders. Table 1 lists the accuracy standards.

Photo 1 Extended lineup of the NSK RA series of roller linear guide rails and sliders, which are available in preloaded single-unit quantities

Table 1 Accuracy standards
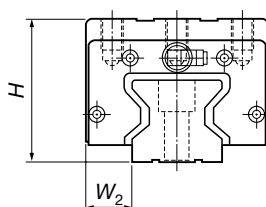
Unit: mm

Accuracy grade		Precision grade P6
Assembly height H	Tolerance	± 0.020
	Dimensional variation (on same rail)	0.015
Assembly width W_2	Tolerance	± 0.025
	Dimensional variation	0.020

(4) Replacing and adding sliders

Sliders are available in either the standard square shape or with a mounting flange. Either type of slider can be used on the same rail. Each slider can also be replaced or added according to user needs.

(5) Extended maintenance-free performance

Units can be equipped with NSK K1™ lubrication units to ensure long-term maintenance-free performance.

(6) Highly resistant against debris

The high-performance seal ensures excellent durability in contaminated environments. Optional rail covers are also available for even more severe operating conditions.

2. Accuracy and Preload

Precision grade P6 is available with medium preload (Z3).

3. Model Numbers and Dimensions

Tables 2 and 3 list available model numbers and boundary dimensions of this RA series of roller linear guides with preloaded, interchangeable rails and sliders.

4. Applications

This series of roller linear guides is suitable for machine tools, automotive manufacturing equipment, LCD manufacturing equipment, medical equipment, and more.

Table 2 Dimensions for types AL, AN, BL, and BN

Unit: mm

Model numbers	Assembly dimensions			Slider dimensions						Rail dimensions		Basic load ratings				
	Height			Width	Length		Grease nipple			Width	Height	Dynamic	Static	Static moment		
							Mounting hole									
	H	E	W_2	W	L	L_1		T_1	N	W_1	H_1	C (N)	C_o (N)	Rolling (N·m)	Pitching (N·m)	Yawing (N·m)
RA25AL	36	5	12.5	48	97.5	65.5	M6×0.75	6	11	23	24	29 200	72 700	970	760	760
RA25AN	40							10								
RA25BL	36				115.5	83.5		6				35 400	92 900	1 240	1 240	1 240
RA25BN	40							10								
RA30AL	42	6.5	16	60	110.8	74	M6×0.75	7	11	28	28	38 900	93 500	1 670	1 140	1 140
RA30AN	45							10								
RA30BL	42				135.4	98.6		7				47 600	121 000	2 170	1 950	1 950
RA30BN	45							10								
RA35AL	48	6.5	18	70	123.8	83.2	M6×0.75	8	11	34	31	53 300	129 000	2 810	1 800	1 800
RA35AN	55							15								
RA35BL	48				152	111.4		8				67 400	175 000	3 810	3 250	3 250
RA35BN	55							15								
RA45AL	60	8	20.5	86	154	105.4	Rc1/8	10	14	45	38	92 800	229 000	6 180	4 080	4 080
RA45AN	70							20								
RA45BL	60				190	141.4		10				116 000	305 000	8 240	7 150	7 150
RA45BN	70							20								
RA55AL	70	9	23.5	100	184	128	Rc1/8	11	14	53	43.5	129 000	330 000	10 200	7 060	7 060
RA55AN	80							21								
RA55BL	70				234	178		11				168 000	462 000	14 300	13 600	13 600
RA55BN	80							21								
RA65AN	90	13	31.5	126	228.4	155.4	Rc1/8	19	14	63	55	210 000	504 000	19 200	12 700	12 700
RA65BN					302.5	229.5						288 000	756 000	28 700	28 600	28 600

Square type: AN (for high-load applications), BN (for super high-load applications)
Square low type: AL (for high-load applications), BL (for super high-load applications)

Table 3 Dimensions for types EM and GM

Unit: mm

Model numbers	Assembly dimensions			Slider dimensions						Rail dimensions		Basic load ratings				
	Height			Width	Length		Grease nipple			Width	Height	Dynamic	Static	Static moment		
	H	E	W_2	W	L	L_1	Mounting hole	T_1	N	W_1	H_1	C (N)	Co (N)	Rolling (N·m)	Pitching (N·m)	Yawing (N·m)
RA25EM	36	5	23.5	70	97.5	65.5	M6×0.7	6	11	23	24	29 200	72 700	970	760	760
RA25GM					115.5	83.5						35 400	92 900	1 240	1 240	1 240
RA30EM	42	6.5	31	90	110.8	74	M6×0.7	7	11	28	28	38 900	93 500	1 670	1 140	1 140
RA30GM					135.4	98.6						47 600	121 000	2 170	1 950	1 950
RA35EM	48	6.5	33	100	123.8	83.2	M6×0.75	8	11	34	31	53 300	129 000	2 810	1 800	1 800
RA35GM					152	111.4						67 400	175 000	3 810	3 250	3 250
RA45EM	60	8	37.5	120	154	105.4	Rc1/8	10	14	45	38	92 800	229 000	6 180	4 080	4 080
RA45GM					190	141.4						116 000	305 000	8 240	7 150	7 150
RA55EM	70	9	43.5	140	184	128	Rc1/8	11	14	53	43.5	129 000	330 000	10 200	7 060	7 060
RA55GM					234	178						168 000	462 000	14 300	13 600	13 600
RA65EM	90	13	53.5	170	228.4	155.4	Rc1/8	19	14	63	55	210 000	504 000	19 200	12 700	12 700
RA65GM					302.5	229.5						288 000	756 000	28 700	28 600	28 600

Flange type: EM (for high-load applications), GM (for super high-load applications)

5. Conclusion

The RA series of roller linear guides allows for random matching of preloaded, interchangeable rails and sliders, which has been made possible by the improved dimensional accuracy of the rails and sliders. Customers can freely combine the rails and sliders while maintaining the high performance and outstanding reliability of the standard RA series roller guides. Single unit quantities of rails and sliders are kept in stock for quick delivery. Such flexibility in parts procurement facilitates timely implementation of slider changes, adding sliders, or modifying slider types and specifications on the user side for greater convenience.

Notes

Notes

Notes

Worldwide Sales Offices and Manufacturing Plants

NSK LTD.-HEADQUARTERS, TOKYO, JAPAN
www.nsk.com

Nissei Bldg., 1-6-3 Ohsaki, Shinagawa-ku, Tokyo 141-8560, Japan
INDUSTRIAL MACHINERY BUSINESS DIVISION-HEADQUARTERS
P: 03-3779-7227   F: 03-3779-7644   C: 81
GLOBAL AFTERMARKET DEPARTMENT
P: 03-3779-7253   F: 03-3779-7644   C: 81
PRECISION MACHINERY DEPARTMENT
P: 03-3779-7163   F: 03-3779-7644   C: 81
MECHATRONICS BUSINESS DEPARTMENT
P: 0466-21-3027   F: 0466-21-3206   C: 81
AUTOMOTIVE BUSINESS DIVISION-HEADQUARTERS
P: 03-3779-7189   F: 03-3779-7917   C: 81

●Africa
South Africa:
NSK SOUTH AFRICA (PTY) LTD.
JOHANNESBURG   25 Galaxy Avenue, Linbro Business Park, Sandton, Gauteng, P.O. Box 1157, Kelvin, 2054, South Africa
P: 011-458-3600   F: 011-458-3608   C: 27

●Asia and Oceania
Australia:
NSK AUSTRALIA PTY. LTD.   www.au.nsk.com
MELBOURNE   11 Dalmore Drive, Scoresby, Victoria 3179, Australia
P: 03-9764-8302   F: 03-9764-8304   C: 61
SYDNEY   24-28 River Road West, Parramatta, New South Wales 2150, Australia
P: 02-8843-8100   F: 02-9893-8406   C: 61
BRISBANE   1/69 Selhurst Street, Coopers Plains, Queensland 4108, Australia
P: 07-3347-2600   F: 07-3345-5376   C: 61
PERTH   Unit 1, 71 Tacoma Circuit, Canning Vale, Western Australia 6155, Australia
P: 08-9256-5000   F: 08-9256-1044   C: 61

China:
NSK HONG KONG LTD.
HONG KONG   Suite 814, World Commerce Centre, Harbour City, T.S.T, KLN, Hong Kong
P: 2739-9933   F: 2739-9323   C: 852
SHENZHEN   Room 8B08-09, Jueshi Tower, Jiabing Road, Luohu, Shenzhen, China (518001)
P: 0755-25904886   F: 0755-25904883   C: 86
KUNSHAN NSK CO., LTD.
OFFICE/PLANT   258 South Huang Pu Jiang Rd., Kunshan Economic & Technical Development Zone, Jiang Su, China (215335)
P: 0512-5771-5654   F: 0512-5771-5689   C: 86
CHANGSHU NSK NEEDLE BEARING CO., LTD.
OFFICE/PLANT   No. 66 Dongnan Road, Changshu Southeast Economic Development Zone, Changshu City, Jiangsu, China (215500)
P: 0512-5230-1111   F: 0512-5230-6011   C: 86
NSK STEERING SYSTEMS DONGGUAN CO., LTD.
OFFICE/PLANT   High-tech Park, Shilong Road, Guanlong Section, Dongguan, Guangdong, China (523119)
P: 0769-2262-0960   F: 0769-2316-2867   C: 86
ZHANGJIAGANG NSK PRECISION MACHINERY CO., LTD.
OFFICE/PLANT   No. 34 Zhenxing Road, Zhangjiagang Economic Development Zone, Zhangjiagang City, Jiangsu Province, China (215600)
P: 0512-5867-6496   F: 0512-5818-0970   C: 86
SUZHOU NSK BEARINGS CO., LTD.
OFFICE/PLANT   No. 22 Taishan Road, Suzhou New District, Jiangsu, China (215129)
P: 0512-6665-5666   F: 0512-6665-9138   C: 86
NSK (CHINA) RESEARCH & DEVELOPMENT CO., LTD.
JIANGSU   No.8 NSK Rd., Huaqiao Economic Development Zone, Kunshan, Jiangsu, China
P: 0512-5796-3000   F: 0512-5796-3300   C: 86
NSK (SHANGHAI) TRADING CO., LTD.
JIANGSU   No.8 NSK Rd., Huaqiao Economic Development Zone, Kunshan, Jiangsu, China
P: 0512-5796-3000   F: 0512-5796-3300   C: 86
NSK (CHINA) INVESTMENT CO., LTD.   www.nsk.com.cn
HEAD OFFICE   No.8 NSK Rd., Huaqiao Economic Development Zone, Kunshan, Jiangsu, China
P: 0512-5796-3000   F: 0512-5796-3300   C: 86
BEIJING   Room 2116, Beijing Fortune Bldg., 5 Dong San Huan Bei Lu, Chao Yang District, Beijing, China (100004)
P: 010-6590-8161   F: 010-6590-8166   C: 86
GUANGZHOU   Room 3101/3102/3106A, Guangdong Telecom Plaza, 18 Zhongshan Er Road, Guangzhou, Guangdong, China (510080)
P: 020-3786-4833   F: 020-3786-4501   C: 86
CHENGDU   Room1901, Green Land Hotel, No.99 Zhonglieci Xi Street, Chengdu,Sichuan Province, China (610016)
P: 028-8661-4200   F: 028-8661-4343   C: 86
NSK CHINA SALES CO., LTD.
SHANGHAI   Room 01-03, Tower B 27F, Far East International Plaza, No.317 Xianxia Road, Shanghai, China (200051)
P: 021-6235-0198   F: 021-6235-1858   C: 86
CHANGCHUN   Room 1001, Building A, Zhongyin Building, 727 Xi'an Road, Changchun, Jilin Province, China (130061)
P: 0431-8898-8682   F: 0431-8898-8670   C: 86
TIAN JIN   Room 06, 09F The Exchange Tower 2, No. 189 NanJing Road, Heping District, Tianjin, China (300050)
P: 022-8319-5030   F: 022-8319-5033   C: 86
NANJING   A1 22F, Golden Eagle International Plaza, No.89 Hanzhong Road, Nanjing, Jiangsu Province, China (210029)
P:025-8472-6671   F:025-8472-6687   C:86
CHONGQING   Room 2306, Unit B, No.137, Keyuan 2nd Road, Jiulongpo District, Chonqing, China (400039)
P:023-6806-5310   F:023-6806-5292   C:86
NSK-WARNER (SHANGHAI) CO., LTD.
PLANT   No. 2518 Huancheng Road (West) Fengxian District, Shanghai,China (201401)
P: 021-3365-5757   F: 021-3365-5262   C: 86

AKS PRECISION BALL (HANGZHOU) CO., LTD.
PLANT   No. 189 Hongda Road, Xiaoshan Area of Economic & Technological Development Zone, Hangzhou, Zhejiang, China (311231)
P: 0571-2280-1288   F: 0571-2280-1268   C: 86
NSK-YAGI PRECISION FORGING (ZHANGJIAGANG) CO., LTD.
PLANT   No. 34 Zhenxing Road, Zhangjiagang Economic Development Zone, Zhangjiagang City, Jiangsu Province, China (215600)
P:0512-5867-6496   F:0512-5818-0970   C:86
NSK-WANDA ELECTRIC POWER ASSISTED STEERING SYSTEMS CO.,LTD.
OFFICE/PLANT   1833 Yatai Road, Wenyan Town, Xiaoshan, Hangzhou, Zhejiang, China (311258)
P:0571-8230-2735   F:0571-8230-2692   C:86
India:
RANE NSK STEERING SYSTEMS LTD.
CHENNAI   14, Rajagopalan Salai, Vallancherry, Guduvancherry, Tamil Nadu-603 202, India
P:044-474-06017   F:044-274-66001   C:91
BAWAL   Plot No.28A, Sector 6, HSIIDC Growth Centre Bawal, District Rewari, Haryana -123 501, India
P:01284-264281   F:01284-264280   C:91
NSK INDIA SALES CO.PVT.LTD.
CHENNAI   New No.7, Old No.5, Boat Club Road, Chennai-600 028, India
P:044-2433-1161   F:044-2433-1160   C:91
GURGAON   311, JMD Pacific Square, Sector 15 (II), 32nd Milestone, National Highway-8, Gurgaon, Haryana-122 001, India
P:0124-4104-530   F:0124-4104-532   C:91
KOLKATA   502, Trinity Towers, 83, Topsia Road, Kolkata-700 046, India
P:033-4001-2062   F:033-4001-2064   C:91
MUMBAI   321, A Wing, Ahura Centre, 82, Mahakali Caves Road, Andheri East, Mumbai -400 093, India
P:022-2838-7787   F:022-2838-5191   C:91
NSK-ABC BEARINGS LTD.
OFFICE/PLANT   Plot No.A2, SIPCOT Growth Centre, Oragadam, Mathur Village, Sriperumbudur Taluk, Kancheepuram District, Tamil Nadu-602 105, India
P:044-2714-3000   F:044-2714-3099   C:91
Indonesia:
PT. NSK BEARINGS MANUFACTURING INDONESIA
JAKARTA PLANT   Blok M4, Kawasan Berikat MM2100 Industrial Town Cikarang Barat, Bekasi 17520, Indonesia
P: 021-898-0155   F: 021-898-0156   C: 62
PT. NSK INDONESIA   www.id.nsk.com
JAKARTA   Summitmas II, 6th Floor, Jl. Jend Sudirman Kav. 61-62, Jakarta 12190, Indonesia
P: 021-252-3458   F: 021-252-3223   C: 62
PT. NSK-WARNER INDONESIA
BEKASI   MM2100 Industrial Town, Cikarang Barat, Bekasi 17520, Indonesia
P: 021-8998-3216   F: 021-8998-3218   C: 62
Korea:
NSK KOREA CO., LTD.   www.kr.nsk.com
SEOUL   Posco Center (West Wing) 9F, 892, Daechi-4Dong, Kangnam-Ku, Seoul, 135-777, Korea
P: 02-3287-0300   F: 02-3287-0345   C: 82
CHANGWON   60, Seongsan-Dong, Changwon, Kyungsangnam-Do, 641-315, Korea
PLANT   P: 055-287-6001   F: 055-285-9982   C: 82
Malaysia:
NSK BEARINGS (MALAYSIA) SDN. BHD.   www.my.nsk.com
HEAD OFFICE   No. 2, Jalan Pemaju, U1/15, Seksyen U1, Hicom Glenmarie Industrial Park, 40150 Shah Alam, Selangor, Malaysia
P: 03-7803-8859   F: 03-7806-5982   C: 60
PRAI   No.36, Jalan kikik, Taman Inderawasih, 13600 Prai, Penang, Malaysia
P: 04-3902275   F: 04-3991830   C: 60
JOHOR BAHRU   88 Jalan Ros Merah 2/17, Taman Johor Jaya, 81100 Johor Bahru, Johor, Malaysia
P: 07-3546290   F: 07-3546291   C: 60
KOTA KINABALU   Lot 10, Lrg Kurma 4, Likas Ind. Centre, 5/12 Miles Jln Tuaran, 88450 Inanam, Sabah, Malaysia
P: 088-421260   F: 088-421261   C: 60
IPOH   Gr. Floor, 89 Jalan Bendahara, 31650 Ipoh, Perak, Malaysia
P: 05-2555000   F: 05-2553373   C: 60
NSK MICRO PRECISION (M) SDN. BHD.   www.my.nsk.com
MALAYSIA PLANT   No.43 Jalan Taming Dua,Taman Taming Jaya 43300 Balakong, Selangor Darul Ehsan, Malaysia
P: 03-8961-3960   F: 03-8961-3968   C: 60
New Zealand:
NSK NEW ZEALAND LTD.   www.nsk-rhp.co.nz
AUCKLAND   3 Te Apunga Place, Mt. Wellington, Auckland, New Zealand
P: 09-276-4992   F: 09-276-4082   C: 64
Philippines:
NSK REPRESENTATIVE OFFICE
MANILA   8th Floor The Salcedo Towers 169 H.V. dela Costa St., Salcedo Village Makati City, Philippines 1227
P: 02-893-9543   F: 02-893-9173   C: 63
Singapore:
NSK INTERNATIONAL (SINGAPORE) PTE LTD.
SINGAPORE   238A, Thomson Road, #24-01/05, Novena Square Tower A, Singapore 307684
P: 6496-8000   F: 6250-5845   C: 65
NSK SINGAPORE (PRIVATE) LTD.   www.nsk-singapore.com.sg
SINGAPORE   238A, Thomson Road, #24-01/05, Novena Square Tower A, Singapore 307684
P: 6496-8000   F: 6250-5845   C: 65
Taiwan:
TAIWAN NSK PRECISION CO., LTD.
TAIPEI   11F., No.87, Song Jiang Rd., Jhongshan District, Taipei City 104, Taiwan R.O.C.
P: 02-2509-3305   F: 02-2509-1393   C: 886
TAICHUNG   107-7, Sec. 3, Wen Xing Rd., Taichung City 407, Taiwan R.O.C.
P: 04-2311-7978   F: 04-2311-2627   C: 886
TAINAN   No.8 Daye 1st Rd., Southern Taiwan Science Park, Tainan County 741, Taiwan R.O.C.
P: 06-505-5861   F: 06-505-5061   C: 886

Worldwide Sales Offices and Manufacturing Plants

P: Phone   F: Fax   C: Country Code   Printed in Japan

TAIWAN NSK TECHNOLOGY CO., LTD.
TAIPEI   11F., No. 87, Songjiang Rd., Jhongshan District, Taipei City 104, Taiwan R.O.C.
                  P: 02-2509-3305   F: 02-2509-1393   C: 886
Thailand:
NSK BEARINGS (THAILAND) CO.,LTD.
BANGKOK   26 Soi On-Nuch 55/1 Pravet District, Bangkok 10250, Thailand
                  P: 02320-2555   F: 02320-2826   C: 66
NSK BEARINGS MANUFACTURING (THAILAND) CO., LTD.
OFFICE/PLANT   700/430 Moo 7, Amata Nakorn Industrial Estate, T.Donhualor, A.Muangchonburi,
                  Chonburi 20000, Thailand
                  P: 038-454-010   F: 038-454-017   C: 66
SIAM NSK STEERING SYSTEMS CO., LTD.
OFFICE/PLANT   90 Moo 9, Wellgrow Industrial Estate, Km.36 Bangna-Trad Rd., Bangwao,
                  Bangpakong, Chachoengsao 24180, Thailand
                  P: 038-522-343   F: 038-522-351   C: 66
NSK ASIA PACIFIC TECHNOLOGY CENTRE (THAILAND) CO., LTD.
CHONBURI   700/430 Moo 7, Amata Nakorn Industrial Estate, T.Donhualor, A.Muangchonburi,
                  Chonburi 20000, Thailand
                  P: 038-454-631   F: 038-454-634   C: 66
Vietnam:
NSK VIETNAM CO., LTD.
HEAD OFFICE   Techno Center, Room 204-205, Thang Long Industrial Park, Dong Anh District,
                  Hanoi, Vietnam
                  P: 04-3955-0159   F: 04-3955-0158   C: 84
NSK REPRESENTATIVE OFFICE
HO CHI MINH CITY Suite 307, Metropolitan Building, 235 Dong Khoi Street, District 1,HCMC, Vietnam
                  P: 08-3822-7907   F: 08-3822-7910   C: 84

●Europe

NSK EUROPE LTD. (EUROPEAN HEADQUARTERS)   www.eu.nsk.com
MAIDENHEAD   Belmont Place, Belmont Road, Maidenhead, Berkshire SL6 6TB, U.K.
                  P: 01628-509-800   F: 01628-509-808   C: 44
France:
NSK FRANCE S.A.S.
PARIS   Quartier de l' Europe, 2 Rue Georges Guynemer, 78283 Guyancourt, France
                  P: 01-30-57-39-39   F: 01-30-57-00-01   C: 33
Germany:
NSK DEUTSCHLAND GMBH
HEAD OFFICE   Harkortsrasse 15, D-40880 Ratingen, Germany
                  P: 02102-4810   F: 02102-4812-290   C: 49
STUTTGART   Liebknechtstrasse 33, DE-70565 Stuttgart-Vahingen, Germany
                  P: 0711-79082-0   F: 0711-79082-289   C: 49
WOLFSBURG   Heinrich-Nordhoff-Strasse 101, D-38440 Wolfsburg, Germany
                  P: 05361-27647-10   F: 05361-27647-70   C: 49
INGOLDSTADT   Ingoldstadt, D-85055 Ingoldstadt, Germany
                  P: 0841-901-4640   F: 0841-901-4642   C: 49
NSK PRECISION EUROPE GMBH
DÜSSELDORF   Harkortsrasse 15, D-40880 Ratingen, Germany
                  P: 02102-4810   F: 02102-4812-290   C: 49
NEUWEG FERTIGUNG GMBH
OFFICE/PLANT   Ehinger Strasse 5, D-89597 Munderkingen, Germany
                  P: 07393-540   F: 07393-5414   C: 49
Italy:
NSK ITALIA S.P.A.
MILANO   Via Garibaldi 215, Garbagnate Milanese (Milano) 20024, Italy
                  P: 0299-5191   F: 0299-028373   C: 39
INDUSTRIA CUSCINETTI S.P.A.
TORINO PLANT   Via Giotto 4, I-10080, S. Benigno C. se (Torino), Italy
                  P: 011-982-4811   F: 011-988-0284   C: 39
Netherlands:
NSK EUROPEAN DISTRIBUTION CENTRE B.V.
                  De Kroonstraat 38, 5048 AP Tilburg, Netherlands
                  P: 013-4647647   F: 013-4647648   C: 31
Poland:
NSK EUROPE LTD. REPRESENTATIVE OFFICE
WARSAW   Ul. Migdalowa 4/73, 02-796, Warsaw, Poland
                  P: 022-645-1525   F: 022-645-1529   C: 48
NSK BEARINGS POLSKA S.A.
OFFICE/PLANT   Ul. Jagiellonska 109, 25-734 Kielce, Poland
                  P: 041-366-5001   F: 041-367-0500   C: 48
NSK EUROPEAN TECHNOLOGY CENTER, POLAND OFFICE
                  Ul. Jagiellonska 109, 25-734 Kielce, Poland
                  P: 041-366-5812   F: 041-366-5206   C: 48
NSK STEERING SYSTEMS EUROPE (POLSKA) SP. ZO.O.
CORPORATE   Ul. Mariana Jachimowicza 17, 58-306 Walbrzych, Poland
OFFICE/PLANT   P: 074-664-4101   F: 074-664-4104   C: 48
NSK NEEDLE BEARING POLAND SP.ZO.O.
OFFICE/PLANT   UL. Jagiellonska 109, 25-734 Kielce, Poland
                  P: 041-345-2469   F: 041-345-0361   C: 48
NSK POLSKA SP.ZO.O.
KIELCE   Ul. Karczowkowska 41, 25-711 Kielce, Poland
                  P: 041-347-5110   F: 041-347-5101   C: 48
Spain:
NSK SPAIN S.A.
BARCELONA   C/Tarragona 161, 2a Planta, 08014, Barcelona, Spain
                  P: 093-433-5775   F: 093-433-5776   C: 34
Turkey:
NSK RULMANLARI ORTA DOGU TIC. LTD. STI.
ISTANBUL   19 Mayis Mah. Ataturk Cad. Ulya Engin Is Merkezi No. 68 Kat. 6, Kozyatagi
                  34734, Istanbul, Turkey
                  P: 0216-355-0398   F: 0216-355-0399   C: 90

United Kingdom:
NSK BEARINGS EUROPE LTD.
PETERLEE   3 Brindley Road, South West Industrial Estate, Peterlee, Co. Durham SR8 2JD, U.K.
PLANT   P: 0191-586-6111   F: 0191-586-3482   C: 44
NEWARK   Northern Road, Newark, Nottinghamshire NG24 2JF, U.K.
PLANT   P: 01636-605-123   F: 01636-605-000   C: 44
NSK EUROPEAN TECHNOLOGY CENTRE
NEWARK   Northern Road, Newark, Nottinghamshire NG24 2JF, U.K.
                  P: 01636-605-123   F: 01636-643-241   C: 44
NSK UK LTD.
NEWARK   Northern Road, Newark, Nottinghamshire NG24 2JF, U.K.
                  P: 01636-605-123   F: 01636-605-000   C: 44
NSK PRECISION UK LTD.
PLANT   Northern Road, Newark, Nottinghamshire NG24 2JF, U.K.
                  P: 01636-605-123   F: 01636-605-000   C: 44
NSK STEERING SYSTEMS EUROPE LTD.
HEAD OFFICE   Belmont Place, Belmont Road, Maidenhead, Berkshire SL6 6TB, U.K.
                  P: 01628-509-800   F: 01628-509-808   C: 44
PETERLEE   6/7 Doxford Drive, South West Industrial Estate, Peterlee, Co. Durham SR8 2PP, U.K.
PLANT   P: 0191-518-6400   F: 0191-518-6421   C: 44

●North and South America

NSK AMERICAS, INC. (AMERICAN HEADQUARTERS)
ANN ARBOR   4200 Goss Road, Ann Arbor, Michigan 48105, U.S.A.
                  P: 734-913-7500   F: 734-913-7511   C: 1
Argentina:
NSK ARGENTINA SRL
BUENOS AIRES   Garcia del Rio 2477 Piso 7 Oficina "A" (1429) Buenos Aires-Argentina
                  P: 11-4704-5100   F: 11-4704-0033   C: 54
Brazil:
NSK BRASIL LTDA.   www.br.nsk.com
HEAD OFFICE   Rua 13 de Maio, 1633-14th Andar-Bela Vista-CEP 01327-905 São Paulo, SP, Brazil
                  P: 011-3269-4786   F: 011-3269-4720   C: 55
SUZANO PLANT   Av. Vereador Joao Batista Fitipaldi, 66, CEP 08685-000, Vila Maluf, Suzano, SP, Brazil
                  P: 011-4744-2527   F: 011-4744-2529   C: 55
BELO HORIZONTE   Rua Ceara 1431-4th andar-sala 405-Funcionarios Belo Horizonte-MG, Brazil
                  30150-311
                  P: 031-3274-2591   F: 031-3273-4408   C: 55
JOINVILLE   Rua Blumenau, 178-sala 910-Centro Joinville-SC, Brazil 89204-250
                  P: 047-3422-5445   F: 047-3422-2817   C: 55
PORTO ALEGRE   Av. Cristovão Colombo, 1694-sala 202-Floresta Porto Alegre-RS, Brazil 90560 001
                  P: 051-3222-1324   F: 051-3222-2599   C: 55
RECIFE   Av. Conselheiro Aguiar, 2738-6th andar-conj. 604-Boa Viagem Recife-PE, Brazil 51020-020
                  P: 081-3326-3781   F: 081-3326-5047   C: 55
Canada:
NSK CANADA INC.   www.ca.nsk.com
HEAD OFFICE   5585 McAdam Road, Mississauga, Ontario, Canada L4Z 1N4
                  P: 905-890-0740   F: 800-800-2788   C: 1
TORONTO   5585 McAdam Road, Mississauga, Ontario, Canada L4Z 1N4
                  P: 877-994-6675   F: 800-800-2788   C: 1
MONTREAL   2150-32E Avenue, Lachine, Quebec, Canada H8T 3H7
                  P: 514-633-1220   F: 800-800-2788   C: 1
VANCOUVER   3353 Wayburne Drive, Burnaby, British Columbia, Canada V5G 4L4
                  P: 877-994-6675   F: 800-800-2788   C: 1
Mexico:
NSK RODAMIENTOS MEXICANA, S.A. DE C.V.   www.mx.nsk.com
MEXICO CITY   Av. Presidente Juarez No.2007 Lote 5, Col. San Jeronimo Tepetlacalco,
                  Tlalnepantla, Estado de Mexico, Mexico, C.P.54090
                  P: 55-3682-2900   F: 55-3682-2937   C: 52
United States of America:
NSK CORPORATION   www.us.nsk.com
HEAD OFFICE   4200 Goss Road, Ann Arbor, Michigan 48105, U.S.A.
                  P: 734-913-7500   F: 734-913-7511   C: 1
NSK AMERICAN   4200 Goss Road, Ann Arbor, Michigan 48105, U.S.A.
TECHNOLOGY CENTER P: 734-913-7500   F: 734-913-7511   C: 1
CLARINDA PLANT   1100 N. First Street, Clarinda, Iowa 51632, U.S.A.
                  P: 712-542-5000   F: 712-542-4905   C: 1
FRANKLIN PLANT   3400 Bearing Drive, Franklin, Indiana 46131, U.S.A.
                  P: 317-738-5000   F: 317-738-5050   C: 1
LIBERTY PLANT   1112 East Kitchel Road, Liberty, Indiana 47353, U.S.A.
                  P: 765-458-5000   F: 765-458-7832   C: 1
NSK PRECISION AMERICA, INC.   www.npa.nsk.com
OFFICE/PLANT   3450 Bearing Drive, Franklin, Indiana 46131, U.S.A.
                  P: 317-738-5000   F: 317-738-5050   C: 1
SAN JOSE   780 Montague Expressway, Suite 508, San Jose, California 95131, U.S.A.
                  P: 408-944-9400   F: 408-944-9405   C: 1
NSK STEERING SYSTEMS AMERICA, INC.   www.nssa.nsk.com
OFFICE/PLANT   110 Shields Drive, Bennington, Vermont 05201, U.S.A.
                  P: 802-442-5448   F: 802-442-2253   C: 1
ANN ARBOR   4200 Goss Road, Ann Arbor, Michigan 48105, U.S.A.
                  P: 734-913-7500   F: 734-913-7102   C: 1
NSK-WARNER U.S.A., INC.
TROY   3001 West Big Beaver Road, Suite 701, Troy, Michigan 48084, U.S.A.
                  P: 248-822-8888   F: 248-822-1111   C: 1
NSK LATIN AMERICA, INC.   www.la.nsk.com
MIAMI   2500 NW 107th Avenue, Suite 300, Miami, Florida 33172, U.S.A.
                  P: 305-477-0605   F: 305-477-0377   C: 1

<As of July 2009>

For the latest information, please refer to the NSK website.

Motion & Control

No. 21 December 2009

Published by NSK Ltd.